Theoretical Analyses and Experimental Validation of Dynamic Responses of Fine-Wire Sensors to Fluctuating Velocity and Temperature of Fluid Flows

by

Soe Minn Khine

Doctoral Dissertation

Submitted to
Nagoya Institute of Technology
in partial fulfillment of
the requirements for the degree of
Doctor of Engineering

January 2014

Abstract

Fine-wire sensors have been widely used in thermo-fluid measurement and enable us to measure fluid temperatures and flow velocities of various flow fields. Although the most remarkable feature of the fine-wire sensor techniques is to be easy to use and available at low cost, we can also achieve high-precision measurement provided that we fully understand their static and dynamic response characteristics to use them appropriately.

The purpose of the present study is to analyze theoretically the static and dynamic response characteristics of the fine-wire sensors and to verify experimentally the effectiveness of the theoretical results in order to improve the accuracy and reliability of thermofluid measurement by the fine-wire sensors. In addition, based on the essential knowledge and technical experiences obtained so far, we have succeeded in developing a novel miniature flow-direction sensor which is applicable to outdoor measurement of complex flow fields and verified its potential for micrometeorological measurement.

The present thesis mainly consists of the following three sections: Chapter 2 deals with adaptive response compensation techniques of the constant-current hot-wire anemometer (CCA) and experimental evaluation of their effectiveness; Chapter 3 shows theoretical analysis of heat-conduction error which can be a major source of error in fine-wire temperature measurement and experimental verification of its reliability; Chapter 4 presents a prototype compact sensor for measuring flow velocity and direction of complex flow fields and demonstrates its usefulness in the application to micrometeorological investigation.

The abstracts of the Chapters 2, 3 and 4 are as follows:

Chapter 2: An adaptive response compensation technique has been proposed to compensate for the response lag of the constant-current hot-wire anemometer (CCA) by taking advantage of digital signal processing technology. First, we have developed a simple response compensation scheme based on a precise theoretical expression for the frequency response of the CCA (Kaifuku *et al.* 2010, 2011), and verified its effectiveness experimentally for hot-wires of 5 μm, 10 μm and 20 μm in diameter. Then, another novel technique based on a two-sensor probe technique—originally developed for the response compensation of fine-wire thermocouples (Tagawa and Ohta 1997; Tagawa *et al.* 1998)—has been proposed for estimating thermal time-constants of hot-wires to realize the *in-situ* response compensation of the CCA. To demonstrate the usefulness of the CCA, we have applied the response compensation schemes to multipoint velocity measurement of a turbulent wake flow formed behind a circular cylinder by using a CCA probe consisting of 16 hot-wires, which were driven simultaneously by a very simple constant-current circuit.

Chapter 3: In temperature measurement of non-isothermal fluid flows by a contact-type temperature sensor, heat conduction along the sensor body can cause significant measurement error which is called “heat-conduction error.” The conventional formula for estimating the heat-conduction error was derived under the condition that the fluid temperature to be measured is uniform. Thus, if we apply the conventional formula to a thermal field with temperature gradient, the heat-conduction error will be underestimated. In the present study, we have newly introduced a universal physical model of a temperature-measurement system to estimate accurately the heat-conduction error even if a temperature gradient exists in non-isothermal fluid flows. Accordingly, we have been able to successfully derive a widely-applicable estimation and/or evaluation formula of the heat-conduction error. Then, we have verified experimentally the effectiveness of the proposed formula using the two non-isothermal fields—a wake flow formed behind a heated cylinder and a candle flame—whose fluid-dynamical characteristics should be quite different. As a result, it is confirmed that the proposed formula can represent accurately the experimental behaviors of the heat-conduction error which cannot be explained appropriately by the existing formula. In addition, we have analyzed theoretically the effects of the heat-conduction error on the fluctuating temperature measurement of a non-isothermal unsteady fluid flow to derive the frequency response of the temperature sensor to be used. The analysis result shows that the heat-conduction error in temperature-fluctuation measurement appears only in a low-frequency range. Therefore, if the power-spectrum distribution of temperature fluctuations to be measured is sufficiently away from the low-frequency range, the heat-conduction error has virtually no effect on the temperature-fluctuation measurements even by the temperature sensor accompanying the heat-conduction error in the mean-temperature measurements.

Chapter 4: An effort has been made for measuring flow velocity and direction simultaneously using a coordinated velocity and temperature sensor for outdoor measurement. A heated fine-wire driven at constant-current (CC) mode was used so as to function not only as a velocity sensor but also as a heat source for twelve fine-wire thermocouples equiangularly surrounding the heated wire. An array of these twelve K-type thermocouples can work as a flow direction sensor by detecting heat convection from the upstream heat source generated by the heated fine-wire. The performance of the coordinated velocity and temperature sensor thus developed was tested in outdoor measurement of complex flow fields, and its effectiveness in the application to micrometeorological investigation has been verified.

Acknowledgments

I would never have been possible my dissertation without the support of many people and organizations. I would have to be thankful to those people and organizations in my life.

First and foremost, I would like to express my special gratitude and thanks to Japanese Government (Monbukagakusho: Ministry of Education, Culture, Sports, Science and Technology) for financial supporting my study life throughout Doctor of Engineering Course at Nagoya Institute of Technology and to our Ministry of Industry, The Republic of the Union of Myanmar for the permission to learn the advanced technologies in Japan.

I would like to acknowledge with deep thanks to Dissertation Examining Committee: Professor M. Tagawa, Professor Y. Ishino and Professor M. Furutani for warmly discussions and for carefully reviewing manuscript.

I would like to show my greatest appreciation to my supervisor, Professor M. Tagawa, for his tremendous support and help. Without his encouragement and guidance this dissertation would not have materialized. And also, I would never forget for feeding delicious Japanese and Korean foods while we were going to International and National Conferences.

Furthermore, I would also like to express my deeply grateful to Dr. T. Houra for his numerous stimulating discussions, help with experimental setup and general advice.

I was overcome by his kindly assistances all types of technical and C programming problems at all times.

Besides, I am very thankful to Dr. H. Hattori for his kindly advice and help especially for his warmly notice to summit technical papers in time when we were having dinner in Incheon, Republic of Korea.

I am particularly grateful for the assistance and advice given by Dr. K. Kaifuku for the digital signal processing to carry out the adaptive response compensation of the Constant-Current Hot-wire Anemometer.

My thanks and appreciations also go to Y. Okamoto, undergraduate student in the Department of Mechanical Engineering, Nagoya Institute of Technology who helped me calculation of the wind direction and for doing the outdoor measurements.

I would like to extend my sincerely thanks to all of our Heat Transfer Laboratory members for their kind co-operation and willingness help throughout my studies.

In addition, my special thanks are extended to International Affairs Office of Nagoya Institute of Technology for their warmly welcome and kindly help on international students including me.

Finally, I would like to express my love and gratitude to my beloved families for their understanding, manual support and encouragement through the duration of my studies. I wish also thank to my wife who always encourages me when I face to many difficulties of my theoretical or experimental works and warmly supports me while we are staying in Nagoya.

Contents

Abstract **i**

Acknowledgments **v**

Contents **vii**

List of Figures **xiii**

List of Tables **xxi**

Nomenclature **xxiii**

1 Introduction **1**

1.1 Research Background 1

1.1.1 Constant-current technique in hot-wire anemometers 2

1.1.2 Heat-conduction error of temperature sensors 6

1.1.3 Simultaneous measurement of flow-velocity and flow-direction . 9

1.2 Compensation for response delay of thermofluid measurement system . 11

1.3 Outline of Thesis: A brief overview 13

2 An adaptive response compensation technique for the constant-current hot-wire anemometer 17

2.1 Time constant of hot-wire for CCA mode 18

2.2 Response compensation techniques for the CCA 21

2.2.1 Response compensation based on precise frequency response function 21

2.2.2 Response compensation of CCA by two-sensor technique 24

2.3 Experimental apparatus and measurement system 28

2.3.1 Single-sensor and two-sensor probes 28

2.3.2 Experimental apparatus and measurement system 29

2.4 Results and discussion 30

2.4.1 Theoretical response compensation for single-sensor measurement 30

2.4.2 Adaptive response compensation by the two-sensor technique . . 32

2.5 Application of response compensation technique to multi-sensor measurement 33

2.5.1 Multi-sensor probe 33

2.5.2 Multipoint measurement 34

3 Heat-conduction error of temperature sensors in a fluid flow with nonuniform and unsteady temperature distribution 45

3.1 Theoretical analysis of heat-conduction error of temperature sensor . . 45
  3.1.1 Physical model of temperature sensor 45
  3.1.2 Theoretical analysis model for heat-conduction error in temperature measurement of fluid flows without temperature gradient . 49
  3.1.3 Present theoretical model for heat-conduction error in temperature measurement of fluid flows with temperature gradient . . . 51
  3.1.4 Comparison of estimated heat-conduction error between the existing and proposed formulas 54
3.2 Experimental apparatus and methods 57
  3.2.1 Validation experiment using a wake flow formed behind a heated cylinder 57
  3.2.2 Verification experiment by candle flame 60
3.3 Results and discussion 63
  3.3.1 Measurement of temperature distributions 63
  3.3.2 Experimental evaluation of heat-conduction error and comparison with theoretical estimation 66
3.4 Heat-conduction error in temperature-fluctuation measurement 69
  3.4.1 Physical model for theoretical analysis and frequency response of a temperature sensor with heat-conduction error 69
  3.4.2 Influences of heat-conduction error on temperature-fluctuation measurement 74

4 A coordinated velocity and temperature sensor for flow-direction and flow-velocity measurement 81

4.1 Frequency response of flow-direction and flow-velocity sensor 82

4.2 Sensor arrangement and experimental setup 85

4.2.1 Sensor arrangement 85

4.2.2 Experimental setup 87

4.3 Results and discussion 88

4.3.1 Indoor flow-direction measurement 88

4.3.2 Outdoor flow-direction and flow-velocity measurement 90

5 Conclusions 109

A Theoretically-derived frequency response function of the CCA 113

A.1 Theoretical solution of frequency response of CCA 113

A.2 Frequency response of CCA 118

B Additional information on present theoretical model for heat-conduction error and derivation of frequency response function of temperature sensor with heat-conduction error 121

B.1 Additional information on present theoretical model for heat-conduction error 121

B.2 Derivation of frequency response function of temperature sensor with heat-conduction error 123

Bibliography **127**

List of Figures

1.1 Comparison of the response between CTA and CCA. 3

2.1 Geometrical features of hot-wire probe. 18

2.2 Frequency response of CCA obtained from Eq. (2.8) as a function of length-to-diameter ratio (tungsten wires 5 μm, 10 μm and 20 μm in diameter). 23

2.3 Schematic diagrams of constant-current circuits for driving three different tungsten hot-wires 5, 10 and 20 μm in diameter: (a) driving circuit for 5 and 10 μm wires. Resistance values R_{w} of 5 μm wire (length: 1.5 mm) and 10 μm one (length: 2 mm) are 5.5 $\sim$ 6.5 Ω and 2 $\sim$ 3 Ω, respectively, at room temperature. Driving currents for 5 μm and 10 μm wires were 40 mA and 100 mA, respectively; (b) driving circuit for 20 μm wire. The resistance value R_{w} of 20 μm wire (length: 4 mm) is 1 $\sim$ 2 Ω at room temperature. The driving current was 260 mA. 37

2.4 Experimental apparatus and details of hot-wire probes (single-sensor and two-sensor probes). The 10 μm and 20 μm hot-wire sensors shown in the two-sensor probe can be used for the single-sensor probe. For the two-sensor probe, we employed two combinations: Probe 1 is the combination of 5 μm and 10μm hot-wires; Probe 2 (circled) is that of 10 μm and 20μm ones. (All dimensions in millimeters.) 38

2.5 Comparison of rms velocity profile between single-wire CCA measurements by 5 μm, 10 μm and 20 μm hot-wires and reference measurement by CTA. 39

2.6 Power spectra of velocity fluctuations measured using three single-sensor probes driven by CCA and that by CTA at $y = 16$ mm where the turbulent intensities take their maxima. 39

2.7 Rms velocities obtained by two-sensor technique using R_{max} method (Probe 2). 40

2.8 Comparison of power spectrum distribution using two-sensor technique using R_{max} method (Probe 2). 40

2.9 Instantaneous signal traces of velocity fluctuations: (a) CTA measurement by single-sensor probe; (b) CCA measurements by two-sensor probe. The CTA and CCA outputs were measured independently (they are not simultaneous measurements). 41

2.10 Multi-sensor probe consisting of sixteen 5 μm hot-wires driven at CCA mode: (a) Side view; (b) Front view. 42

2.11 Mean velocity profiles of single-sensor measurement by CTA and multipoint measurement by CCA. Cylinder is positioned at $y = 0$ mm. . . . 43

2.12 Comparison of rms velocity distributions of single-sensor measurement by CTA and multipoint measurement by CCA. 43

2.13 Instantaneous signal traces of multipoint measurement: (a) Uncompensated (raw) outputs; (b) Compensated results by theoretical response compensation scheme using Eq. (2.8). 44

3.1 Configuration of a cylindrical temperature sensor. 47

3.2 Conventional analytical model of heat-conduction error in measurement of uniform fluid temperature.(Sparrow 1976) 48

3.3 Proposed analytical model of heat-conduction error in measurement of non-uniform fluid temperature. 52

3.4 Comparison of heat-conduction error estimated between the conventional formula [Eq. (3.7)] and the proposed one [Eq. (3.12)]. 56

3.5 Experimental apparatus and arrangement of reference and test probes for temperature measurement. 59

3.6 Characteristics of the test field for heat-conduction error. (Mean velocity and temperature distributions were measured by hot-wire anemometer and fine-wire thermocouple. Flow velocity was set to 4 m/s at a wind-tunnel exit.) 61

3.7 Experimental configuration for evaluating heat-conduction error in temperature measurement of candle flame. 62

3.8 Temperature distributions obtained using the reference and test probes designed for wake flow formed behind a cylindrical heater. 64

3.9 Temperature distributions obtained using the reference and test probes designed for candle-flame temperature. 65

3.10 Experimental validation of the proposed theoretical formula [Eq. (3.12)] for estimating heat-conduction error based on the present experimental results. 67

3.11 Theoretical model for analyzing the dynamic response of temperature sensor with heat-conduction error. 71

3.12 Frequency response of temperature sensor with heat-conduction error. (a) gain (b) phase 73

3.13 Mean temperature distribution of a wake flow formed behind a heated cylinder. 75

3.14 Response compensation of temperature fluctuations measured by the reference and test probes. 76

3.15 Frequency responses of the reference and test probes, and power spectra of raw and compensated data measured by the reference cold-wire probe (Tagawa et al. 2005). 77

4.1 Frequency response of temperature sensors as a function of flow velocity: (a) Standard fine-wire thermocouple probe 51 μm in diameter with the prong span of $\ell = 16$ mm [Eq. (3.21)]; (b) V-shaped thermocouple probe 51 μm in diameter with the sensing length of $L = 8$ mm [Eq. (3.19)]. . 83

4.2 Frequency response of CCA reference sensor and test sensor as a function of flow velocity using Eq. (2.8): (a) Reference sensor (tungsten wire 10 μm in diameter); (b) Test sensor (nichrome coil 20 μm in diameter). . . 84

4.3 Flow direction sensor combined with the CCA and twelve K-type thermocouples: (a) Photograph of the sensor from the front view; (b) Plan view of the fabricated sensor. (All dimensions in millimeters.) 95

4.4 Campus map Nagoya Institute of Technology (NIT) to show the location of outdoor measurement. 96

4.5 Outdoor measurement using flow-direction sensor near the Building No. 12 in the campus of NIT. 97

4.6 Schematic diagram for finding a true peak using Gaussian fitting. . . . 97

4.7 Test of the flow-direction sensor by indoor calibration experiment. . . . 98

4.8 Fluctuation intensities (r.m.s. values) of flow-direction angle obtained in indoor measurement. 98

4.9 Schematic diagrams for showing the principle operation of flow-direction and flow-velocity measurement: (a) Arrangement of twelve thermocouples for detecting flow-direction; (b) Decomposition of flow-direction measurement into two velocity components in the Cartesian coordinates. 99

4.10 Sample instantaneous signal traces of flow velocities measured by the CCA reference (tungsten wire 10 μm in diameter) and test (nichrome coil) sensors.The upper figure shows the raw (uncompensated) data and the lower one the results obtained by the response compensation for the CCA sensors. 100

4.11 Sample flow-direction measurement in steady wind conditions: The instantaneous signal traces of the twelve type-K thermocouples in outdoor measurement conducted near Building No.12. 101

4.12 Sample flow-direction measurement in outdoor measurement conducted near Building No. 12 under steady wind conditions: The detected flow-direction is represented by the channel numbers of the twelve thermocouples. 102

4.13 Flow-direction measurement in outdoor measurement conducted near Building No. 12 under steady wind conditions. The wind direction is represented by the angle to the north direction (0 or 360 degree). . . . 102

4.14 Flow-velocity measurement by the CCA sensor (nichrome coil) conducted near Building No. 12 under steady wind conditions: The results are shown in the two velocity components decomposed using both flow-velocity and flow-direction measurements. 103

4.15 Sample flow-velocity measurements by the CCA sensor (nichrome coil whose diameter is 20 μm) and the reference one (tungsten wire 10 μm in diameter) under complex wind conditions. 104

4.16 Comparison of instantaneous signal traces measured under complex wind conditions between the uncompensated (raw) thermocouple outputs and compensated ones. 105

4.17 Sample flow-direction measurement in outdoor measurement conducted near Building No. 12 under unsteady wind conditions: The detected flow-direction is represented by the channel numbers of the twelve thermocouples. 106

4.18 Flow-direction measurement in outdoor measurement conducted near Building No. 12 under unsteady wind conditions. The wind direction is represented by the angle to the north direction (0 or 360 degree). . . . 106

4.19 Flow-velocity measurement by the CCA sensor (nichrome coil) conducted near Building No. 12 under unsteady wind conditions: The results are shown in the two velocity components decomposed using both the velocity and flow-direction measurements. 107

A1 Frequency response of CCA obtained using Eq. (2.8): (a) Absolute gain; (b) Normalized gain; (c) Phase 120

B1 Comparison of heat-conduction error estimated between the existing equation [Eq. (3.7)] and the proposed ones [Eq. (3.12) and (B2)]. 122

List of Tables

2.1 Detailed features of three different hot-wires used. Definitions of the geometrical parameters d_1, ℓ and L are given in Fig. 2.1. 22

2.2 Time-constant values estimated from e_{min} method, R_{max} method and Collis-Williams law given by Eq. (A13) ($y = 16$ mm) 31

Nomenclature

Roman Symbols

a	Thermal diffusivity [m^2/s]
c	Specific heat [J/(kg·K)]
d	Wire diameter [m]
f	Frequency [Hz]
G	Time derivative of velocity U [$\mathrm{m/s}^2$] [$\equiv \mathrm{d}U/\mathrm{d}\tau$]
H	Frequency response function [K/(m/s)]
h	Heat transfer coefficient [$\mathrm{W}/(\mathrm{m}^2{\cdot}\mathrm{K})$]
I	Electric Current [A]
ℓ	Wire length [m]
L	Distance between prongs or length of temperature sensor [m]
R	Electrical resistance [Ω]
S	Cross-sectional area [m^2]
T, t	Temperature, Temperature fluctuation [K]
U, u	Flow velocity, Velocity fluctuation [m/s]

x, y, z	Spatial coordinates

Greek Symbols

α	Temperature coefficient of fine wire [K^{-1}]
λ	Thermal conductivity [W/(m·K)]
μ	Viscosity [Pa·s]
ν	Kinematic viscosity [m^2/s]
ρ	Density [kg/m^3]
τ	Time or Time constant [s] [$\equiv 1/(2\pi f_\mathrm{c})$, f_c: Cutoff frequency]
χ	Electric resistivity [Ω·m]
Ω	Parameter defined by Eq. (3.20) and Eq. (A8)
ω	Angular frequency [s^{-1}] ($\equiv 2\pi f$)

Subscripts and Superscripts

0	Constant temperature at fixed point or solid wall or position at sensor tip
1	Wire (sensing part) or Hot-wire 1
2	Stub or Hot-wire 2
w	Sensor body temperature
m	Fluid temperature(true value) at sensor tip
a	Ambient temperature
g	Flow velocity to be measured
$\overline{(\ )}$	Time average

$\hat{( )}$	Fourier transform
$( )'$	Fluctuating component

Abbreviation

CTA	constant-temperature hot-wire anemometer
CCA	constant-current hot-wire anemometer

Chapter 1

Introduction

1.1 Research Background

Fine-wire sensors have been widely used in thermo-fluid measurement and enable us to measure fluid temperatures and flow velocities of various flow fields. Although the most remarkable feature of the fine-wire sensor techniques is to be easy to use and available at low cost, we can also achieve high-precision measurement provided that we fully understand their static and dynamic response characteristics to use them appropriately.

The purpose of the present study is to analyze theoretically the static and dynamic response characteristics of the fine-wire sensors and to verify experimentally the effectiveness of the theoretical results in order to improve the accuracy and reliability of thermofluid measurement by the fine-wire sensors. In addition, based on the essential knowledge and technical experiences obtained so far, we have succeeded in developing a novel miniature flow-direction sensor which is applicable to outdoor measurement of complex flow fields and verified its potential for micrometeorological measurement.

1.1.1 Constant-current technique in hot-wire anemometers

In recent years, particle image velocimetry (PIV) has become one of the most popular techniques for measuring velocity fields. The hot-wire anemometry (Hinze 1975; Comte-Bellot 1976; Perry 1982; Bruun 1995; Tropea *et al.* 2007), on the other hand, has long been used mainly for measuring turbulent gaseous flows because of its simple and highly-reliable measurement systems and wide range of applicability. Thus, the hot-wire anemometry is still frequently utilized as a reliable research tool for statistical and frequency analyses of turbulent flows.

The hot-wire anemometry is generally driven at three operation modes, i.e., the constant temperature, constant-current and constant voltage modes. For the application of the hot-wire anemometry, the constant-temperature anemometer (CTA) is commercially available and almost always used as a standard system for driving the hot-wire, while the other two modes are rarely used, primarily due to their response lag during velocity fluctuation measurement. However, the electric circuit of the CTA is not simple, and the measurement system is fairly expensive. On the other hand, the constant-current hot-wire anemometer (CCA) can be set up with a very simple and low-cost electric circuit for heating the hot-wire. Thus, if we improve the response

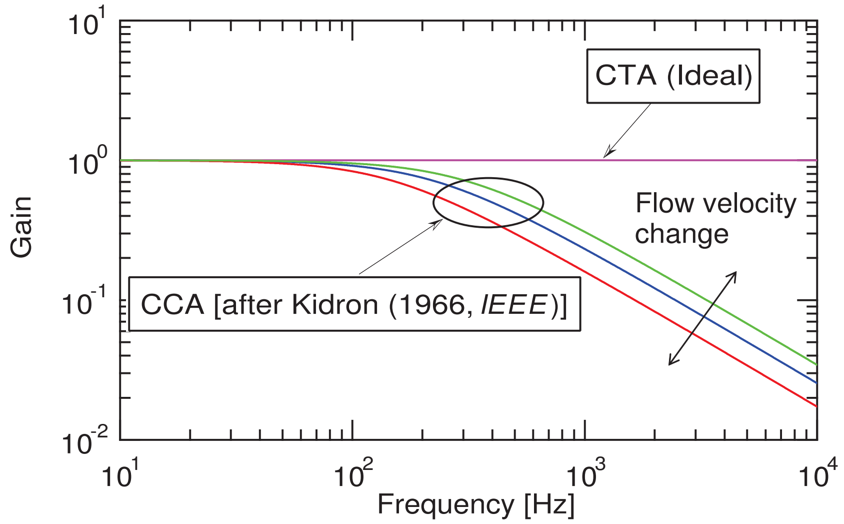

Figure 1.1 Comparison of the response between CTA and CCA.

characteristics of the CCA with the aid of digital signal processing, the CCA will have a great advantage over the CTA and will be a promising tool for multipoint turbulence measurement.

In the previous studies, some comparisons between the representative two hot-wire anemometers—CTA and CCA—were made (Kidron 1967; Chevray and Tu Tu 1972; Hultmark and Smits 2010). Kidron (1967) showed that unequal signal-to-noise ratios of the two anemometers, CTA and CCA, in the same bandwidth caused no significant difference between them. On the other hand, Chevray and Tu Tu (1972) showed that the CCA results can be linearized by using a compensation circuit on the basis of simultaneous measurement of velocity and temperature. The efforts to improve the CTA and CCA techniques are still going on. For example, Hultmark and Smits (2010) has recently proposed a new correction method for changes in the ambient fluid temperature which affects the calibration curves of CTA and CCA. The results showed that the proposed method worked correctly at relatively large changes in the ambient temperature—15°C for CTA and 9°C for CCA.

When a hot-wire is driven at a constant electric current, the wire temperature, which corresponds to the hot-wire output, does not respond correctly to high-frequency velocity fluctuations because of the thermal inertia of the wire (Fig. 1.1). In this figure, the vertical axis indicates the gain of hot-wire output and frequency responses of CTA and CCA are presented by Kaifuku (2010). As seen from the figure, the response of CCA depends largely on the flow velocity and the response speed is also much lower than the CTA. Thus, the CCA output needs to be compensated adequately for the response lag to reproduce high-frequency components of the measurement data. In order to investigate the response characteristics of the hot-wire, Hinze (1975) analyzed the dynamic behavior of the hot-wire with heat loss to the wire supports. As a result, it was shown that the aspect ratio of the hot-wire (the length-to-diameter ratio) is an important parameter characterizing the response of the hot-wire, and that the thermal time constant will decrease with increasing heat loss to the wire support. In our previous studies (Kaifuku *et al.* 2010, 2011), we have successfully derived a precise theoretical solution for the frequency response of an actually-used hot-wire probe which consisted of a fine metal wire, stub parts (copper-plated ends/silver cladding of a Wollaston wire) and prongs (wire supports). As a result, we were able to find the geometrical conditions for the frequency response of the CCA to be approximated by the first-order lag system, which can be characterized by a single system parameter called the thermal time-constant (Bruun 1995).

If the time-constant value is known in advance, we may apply the existing response compensation techniques for the first-order system (Perry 1982; Bruun 1995) to recover the response delay in the CCA measurement. In reality, however, since the time-constant value of the CCA changes largely depending on flow velocity (Kidron 1966) and physical properties of the working fluid, it is very difficult to estimate the time-constant value of the hot-wire accurately. In our previous papers (Kaifuku *et al.* 2010, 2011), we proposed a digital response compensation scheme based on the precise theoretical expression for the frequency response of the CCA. The results showed that the scheme worked successfully, reproducing high-frequency velocity fluctuations of a turbulent flow. However, this compensation scheme needs more information regarding the geometrical parameters of the hot-wire probe, i.e., the diameters and lengths of the wire and stub together with their physical properties.

In the present study, first, we throughly tested the theoretical expression for the frequency response of the CCA by applying it extensively to the digital response compensation of three different hot-wire probes consisting of tungsten wires 5 μm, 10 μm and 20 μm in diameter. Secondly, we have proposed a novel approach to the response compensation of the CCA output that will work without our knowing in advance the geometrical parameters of the hot-wire probe. This approach is based on a two-sensor probe technique for compensating the response delay of fine-wire thermocouples (Tagawa and Ohta 1997; Tagawa *et al.* 1998), and enables *in-situ* estimation of the time-constant values of the hot-wire probe, and will realize adaptive response compensation of the CCA outputs. Specifically, in the two-sensor probe technique, two hot-wires of unequal diameters—having different response speeds—are used simultaneously, and the time-constant values of the two hot-wires can be obtained from the measurement data itself without carrying out any dynamic calibration of the hot-wire probe. Finally, in order to demonstrate the usefulness of the CCA, we have applied the above response compensation schemes to multipoint velocity measurement of turbulent flows (e.g., Blackwelder and Kaplan 1976; Glauser and George 1992; Houra and Nagano 2008). In the present multipoint measurement, we have simultaneously used 16 hot-wires driven by the CCA to measure a turbulent wake flow formed behind a cylinder. In these verification experiments, we have measured turbulence intensities (r.m.s. values), power spectra and instantaneous signal traces of the velocity fluctuations, and have compared them with those obtained by a hot-wire probe driven by a commercially available constant-temperature hot-wire anemometer.

1.1.2 Heat-conduction error of temperature sensors

In temperature measurement of fluid flows, heat conduction along the axis of a temperature sensor often causes large measurement error. For example, if we insert a rod-type temperature sensor into a high-temperature fluid flow, heat transfer will occur from the hot region to the circumference because of the heat conduction through the sensor body and its support. Then, a measured temperature, which corresponds to the temperature at the detecting point (sensing part), can become lower than the fluid temperature to be measured. Consequently, the sensor output will indicate a temperature lower than the actual fluid temperature. Depending on temperature fields to be measured and/or measurement conditions, this phenomenon can lead to a large error in temperature measurement, which is called "heat-conduction error." As an example, in the temperature measurement of a candle flame entailing a high-temperature gas flow confined in a small space, even a relatively fine type-R thermocouple 100 μm in diameter has indicated a temperature 300 degrees lower than the actual fluid temperature because of the heat conduction induced by a large temperature gradient along the thermocouple wire (see Fig. 3.9).

As mentioned above, for accurate measurement of fluid temperature, it is essential to select a temperature sensor appropriately and use it properly so as to minimize the heat-conduction error. The basic principle is to make the sensor body as fine as possible and to arrange it so as to minimize the temperature gradient along the sensor body. However, we are often forced to use a temperature sensor in a way not in line with the basic principles depending on measurement situations and conditions. In such a case, we need to estimate the heat-conduction error quantitatively and correct it accurately.

If we have a simple method for estimating or evaluating the heat-conduction error of a temperature sensor, it must be a useful tool for appropriate selection of temperature sensors and/or reliable correction of temperature measurements. A representative estimation method is the theoretical formula proposed by Sparrow (1976) which has been used extensively. The formula was derived based on fairly limited assumptions that the velocity and temperature profiles of a fluid flow are uniform and the temperature sensor is inserted through a solid wall into the flow, in which the solid wall is kept at a constant temperature different from the fluid one. Recently, an extended physical model (Kobus 2006) has been successfully introduced into the theoretical analysis of the heat-conduction error to provide a wide range of applicability of the formula. In this model, a nonuniform temperature profile along the sensor support is taken into consideration, although the assumption that the velocity and temperature profiles along the sensor body are uniform has been employed. On the other hand, in order to make the analysis more realistic in reference to actual measurement situations, a numerical simulation has been introduced to estimate the heat-conduction error in a flow field with nonuniform velocity and temperature distributions found in the immediate vicinity of a heated wall (Kaiser 2012).

In the present study, we propose a new theoretical approach which is applicable to accurate estimation and reliable evaluation of the heat-conduction error even in the case of nonuniform and/or unsteady temperature fields, and test the effectiveness of the proposed approach experimentally. The newly developed formula for estimating the heat-conduction error provides a useful tool for appropriate selection and proper use of temperature sensors, and enables us to evaluate the reliability of measurements and to correct the measurement error rationally.

1.1.3 Simultaneous measurement of flow-velocity and flow-direction

Air flow measurement for both direction and magnitude has a vital role in a wide variety of research fields such as flow assessment for siting wind turbines, measuring an intake air stream in automobile engines, weather forecasting, investigating urbanization effects (heat-island effect and air pollution), environmental monitoring and so on. Most of those measurement techniques are basically designed as a mechanical system on a relatively large scale so as to be applicable to outdoor measurements. Recently, the flow-direction measurement techniques for precise flow control are making rapid progress by using the micro-electromechanical system (MEMS) technology (Adamec *et al.* 2003; Kim and Kim 2006; Tan *et al.* 2007; Lee *et al.* 2008; Ma *et al.* 2009; Hayashi *et al.* 2009; Kottapalli *et al.* 2011; Dong *et al.* 2012). In recent years, Nguyen (2005) presented a thermal flow sensor, which was constructed as a mechanical system by combining a cylindrical heater with an array of thermocouples. In this paper, three different methods for velocity measurement (the hot-wire method, calorimetric one and a novel average-temperature method) and two algorithms for direction measurement (analytical and Gaussian estimators) were also presented. The validation results confirmed that the calorimetric method was suitable for low Peclet-number cases from 0 to 10, and the Gaussian estimator provided better results with satisfactory accuracy when determining the flow direction. Another approach for the flow-direction measurement was proposed by using solid-state devices (Makinwa *et al.* 2001). This instrument was constructed by merging mechanical and electronic technologies so as not to have any moving parts. The experimental results showed that the accuracy of the sensor worked well in the range of 0.1 to 25 m/s and the measurement errors were less than 0.5 m/s (±3%) for wind velocity and ±3° for wind direction.

In the present study, the flow-direction sensor is basically designed as a mechanical system by utilizing the important knowledge and technical essences accumulated in the preceding studies [Minn Khine *et al.* 2013 (a)(b)(c)]. The constant-current hot-wire anemometer (CCA) is served simultaneously as a heater and a flow-velocity sensor in order to reduce the design complexity of the sensor. This design will enable us to construct a compact flow-direction sensor at low cost. To detect the flow direction, the twelve-thermocouples are used, which were arranged equiangularly at every 30° around the CCA, to sense fully the flow direction of 0° to 360°. Since the positioning of the thermocouples is a dominant factor determining the spatial and temporal resolution of the flow-direction sensor, it is necessary to optimize the distance between the CCA sensor (nichrome coil) and the surrounding thermocouples. As a result, the proposed sensor provides a reliable technique for measuring simultaneously flow-direction and flow-velocity in outdoor measurement.

1.2 Compensation for response delay of thermofluid measurement system

A measurement method for thremofluid systems must be selected so as to meet the requirements for various features in accordance with the intended use. However, sometimes it is necessary to make much account of available technical knowledge and experiences and the safety issues specific to the measurement method to be employed. Thus, various conditions such as an object to be measured, purpose of measurement, measurement accuracy required and expenses for instruments need to be taken into consideration.

Although there must be a number of factors to consider when determining an appropriate method for measuring thermofluid systems, we need to usually place greater emphasis on usability, durability and the cost of the measurement method. However, since a measurement method thus selected has generally insufficient temporal resolution—the dynamic response of the method is slow, it is difficult to measure accurately the fluctuation component of the measurements which contain high-frequency components in the spectrum. Therefore, the problem of the response delay will be inevitable in many different situations of thermofluid measurement. Therefore, in order to evaluate accurately the thermofluid phenomena by using a standard (not specially developed) measurement method, it is often necessary to compensate their response delay appropriately.

To compensate the response delay of the measurement system, we need to identify the response characteristics by calibrating the dynamic characteristics of the measurement system. Since good calibration of the response characteristics is essential to realizing reliable unsteady measurement, various calibration techniques have been proposed for every measurement method. However, there exists considerable difficulties when calibrating the dynamic characteristics of the measurement system, since the calibration is often tedious work and more importantly it is almost impossible to cover all the measurement conditions.

To solve this problem, the rational approach utilizing the digital signal processing techniques has been proposed by Tagawa and Ohta (1997) and Tagawa *et al.* (1998). They have found a novel method for identifying the time constant of the thermocouple—the primary parameter representing the response characteristics of the thermocouple—without any dynamic calibration, and called it the two-thermocouple probe technique. Since this method can provide an essential information on the dynamic characteristics of the thermocouple only using the measurement data itself, it is not necessary to conduct the dynamic calibration experiment in advance. The details of this method and its application to the present study are described in section 2.2.2.

1.3 Outline of Thesis: A brief overview

This dissertation is composed of five chapters. The brief overviews of each chapter are described as follow:

In Chapter 1, the research backgrounds of response compensation of the constant-current hot-wire technique, evaluation of the heat-conduction error of temperature sensors and simultaneous measurement of flow-direction and flow-velocity are presented in this chapter. The main portion of the dissertation is focused on the theoretical analysis of the static and dynamic responses of the thermofluid measurement systems and the compensation techniques for the response delay in the measurement of velocity and temperature fluctuations. A brief overview of each chapter is also included in this chapter.

In Chapter 2, an adaptive response compensation technique for the constant-current hot-wire anemometer (CCA) is proposed. First, the frequency response of three different hot-wire probes (tungsten wires 5 μm, 10 μm and 20 μm in diameter) has been investigated theoretically, and the outputs of the hot-wire probes have been compensated for the response delay of the CCA by using an adaptive response compensation technique. To avoid using the geometrical parameters of the hot-wire probe, a novel approach to the response compensation of the CCA called a two-sensor probe technique has been introduced. Secondly, the effectiveness of the CCA technique has been appraised by applying the above-mentioned response compensation scheme for the CCA to the multi-point velocity measurement of turbulent flows by using a ladder-shaped probe consisting of 16 hot-wires. In the verification experiment of the CCA technique, a wake flow formed behind a cylinder placed just above the exit of an upright wind tunnel. Then, the measurement results—turbulence intensities (r.m.s. values), power spectra and instantaneous signal traces of the velocity fluctuations—were compared with those obtained using a commercially available constant-temperature hot-wire anemometer (CTA).

In Chapter 3, the heat-conduction error of temperature sensors in a fluid flow with nonuniform and unsteady temperature distribution is discussed. The existing theoretical analyses of the heat-conduction error of temperature sensors were constructed based on the assumption that a fluid flow has a uniform temperature field. In the actual situation of fluid temperature measurement, however, it seems to be natural for the temperature fields of fluid flows to be nonuniform and fluctuate as observed in turbulent flows. In addition, fluid temperature measurement is performed not only in pipe/channel flows confined by solid walls but often in unconfined jet/boundary-layer flows. Therefore, in the present study, a new analytical model has been introduced to the estimation of the heat-conduction error in temperature measurement of fluid flows with a temperature gradient. The validity of the proposed formula has been verified experimentally in a very different fluid thermal field, a wake flow formed behind an electric heater and a candle flame. Furthermore, the effect of the heat-conduction error on temperature fluctuation measurements has been successfully analyzed to derive a unique evaluation formula theoretically.

Chapter 4 describes the design and construction of a compact sensor for measuring flow-direction and flow-velocity simultaneously based on a coordinated CCA and thermocouple technique. Based on the knowledge and technical experiences presented in the preceding chapters, a new flow-direction sensor has been successfully realized by combining the CCA technique with the thermocouple one. Then, the flow-direction and flow-velocity sensor developed has been applied to the outdoor measurement to appraise the usefulness and performance and to verify the potential capability for micrometeorological measurement.

Finally, the concluding remarks are given in Chapter 5.

The supplementary investigations and the derivation processes of the equations related to the subjects of Chapters 2 and 3 are given in Appendixes A and B.

Chapter 2

An adaptive response compensation technique for the constant-current hot-wire anemometer

In this chapter, we have carried out the response compensation of the constant-current hot-wire anemometer (CCA) which has a slow response and also the driving circuit is simple and inexpensive. First, we have tested using the adaptive response compensation technique to three types of hot-wires (5 μm, 10 μm and 20 μm in diameters). Then we have tried to propose the two-sensor probe technique of the CCA for estimating time constants without knowing any geometrical features and physical properties of the hot-wire probe used. Finally, we have applied this response compensation scheme to multi-point velocity measurement by using multi-sensor probe. We have compared all the verification results of the CCA with those obtained by a hot-wire (5 μm in diameter) driven by a commercially available CTA.

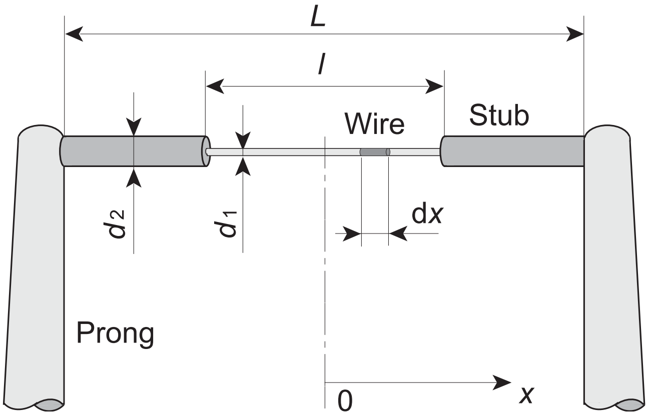

Figure 2.1 Geometrical features of hot-wire probe.

2.1 Time constant of hot-wire for CCA mode

Figure 2.1 shows the geometrical features and coordinate system of the CCA probe used in the theoretical analysis (see Appendix A). As shown in Fig. 2.1, the hot-wire is a fine tungsten wire (sensing part) with copper-plated ends (stubs) which are soldered to the prongs (wire supports). By applying electric current I to the fine-wire element (length: $\mathrm{d}x$, diameter d_1), the generated Joule heat should balance with the sum of the following heat losses: heat convection, heat conduction, heat accumulation and thermal radiation. Since the heated wire is very fine, we can assume that the amount of heat radiation is negligible and the cross-sectional temperature distribution is uniform (Kato *et al.* 2007). Therefore, the energy balance equation for the hot-wire can be written as (in this section, the subscript 1 for wire or 2 for stub is omitted for simplicity):

$$\frac{\partial T}{\partial \tau} = \frac{I^2 R^*}{\rho c S} - \frac{\pi d h}{\rho c S}(T - T_\mathrm{a}) + a\frac{\partial^2 T}{\partial x^2}, \tag{2.1}$$

where τ is time, R^* denotes the wire resistance per unit length and given by $R^* =$

χ/S [χ: electric resistivity, S ($= \pi d^2/4$): cross-sectional area of the wire], and I: electric current, h: heat transfer coefficient, T: wire temperature, T_a: ambient fluid temperature, a ($= \lambda/\rho c$): thermal diffusivity of wire material, λ: thermal conductivity, ρ: density, c: specific heat. In Eq. (2.1), R^* can be expressed as a linear function of the temperature difference between the wire and reference temperatures as:

$$R^* = R^*_\mathrm{a}[1 + \alpha_\mathrm{a}(T - T_\mathrm{a})], \tag{2.2}$$

where R^*_a is electric resistance per unit wire length at the reference temperature and α_a denotes a temperature coefficient of wire material. Then, Eq. (2.1) can be rewritten as:

$$\frac{\partial T}{\partial \tau} = \frac{I^2 R^*_\mathrm{a}}{\rho c S} - \frac{\pi d h - I^2 R^*_\mathrm{a}\alpha_\mathrm{a}}{\rho c S}(T - T_\mathrm{a}) + a\frac{\partial^2 T}{\partial x^2}. \tag{2.3}$$

In hot-wire measurement, the effective cooling rate of the heated wire must principally be a function of flow velocity and can be obtained from the heat transfer coefficient of the fine wire, h, while the heat generation term is a nonlinear function of the electric current I and the wire resistance is determined by wire temperature as shown in Eq. (2.2). To make Eq. (2.3) theoretically treatable, it needs to be linearized by decomposing the relevant physical quantities into a time-averaged component and a fluctuation one as: $T = \overline{T} + t$, $h = \overline{h} + h'$, $I = \overline{I} + i$ (Hinze 1975, Li 2004, Berson *et al.* 2010). Then, we can obtain a governing equation of the constant-current hot-wire anemometer by formulating the energy balance equation with the following procedures: (i) ignore the contribution of the second- and higher-order fluctuation components; (ii) derive a governing equation for the first-order fluctuation components by time-averaging the equation obtained in (i); (iii) introduce a well-accepted correlation of $h = A + BU^n$ to relate the heat transfer coefficient to the flow velocity; and (iv) assume the electric current I to be constant. From the above procedures, the static and dynamic characteristics of the CCA are expressed as:

$$\begin{aligned} 0 &= \frac{\overline{I}^2 R_{\mathrm{a}}^*}{\rho c S} - \frac{1}{\tau_i}(\overline{T} - T_{\mathrm{a}}) + a\frac{\mathrm{d}^2\overline{T}}{\mathrm{d}x^2}, & (2.4)\\ \frac{\partial t}{\partial \tau} &= -\frac{1}{\tau_i}\,t + a\frac{\partial^2 t}{\partial x^2} - \frac{\pi d B n \overline{U}^{n-1}}{\rho c S}(\overline{T} - T_{\mathrm{a}})\,u, & (2.5) \end{aligned}$$

where τ_i is the thermal time-constant ($i = 1$ or 2), and is primarily related to the time-averaged heat transfer coefficient around the fine wire $\overline{h}$ and electric current $\overline{I}$ as follows:

$$\tau_i = \frac{\rho c S}{\pi d \overline{h} - \overline{I}^2 R_{\mathrm{a}}^* \alpha_{\mathrm{a}}}. \tag{2.6}$$

In Eq. (2.6), the heat transfer coefficient $\overline{h}$ can be expressed as a function of flow velocity $\overline{U}$ and is written as:

$$\overline{h} = A + B\overline{U}^n \tag{2.7}$$

where the constants A, B and n can be obtained from the Collis-Williams correlation equation [Collis and Williams 1959; see Eq. (A13)]. As seen from Eq. (2.6), the time constant τ_i should be a complex function of flow velocity $\overline{U}$, driving current $\overline{I}$, wire diameter d, etc. Thus, in general, we need to either obtain the time-constant value experimentally or estimate it empirically.

2.2 Response compensation techniques for the CCA

2.2.1 Response compensation based on precise frequency response function

The frequency response of the hot-wire driven by the CCA, $H_1(\omega)$, has been derived theoretically by the authors (Kaifuku *et al.* 2010, 2011), and is expressed by the following equation (see Appendix A):

$$\begin{aligned} H_1(\omega) \;&= -\frac{Z_{1,\mathrm{m}}\tau_1}{1+j\omega\tau_1} + \left[\frac{Z_{2,\mathrm{m}}\tau_2}{1+j\omega\tau_2} + \left(\frac{Z_{1,\mathrm{m}}\tau_1}{1+j\omega\tau_1} - \frac{Z_{2,\mathrm{m}}\tau_2}{1+j\omega\tau_2}\right)\cosh\left(\frac{\Omega_2(L-\ell)}{2}\right)\right] \\ &\times \left\{\frac{\Omega_1\ell}{2}\left[\coth\left(\frac{\Omega_1\ell}{2}\right)\cosh\left(\frac{\Omega_2(L-\ell)}{2}\right) + \frac{\Omega_1}{\Omega_2}\frac{d_1^2\lambda_1}{d_2^2\lambda_2}\sinh\left(\frac{\Omega_2(L-\ell)}{2}\right)\right]\right\}^{-1}. \end{aligned} \tag{2.8}$$

To estimate theoretically the frequency response of hot-wires, we have applied Eq. (2.8) to the three different tungsten hot-wires (5 μm, 10 μm and 20 μm in diameter) with copper-plated ends (stubs). The geometrical parameters of the hot-wires are given in Table 2.1, in which ℓ/d_1 and L denote the aspect ratio of the fine-wire and the distance between the prongs, respectively. All the hot wires have copper-plated ends 35 μm in diameter and are supported by the prongs (see Fig. 2.1). In the present analysis, electric currents for the hot-wires driven at the CCA mode were set respectively at 40 mA, 100 mA and 260 mA for the 5 μm, 10 μm and 20 μm hot-wires, so as to provide adequate sensitivity to flow velocity. The airflow velocity and fluid temperature were 7 m/s and 20°C, respectively. Figure 2.2 shows the Bode diagram (gain) calculated from Eq. (2.8). As shown in Fig. 2.2, the frequency response of the hot-wire driven

Table 2.1 Detailed features of three different hot-wires used. Definitions of the geometrical parameters d_1, ℓ and L are given in Fig. 2.1.

Material	d_1 [μm]	ℓ [mm]	L [mm]	ℓ/d_1 [-]
Tungsten	5	1.5	5	300
ditto	10	2.0	6	200
ditto	20	4.0	7	200

at the CCA mode can be naturally improved by decreasing the wire diameter. In the present calculation conditions, the 5 μm tungsten wire responded adequately to velocity fluctuations up to about 100 Hz without response compensation, while the response speed of the 20 μm wire decreased by an order of magnitude compared with the 5 μm one.

The length-to-diameter ratio (aspect ratio) of the tungsten wires shown in Fig. 2.2 ranges from 200 to 300. In this regard, Hinze (1975) showed that, for platinum-iridium wires, the aspect ratio should be greater than 200, and be still higher for tungsten wires to make the wire resistance (temperature) almost uniform along the central 60 percent of its length. In such a case, as seen from Fig. 2.2, the frequency response of the hot-wire driven by the CCA can be approximated by the first-order lag system, whose response can be expressed as a function of only the time constant. If the aspect ratio becomes smaller than about 200, the cooling effects of the wire supports such

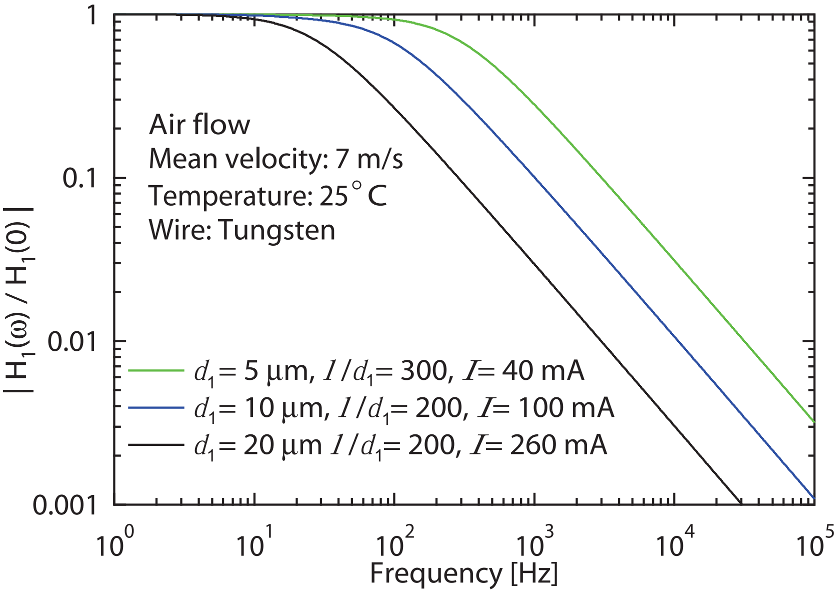

Figure 2.2 Frequency response of CCA obtained from Eq. (2.8) as a function of length-to-diameter ratio (tungsten wires 5 μm, 10 μm and 20 μm in diameter).

as the stub and prong will emerge, and can deteriorate the frequency response of the hot-wire. As a result, the Bode diagram for shorter wires behaves in a more complex manner (see Fig. A1 in Appendix A).

The digital signal processing of the response compensation based on a known frequency-response function was described in detail in a previous paper (Tagawa et al. 1998). The procedure is applicable to the hot-wire measurement and can be summarized as follows: First, the hot-wire output (time-series data) is transformed into frequency-domain components using the fast Fourier transform (FFT). Next, each frequency component is multiplied by $1/H_1(\omega)$—the reciprocal of Eq. (2.8)—to compensate for the output in the frequency domain. Finally, the inverse FFT is applied to the frequency-domain components thus calculated to obtain the compensated time-series data of the hot-wire output.

2.2.2 Response compensation of CCA by two-sensor technique

To use the above response compensation scheme based on Eq. (2.8), we need to know the geometrical parameters of the hot-wire probe. On the other hand, if the frequency response of the hot-wire can be represented by the first-order lag system, we can apply the two-sensor technique, which does not need the geometrical parameters of the probe (Tagawa and Ohta 1997; Tagawa *et al.* 1998), to the response compensation of the CCA. In the present study, we used two methods called $e_{\min}$ and $R_{\max}$. Their methods are given below.

$e_{\min}$ method

The first-order lag systems of the two hot-wires driven by the CCA can be expressed as follows:

$$\left.\begin{aligned} U_{\mathrm{g}1} &= U_1 + \tau_1 \frac{\mathrm{d}U_1}{\mathrm{d}\tau}, \\ U_{\mathrm{g}2} &= U_2 + \tau_2 \frac{\mathrm{d}U_2}{\mathrm{d}\tau}, \end{aligned}\right\} \tag{2.9}$$

where U and U_{g} denote respectively raw output of the CCA (uncompensated velocity) and fluid velocity around the hot-wire, and τ and τ_i are the time and time-constant defined by Eq. (2.6), respectively. The subscripts $i = 1$ and 2 denote two unequal hot-wires different in diameter. Ideally, the fluid velocities surrounding the two hot-wires,

$U_{\mathrm{g}1}$ and $U_{\mathrm{g}2}$, must be expressed as $U_{\mathrm{g}1} = U_{\mathrm{g}2}$ ($= U_{\mathrm{g}}$). In reality, however, the finite spatial resolution between the two hot-wires and the instrumentation noise may change the relation between $U_{\mathrm{g}1}$ and $U_{\mathrm{g}2}$ as $U_{\mathrm{g}1} \simeq U_{\mathrm{g}2}$. Thus, the time constants τ_1 and τ_2 can be determined so as to minimize the mean square value of the difference between $U_{\mathrm{g}1}$ and $U_{\mathrm{g}2}$, which is given by

$$e = \overline{(U_{\mathrm{g}2} - U_{\mathrm{g}1})^2}. \tag{2.10}$$

The time-constant estimation method thus obtained was originally proposed by Tagawa and Ohta (1997). In what follows, we call this estimation scheme the "e_{min} method." The time derivatives of $\mathrm{d}U_1/\mathrm{d}\tau$ and $\mathrm{d}U_2/\mathrm{d}\tau$ in Eq. (2.9) are defined as G_1 and G_2, and also $\Delta U_{21} = U_2 - U_1$, velocity difference between the CCA fine-wires. And then Eq. (2.9) can be expended into

$$e = \overline{\Delta U_{21}^2} + \overline{G_1^2}\tau_1^2 + \overline{G_2^2}\tau_2^2 - 2\overline{G_1 \Delta U_{21}}\tau_1 + 2\overline{G_2 \Delta U_{21}}\tau_2 - 2\overline{G_1 G_2}\tau_1\tau_2. \tag{2.11}$$

Then, the time constants τ_1 and τ_2 can be obtained from the simultaneous equation derived from Eq. (2.11) by minimizing the value of e as the following conditions:

$$\frac{\partial e}{\partial \tau_1} = 0, \frac{\partial e}{\partial \tau_2} = 0. \tag{2.12}$$

The result is given by the following equations:

$$\begin{aligned} \tau_1 &= \frac{\overline{G_2^2} \cdot \overline{G_1 \Delta U_{21}} - \overline{G_1 G_2} \cdot \overline{G_2 \Delta U_{21}}}{\overline{G_1^2} \cdot \overline{G_2^2} - (\overline{G_1 G_2})^2}, \\ \tau_2 &= \frac{\overline{G_1 G_2} \cdot \overline{G_1 \Delta U_{21}} - \overline{G_1^2} \cdot \overline{G_2 \Delta U_{21}}}{\overline{G_1^2} \cdot \overline{G_2^2} - (\overline{G_1 G_2})^2}, \end{aligned} \tag{2.13}$$

R_{max} method

In a case where there is a low spatial resolution of the two-sensor probe and/or a low signal-to-noise ratio of the measurement system, we can take another approach to estimate the time-constant values by maximizing the correlation coefficient R between $U_{\mathrm{g}1}$ and $U_{\mathrm{g}2}$:

$$R = \frac{\overline{U'_{\mathrm{g}1}U'_{\mathrm{g}2}}}{\sqrt{\overline{U'^2_{\mathrm{g}1}}}\sqrt{\overline{U'^2_{\mathrm{g}2}}}}, \tag{2.14}$$

where the prime denotes a fluctuating component. By expressing U_g and G as mean and fluctuating components: $U_{\mathrm{g}} = \overline{U_{\mathrm{g}}} + U'_{\mathrm{g}}$ and $G = \overline{G} + G'$ and putting into Eq. (2.9), we get the relations $U'_{\mathrm{g}1} = U_{\mathrm{g}1} - \overline{U_{\mathrm{g}1}} = U'_1 + \tau_1 G'_1$ and $U'_{\mathrm{g}2} = U_{\mathrm{g}2} - \overline{U_{\mathrm{g}2}} = U'_2 + \tau_2 G'_2$. By substituting these relations into Eq. (2.14), it becomes the following:

$$\begin{aligned}
\overline{U'^2_{\mathrm{g}1}} &= \overline{U'^2_1} + 2\overline{G'_1U'_1}\tau_1 + \overline{G'^2_1}\tau_1^2, \\
\overline{U'^2_{\mathrm{g}2}} &= \overline{U'^2_2} + 2\overline{G'_2U'_2}\tau_2 + \overline{G'^2_2}\tau_2^2, \\
\overline{U'_{\mathrm{g}1}U'_{\mathrm{g}2}} &= \overline{U'_1U'_2} + \overline{G'_1U'_2}\tau_1 + \overline{G'_2U'_1}\tau_2 + \overline{G'_1G'_2}\tau_1\tau_2.
\end{aligned} \tag{2.15}$$

The time constants, τ_1 and τ_2, will satisfy the following conditions:

$$\frac{\partial R}{\partial \tau_1} = 0, \frac{\partial R}{\partial \tau_2} = 0. \tag{2.16}$$

By solving a simultaneous equation thus derived, we obtain the time constants τ_1 and

τ_2 as a solution of quadratic equations:

$$\begin{aligned} \tau_1 &= \left(-B_1 + \sqrt{B_1^2 - 4C_1}\right)/2, \\ \tau_2 &= \left(-B_2 + \sqrt{B_2^2 - 4C_2}\right)/2. \end{aligned} \tag{2.17}$$

The quantities B_1, B_2, C_1 and C_2 in Eq. (2.17) are given by

$$\begin{aligned} B_1 &= \frac{\langle a_1, d_1\rangle + \langle b_1, c_1\rangle}{\langle b_1, d_1\rangle}, \quad B_2 = \frac{\langle a_2, d_2\rangle + \langle c_2, b_2\rangle}{\langle c_2, d_2\rangle}, \\ C_1 &= \frac{\langle a_1, c_1\rangle}{\langle b_1, d_1\rangle}, \quad C_2 = \frac{\langle a_2, b_2\rangle}{\langle c_2, d_2\rangle}, \end{aligned} \tag{2.18}$$

and all the elements in Eq. (2.18) are given by

$$\begin{aligned} a_1 &= \overline{U_1'^2} \cdot \overline{G_1'U_2'} - \overline{U_1'U_2'} \cdot \overline{G_1'U_1'}, \\ a_2 &= \overline{U_2'^2} \cdot \overline{G_2'U_1'} - \overline{U_1'U_2'} \cdot \overline{G_2'U_2'}, \\ b_1 &= \overline{G_1'U_1'} \cdot \overline{G_1'U_2'} - \overline{U_1'U_2'} \cdot \overline{G_1'^2}, \\ b_2 &= \overline{U_2'^2} \cdot \overline{G_1'G_2'} - \overline{G_1'U_2'} \cdot \overline{G_2'U_2'}, \\ c_1 &= \overline{U_1'^2} \cdot \overline{G_1'G_2'} - \overline{G_1'U_1'} \cdot \overline{G_2'U_1'}, \\ c_2 &= \overline{G_2'U_1'} \cdot \overline{G_2'U_2'} - \overline{U_1'U_2'} \cdot \overline{G_2'^2}, \\ d_1 &= \overline{G_1'U_1'} \cdot \overline{G_1'G_2'} - \overline{G_2'U_1'} \cdot \overline{G_1'^2}, \\ d_2 &= \overline{G_2'U_2'} \cdot \overline{G_1'G_2'} - \overline{G_1'U_2'} \cdot \overline{G_2'^2}. \end{aligned} \tag{2.19}$$

In the present study, we have mainly used this approach called the "$R_{\max}$ method" (Tagawa *et al.* 1998). It is noted that the time derivatives in Eqs. (2.13) and (2.19) can be obtained from the coefficients of a polynomial curve-fitting (Tagawa et al. 2001) for the digitized outputs of the two unequal hot-wires driven at the CCA mode.

2.3 Experimental apparatus and measurement system

2.3.1 Single-sensor and two-sensor probes

In this experiment, we used three fine tungsten wires 5 μm, 10 μm and 20 μm in diameter for the CCA, and a 5 μm tungsten wire for the CTA, which was used as a reference sensor. The detailed features of the fine-wires are given in Table 2.1. For the two-sensor technique, we have constructed two types of the CCA probes—one is the combination of 5 and 10 μm hot-wires, and the other is that of 10 and 20 μm ones. The schematic diagram of the constant-current circuit for driving a 5 μm or 10 μm wire is shown in Fig. 2.3 (a), and that for a 20 μm wire in Fig. 2.3 (b). The driving circuit for 5 μm and 10 μm wires is very simple and can be composed at quite a low cost. On the other hand, a different circuit [shown in Fig. 2.3 (b)] should be used for a 20 μm wire, since the current needs to be kept accurately constant even in case of a higher electric current. The later circuit, of course, can be used for driving a thinner wire, and is still much simpler to operate than the constant-temperature anemometer. The configuration and arrangement of the hot-wires consisting of single-sensor and two-sensor probes are shown (circled) in Fig. 2.4. We have determined a proper wire separation so as to minimize thermal and fluid-dynamical interferences between the two hot-wires.

2.3.2 Experimental apparatus and measurement system

As shown in Fig. 2.4, the flow field to be measured is a turbulent far wake of a circular cylinder, and the test section is the $y \geq 0$ mm region in the central plane ($z = 0$ mm) at $x/D = 8$. A uniform airflow up to 12 m/s can be produced using an upright wind tunnel with a two-dimensional contraction (contraction ratio, 5:1), and approaches to the cylinder set at the wind tunnel exit. It is noted that 5 $\sim$ 10 % free stream turbulence is generated by a perforated plate (hole size: ϕ 5 mm; staggered arrangement with 7 mm pitch). In the present experiment, the uniform airflow velocity was set to 7 m/s.

All the outputs of the hot-wires driven by the constant-current circuits shown in Fig. 2.3 are amplified by 100 $\sim$ 500 times and digitized by a 14-bit A/D converter (Microscience ADM-670 and/or 681PCI). The sampling frequency is set at 10 kHz and the number of samples is 132,000 for each measurement. A personal computer (EPSON Endeavor Pro3100) is used to store the hot-wire outputs of the A/D converter and perform all the data processing. The hot-wire outputs are calibrated with the aid of a pitot tube in the range of 1 to 10 m/s.

2.4 Results and discussion

2.4.1 Theoretical response compensation for single-sensor measurement

First, we estimated the frequency response of the hot-wires 5 μm, 10 μm and 20 μm in diameter to apply the theoretical response compensation scheme mentioned in section 2.2.1 to the CCA outputs.

Naturally, the mean velocity profiles obtained by these three hot-wires show little difference (a sample velocity profile is seen in Fig. 2.11). Then, we appraised experimentally the effectiveness of the theoretical response compensation of the CCA on the basis of the turbulence intensities (root-mean-square values) and power spectra of the velocity fluctuations of the turbulent wake flow. The results are shown in Figs. 2.5 and 2.6. Figure 2.5 shows the root-mean-square (r.m.s.) velocities of the uncompensated (raw) and compensated CCA outputs in comparison to the CTA results used as reference data. As seen from Fig. 2.5, all the three compensated r.m.s. profiles are generally in good agreement with the CTA data. On the other hand, Fig. 2.6 shows the uncompensated and compensated power spectra of the CCA data measured at $y = 16$ mm, where the r.m.s. profiles indicate the peak values. As seen from the comparison between the uncompensated and compensated power spectra, the CCA outputs start to attenuate at about 200 Hz, 70 Hz and 20 Hz for the 5 μm, 10 μm and 20 μm hot-wire data, respectively. These behaviors of the uncompensated power spectra can be well

Table 2.2 Time-constant values estimated from $e_{\min}$ method, $R_{\max}$ method and Collis-Williams law given by Eq. (A13) ($y = 16$ mm)

	Probe 1 ($\overline{U} = 5.0$ m/s)		Probe 2 ($\overline{U} = 5.9$ m/s)	
	τ_1[ms]	τ_2[ms]	τ_1[ms]	τ_2[ms]
Scheme	d_1: 5 μm	d_2: 10 μm	d_1: 10 μm	d_2: 20 μm
$e_{\min}$ method	0.57	2.07	1.64	6.20
$R_{\max}$ method	0.66	2.13	2.06	7.55
Collis-Williams	0.64	2.12	2.02	7.47

explained by the Bode (gain) diagrams shown in Fig. 2.2, and the compensated power spectra agree well with the CTA result up to sufficiently high-frequencies. It is noted that, in the present study, we have applied a finite-impulse-response (FIR) digital filter to the compensated CCA outputs in order to cut off the frequency components higher than 4.5 kHz, 3 kHz and 2 kHz for the 5 μm, 10 μm and 20 μm hot-wire outputs, respectively. As seen from the above, the proposed theoretical response compensation scheme works quite well.

2.4.2 Adaptive response compensation by the two-sensor technique

Before applying the two-sensor technique to the present experiment, we investigated the frequency response of the three hot-wires 5 μm, 10 μm and 20 μm in diameter to confirm that the response characteristics of these hot-wires can be approximated by the first-order lag system as explained in section 2.2.1. Then, we estimated the time-constant values by the $e_{\min}$ and $R_{\max}$ methods described in section 2.2.2. The results obtained at $y = 16$ mm are summarized in Table 2. As seen from Table 2.2, the time-constant values estimated by both Probe 1 and Probe 2 using the $R_{\max}$ method are in good agreement with those obtained from the correlation equation proposed by Collis and Williams (1959). Figure 2.7 shows the compensated r.m.s. velocity distributions obtained by Probe 2 using the $R_{\max}$ method (results obtained by Probe 1 is omitted due to space limitation). As seen from Fig. 2.7, the present response compensation scheme works successfully and can provide acceptable results that are comparable to the CTA measurements, except the centerline region around $y = 0$ mm. This slight discrepancy near the centerline may be caused by an increase of thermal and/or fluid-dynamic interferences between the two hot-wires of the two-sensor probe shown in Fig. 2.4.

The power spectra of both uncompensated and compensated velocity fluctuations measured at $y = 16$ mm are shown in Fig. 2.8, where we also compared their distributions with those obtained by the CTA. In the present experiment, we removed high-frequency noise components in the compensated CCA outputs using a finite-impulse-response (FIR) digital filter with the cutoff frequency of 3 kHz for the 10 μm hot-wire and 2 kHz for the 20 μm one. As seen from Fig. 2.8, the power spectra of the compensated CCA outputs agree well with the CTA result, and high-frequency velocity fluctuations up to around 2 kHz can be well reproduced. Meanwhile, Fig. 2.9 shows a comparison of the instantaneous signal trace between the uncompensated and compensated CCA outputs measured at $y = 16$ mm, with a reference of the CTA output. The CTA and CCA outputs were measured independently (they are not simultaneous measurements). As seen from Fig. 2.9 (b), high-frequency velocity fluctuations have been recovered properly by the present response compensation scheme. As a result, the compensated CCA signal traces are analogous to the CTA one shown in Fig. 2.9 (a).

2.5 Application of response compensation technique to multi-sensor measurement

2.5.1 Multi-sensor probe

Multipoint measurement and analysis will help us elucidate the spatiotemporal structures of turbulent flows. Thus, in the present study, we have explored the possibilities of applying the above-mentioned response compensation scheme to the multi-sensor probe driven at the CCA mode, since the constant electric-current circuit driving the hot-wires, e.g., Fig. 2.3 (a), is much simpler and can be constructed at an even lower cost than the constant-temperature anemometer (CTA).

Figure 2.10 shows the photographs of the multi-sensor probe constructed in our laboratory. As shown in Fig. 2.10, sixteen tungsten hot-wires 5 μm in diameter with copper plated ends are aligned at intervals of 2 mm and soldered on steel prong tips. The configuration of the 5 μm hot-wire is the same as that given in Table 1, and the entire length of the sensing part becomes 30 mm. The present muti-sensor probe was designed so as to measure adequately the turbulent far wake of a cylinder (Fig. 2.4). The probe was set at the same hight as the above experiment ($x = 80$ mm) with the probe tip positioned at $y = 0$ mm. When the airflow velocity at the wind-tunnel exit is 7 m/s and the probe is set at $x/D = 8$ (cylinder diameter: $D = 10$ mm), the mean velocity profile in the y-direction can be sufficiently covered by the measurement range of $0 \leq y \leq 30$ mm. We used the constant-current circuit shown in Fig. 2.3 (a) for driving the sixteen tungsten hot-wires 5 μm in diameter.

2.5.2 Multipoint measurement

The multipoint measurement by the 16-channel CCA probe was performed in the turbulent far wake of the cylinder (Fig. 2.4). Figure 2.11 shows the comparison between the mean velocity profile measured by the multi-sensor probe and that obtained using the single hot-wire driven by the CTA. As seen from Fig. 2.11, the uncompensated (raw) mean velocities of the multipoint measurement are almost coincident with the CTA measurements. Naturally, as for the measurement of the mean velocity profile, the response compensation scheme need not necessarily be applied to the CCA outputs. Meanwhile, Fig. 2.12 shows the comparison of r.m.s. velocity distributions between the multipoint measurements and the CTA result. In the present response compensation, the frequency components higher than 4.5 kHz were attenuated by a finite-impulse-response (FIR) digital low-pass filter. As seen from Fig. 2.12, the r.m.s velocities of the multi-sensor measurements compensated by using Eq. (2.8) are in good agreement with those obtained by the CTA. Thus, a multi-sensor probe with the present response compensation scheme (section 2.2.1) will work successfully to detect spatiotemporal behaviors of turbulent flow fields.

The instantaneous signal traces measured by the multi-sensor probe are shown in Fig. 2.13. Figure 2.13 (a) shows the uncompensated (raw) outputs of the 16 hot-wires of the multi-sensor probe, in which the hot-wires are arranged at the constant intervals of 2 mm, and the cylinder was placed at $y = 0$ mm (see Figs. 2.11 and 2.12). As seen from Fig. 2.13 (a), the mean velocity changes largely in the region of $0 \leq y \leq 20$ mm, and the mean velocity gradient in the y direction is barely observed in the region of $y \geq$ 20 mm. On the other hand, Fig. 2.13 (b) shows the compensated signal traces. As seen from Fig. 2.13 (b), the response compensation has reproduced high-frequency velocity fluctuations and has made it evident that large-scale fluid motions exist through the shear layer of the turbulent far wake of the cylinder. Thus, the multi-sensor probe driven by the CCA together with the digital response compensation scheme will provide a useful tool for investigating spatiotemporal structures of turbulent flows.

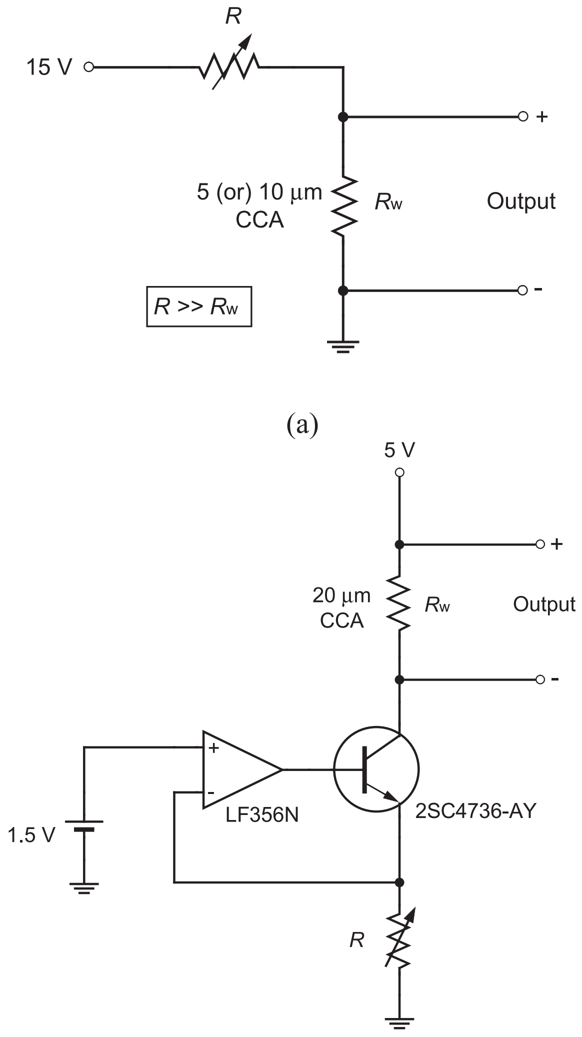
R
15 V
+
5 (or) 10 µm
CCA
Rw
Output
-
R >> Rw
5 V
+
20 µm
CCA
Rw
Output
-
+
-
LF356N
1.5 V
2SC4736-AY
R

(a)

(b)

Figure 2.3 Schematic diagrams of constant-current circuits for driving three different tungsten hot-wires 5, 10 and 20 μm in diameter: (a) driving circuit for 5 and 10 μm wires. Resistance values R_w of 5 μm wire (length: 1.5 mm) and 10 μm one (length: 2 mm) are 5.5 $\sim$ 6.5 Ω and 2 $\sim$ 3 Ω, respectively, at room temperature. Driving currents for 5 μm and 10 μm wires were 40 mA and 100 mA, respectively; (b) driving circuit for 20 μm wire. The resistance value R_w of 20 μm wire (length: 4 mm) is 1 $\sim$ 2 Ω at room temperature. The driving current was 260 mA.

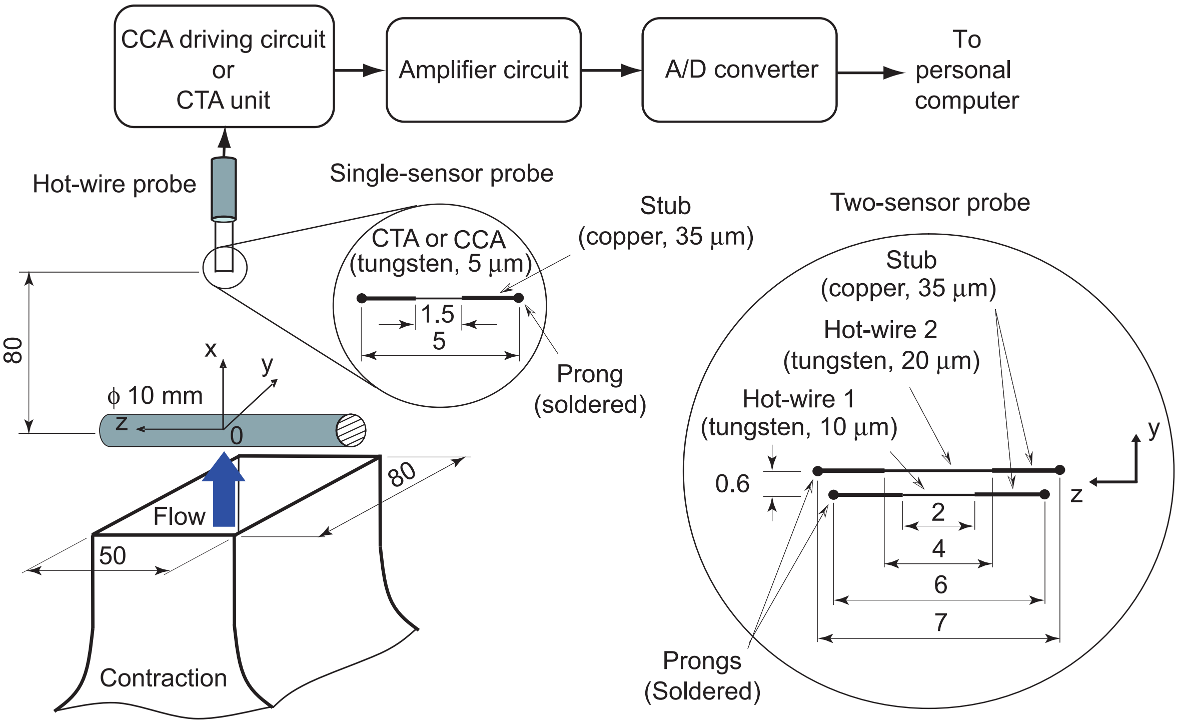
CCA driving circuit
or
CTA unit
Amplifier circuit
A/D converter
To
personal
computer
Hot-wire probe
Single-sensor probe
CTA or CCA
(tungsten, 5 µm)
1.5
5
Stub
(copper, 35 µm)
Prong
(soldered)
Two-sensor probe
Stub
(copper, 35 µm)
Hot-wire 2
(tungsten, 20 µm)
Hot-wire 1
(tungsten, 10 µm)
0.6
2
4
6
7
y
z
Prongs
(Soldered)
80
x
y
ϕ 10 mm
z
0
80
Flow
50
Contraction

Figure 2.4 Experimental apparatus and details of hot-wire probes (single-sensor and two-sensor probes). The 10 μm and 20 μm hot-wire sensors shown in the two-sensor probe can be used for the single-sensor probe. For the two-sensor probe, we employed two combinations: Probe 1 is the combination of 5 μm and 10μm hot-wires; Probe 2 (circled) is that of 10 μm and 20μm ones. (All dimensions in millimeters.)

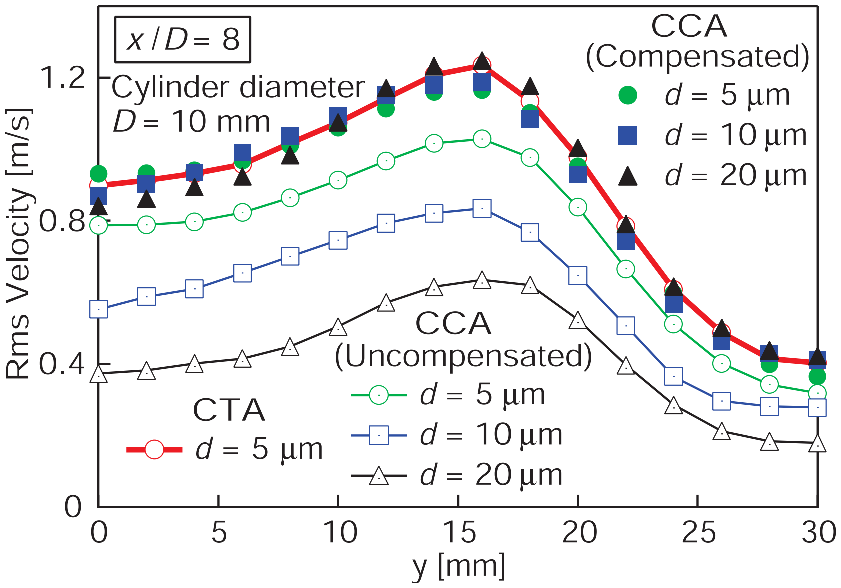

Figure 2.5 Comparison of rms velocity profile between single-wire CCA measurements by 5 μm, 10 μm and 20 μm hot-wires and reference measurement by CTA.

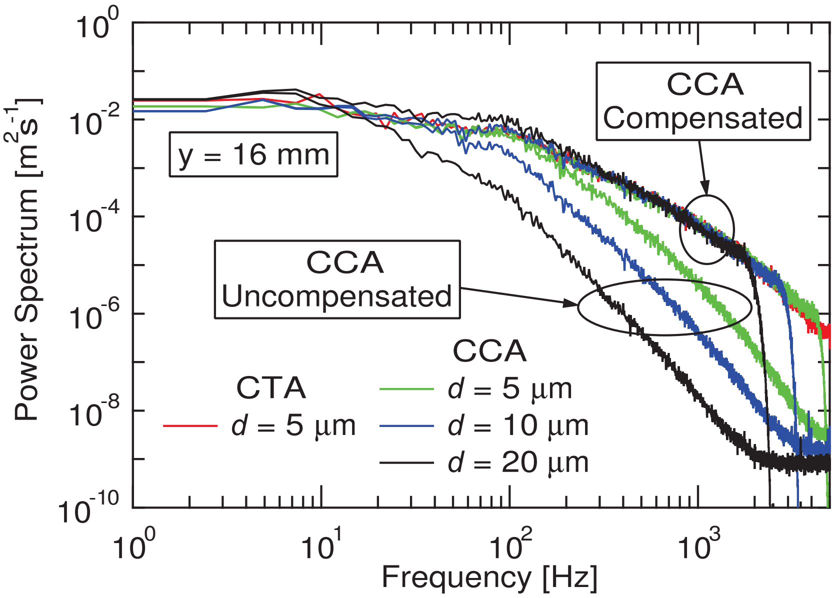

Figure 2.6 Power spectra of velocity fluctuations measured using three single-sensor probes driven by CCA and that by CTA at $y = 16$ mm where the turbulent intensities take their maxima.

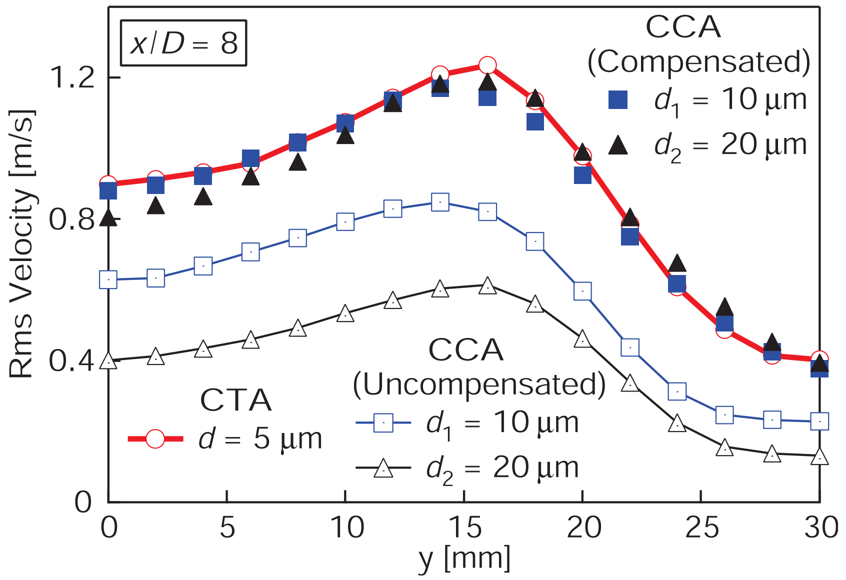

Figure 2.7 Rms velocities obtained by two-sensor technique using R_{max} method (Probe 2).

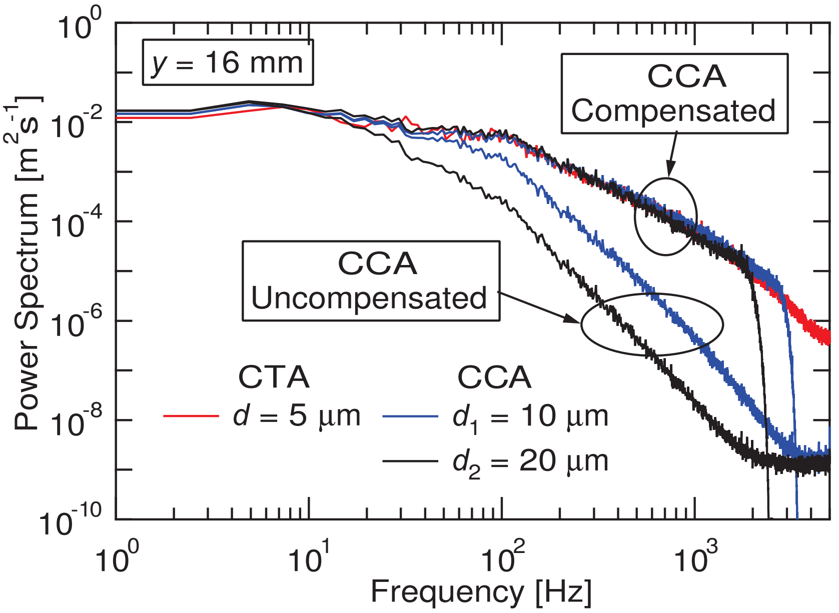

Figure 2.8 Comparison of power spectrum distribution using two-sensor technique using R_{max} method (Probe 2).

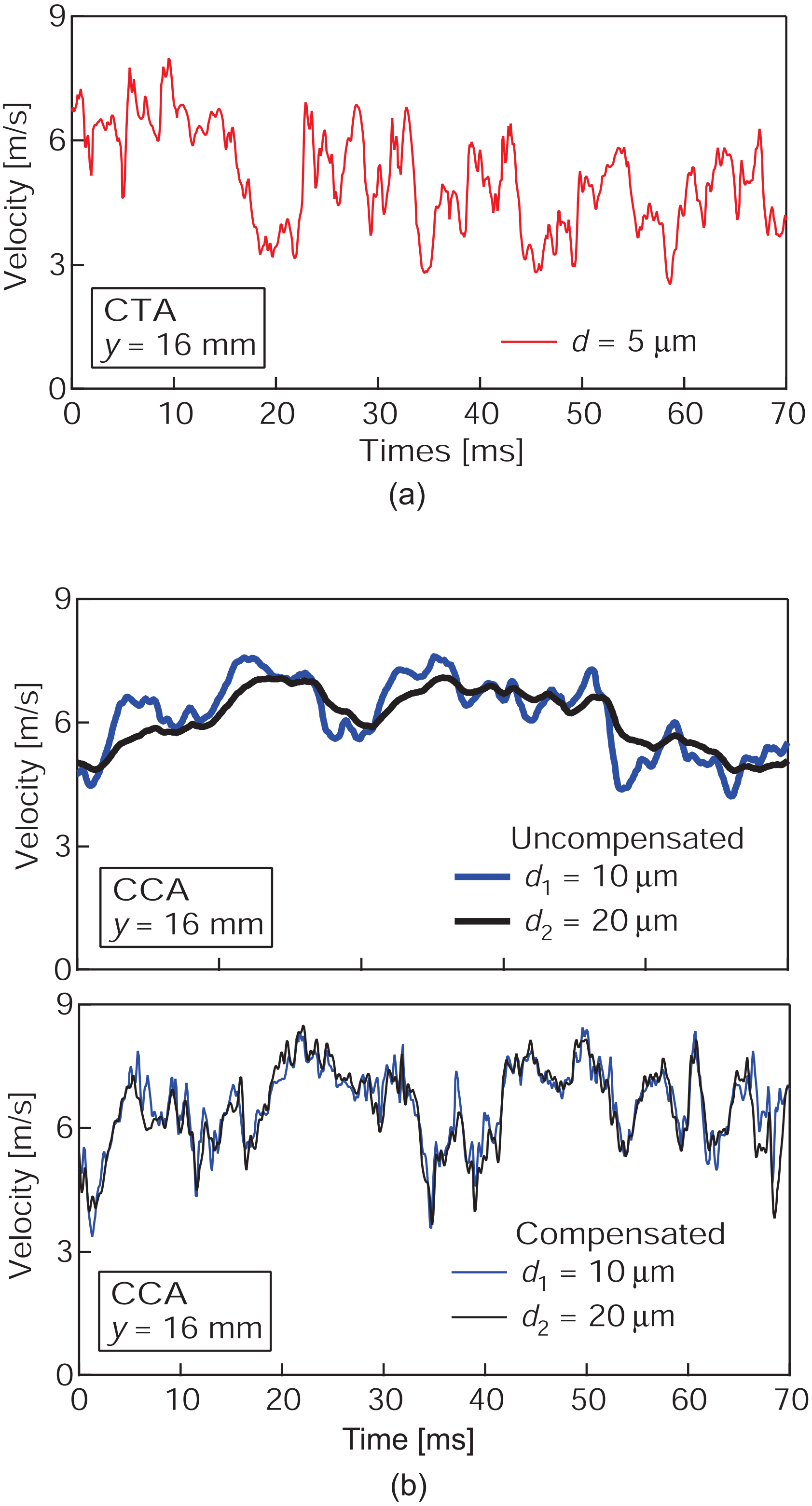

Figure 2.9 Instantaneous signal traces of velocity fluctuations: (a) CTA measurement by single-sensor probe; (b) CCA measurements by two-sensor probe. The CTA and CCA outputs were measured independently (they are not simultaneous measurements).

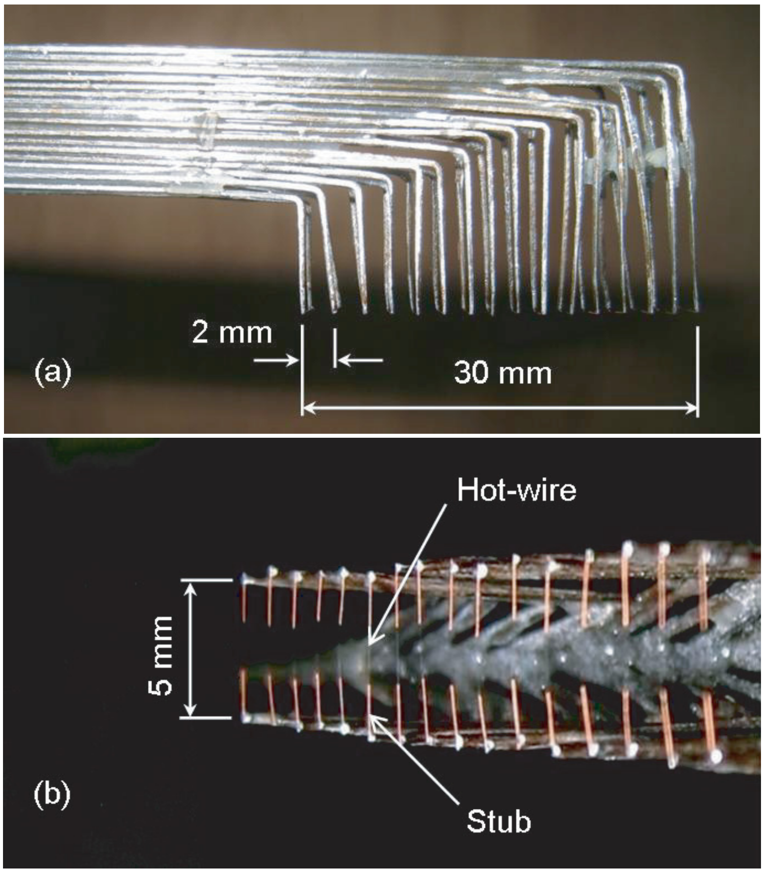
2 mm
(a)
30 mm
Hot-wire
5 mm
(b)
Stub

Figure 2.10 Multi-sensor probe consisting of sixteen 5 μm hot-wires driven at CCA mode: (a) Side view; (b) Front view.

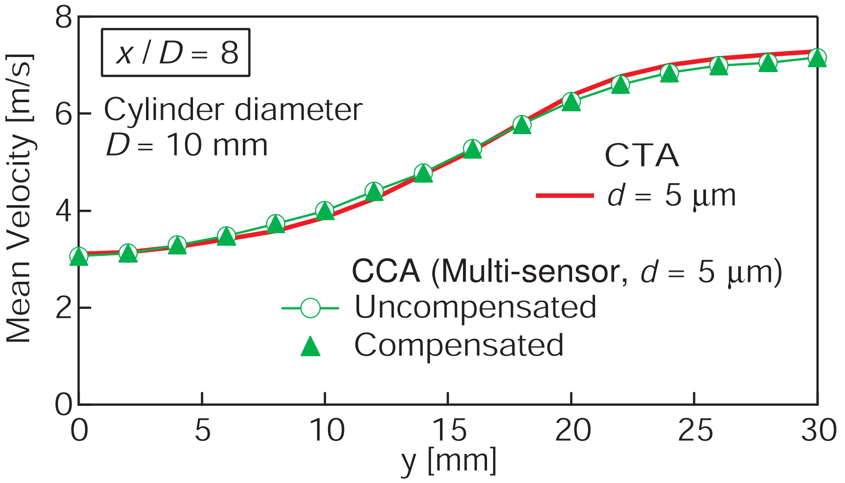

Figure 2.11 Mean velocity profiles of single-sensor measurement by CTA and multipoint measurement by CCA. Cylinder is positioned at $y = 0$ mm.

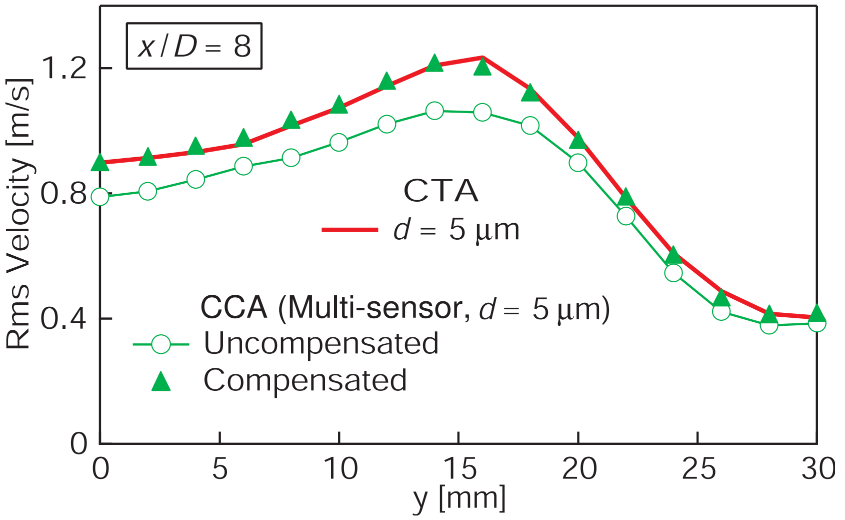

Figure 2.12 Comparison of rms velocity distributions of single-sensor measurement by CTA and multipoint measurement by CCA.

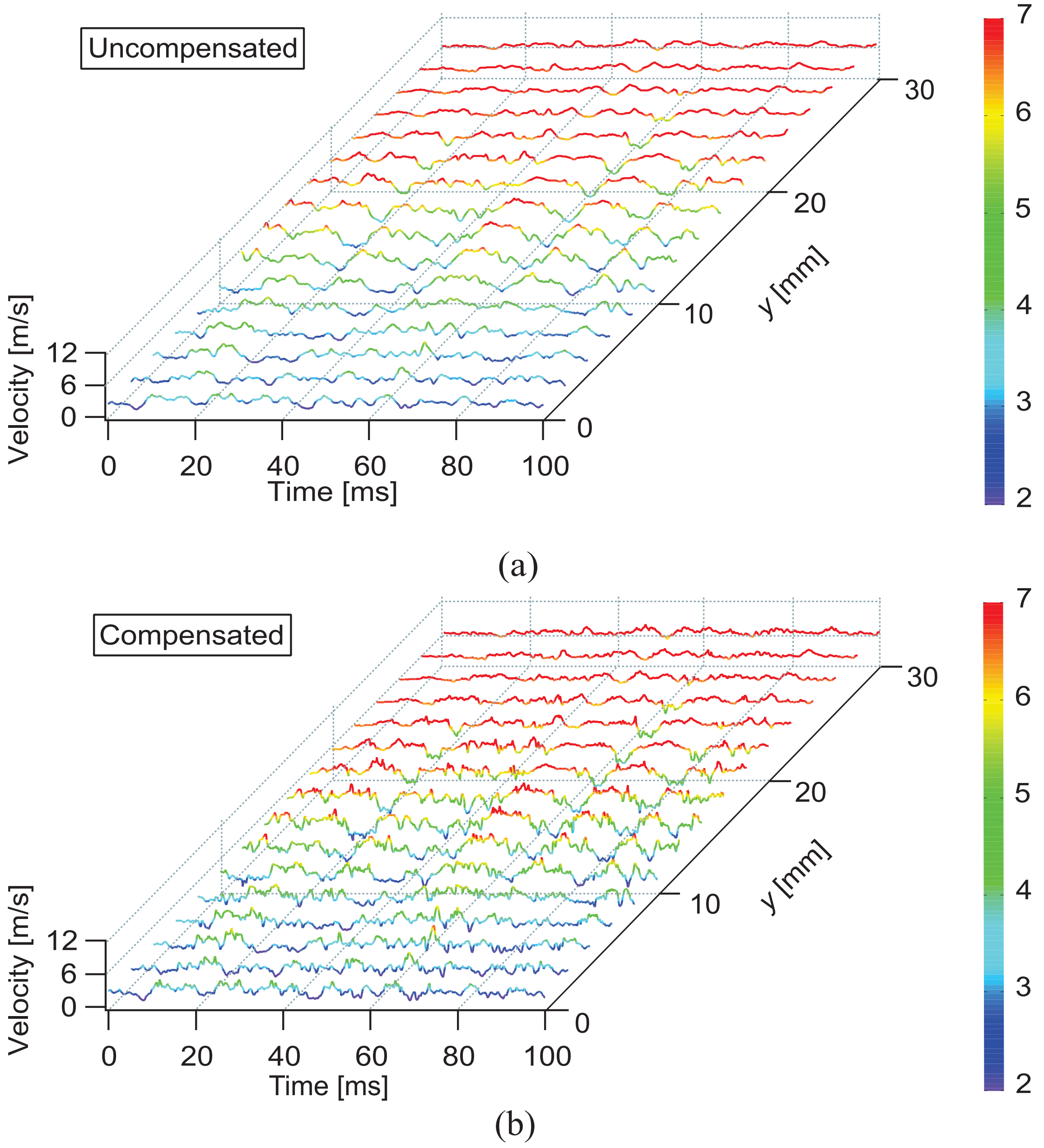

(a)

(b)

Figure 2.13 Instantaneous signal traces of multipoint measurement: (a) Uncompensated (raw) outputs; (b) Compensated results by theoretical response compensation scheme using Eq. (2.8).

Chapter 3

Heat-conduction error of temperature sensors in a fluid flow with nonuniform and unsteady temperature distribution

3.1 Theoretical analysis of heat-conduction error of temperature sensor

3.1.1 Physical model of temperature sensor

In the present study, we analyze theoretically the heat-conduction error of temperature sensors whose shape can be represented as a thin cylinder like a fine-wire thermocouple, a sheath-type one, resistance-temperature detector, etc. As shown in Fig. 3.1, heat balance of a minute fraction Δx [m] of a thin cylinder of diameter d

[m], which is placed in a flow with velocity U [m/s] and temperature T_a [K], can be expressed by the following equation.

$$\rho\left(\frac{\pi}{4}d^2\Delta x\right)c\Delta T_\mathrm{w} = \left[h(\pi d\Delta x)(T_\mathrm{a}-T_\mathrm{w}) + \left(\frac{\pi}{4}d^2\right)\lambda \left.\frac{\mathrm{d}^2T_\mathrm{w}}{\mathrm{d}x^2}\right|_x \Delta x\right]\Delta t, \tag{3.1}$$

where T_w and ΔT_w are the cylinder temperature and its change, respectively, and Δt denotes time [s]. Furthermore, d, h and x are the cylinder diameter [m], heat transfer coefficient [W/(m^2·K)] and the coordinate along the cylinder axis [m], and c, ρ and λ denote respectively the specific heat [J/(kg·K)], density [kg/m^3] and thermal conductivity [W/(m·K)] of the cylinder material. In Eq. (3.1), heat conduction in the radial direction of the cylinder, radiative heat transfer and the effects of surface coating and/or filling material are not taken into account. The effects of the radial-direction heat conduction, surface coating and filling material on dynamic characteristics of temperature sensors can be found in our previous papers, (Tagawa *et al.* 2003, Kato *et al.* 2007) and those of the radiative heat transfer were also investigated in our previous study (Tagawa and Ohta 1997).

The left-hand side of Eq. (3.1) shows accumulated heat in the fraction Δx during minute time Δt, and the first and second terms on the right-hand side represent, respectively, convective heat transfer between the cylinder surface and ambient fluid and the difference in heat conduction between the left and right sides of the fraction Δx. When Δt and Δx is approaching zero, Eq. (3.1) can be written in the following

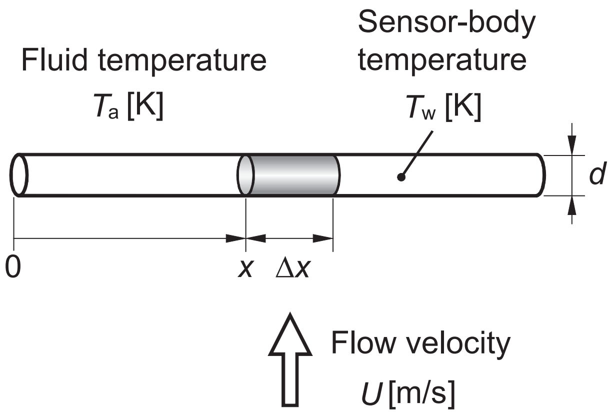

Figure 3.1 Configuration of a cylindrical temperature sensor.

form:

$$\begin{aligned}\frac{\partial T_{\mathrm{w}}}{\partial t} &= \frac{4h}{\rho c d}(T_{\mathrm{a}} - T_{\mathrm{w}}) + \frac{\lambda}{\rho c}\frac{\partial^2 T_w}{\partial x^2} \\ &= \frac{1}{\tau}(T_{\mathrm{a}} - T_{\mathrm{w}}) + a\frac{\partial^2 T_w}{\partial x^2},\end{aligned} \tag{3.2}$$

where a denotes thermal conductivity of the cylinder material [$= \lambda/(\rho c)$], and τ is a time constant (thermal time constant) defined by the following equation.

$$\tau = \frac{\rho c d}{4h}. \tag{3.3}$$

In a steady flow, since the left-hand side of Eq. (3.2) becomes zero, the heat balance of the cylinder can be expressed by the second-order ordinary differential equation as follows:

$$\frac{\mathrm{d}^2 T_{\mathrm{w}}}{\mathrm{d}x^2} - \frac{T_{\mathrm{w}}}{a\tau} = -\frac{T_{\mathrm{a}}}{a\tau}. \tag{3.4}$$

The governing parameter of Eq. (3.4) is $a\tau$, which can be represented by the so-called ‘cold length’ defined by

$$L_{\mathrm{c}} = \sqrt{a\tau}. \tag{3.5}$$

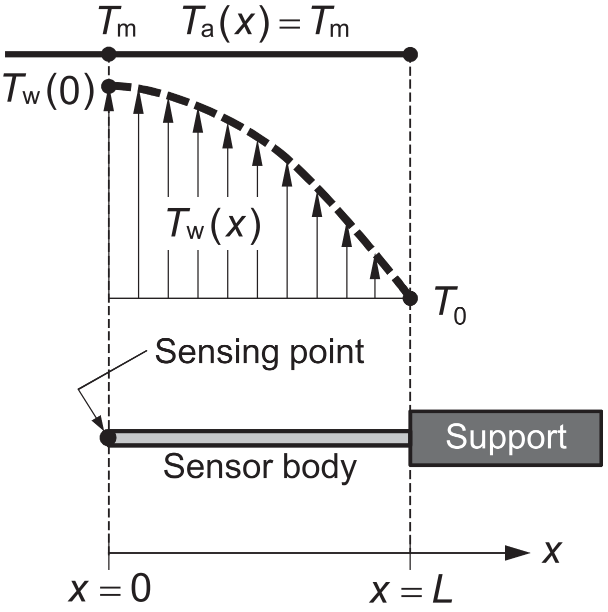

Figure 3.2 Conventional analytical model of heat-conduction error in measurement of uniform fluid temperature.(Sparrow 1976)

Consequently, the theoretical analysis of the heat-conduction error in fluid temperature measurement is to be performed based on the following equation.

$$\frac{\mathrm{d}^2 T_\mathrm{w}}{\mathrm{d}x^2} - \frac{T_\mathrm{w}}{L_\mathrm{c}^2} = -\frac{T_\mathrm{a}}{L_\mathrm{c}^2} \tag{3.6}$$

In the present analysis, it is assumed that the physical properties of the fluid and sensor material are kept constant, and the diameter d and flow velocity U do not change in the axial direction of the cylinder. Namely, the heat-conduction error is to be estimated theoretically based on the assumption that the heat transfer coefficient h and the cold length L_c are uniform in the x direction.

3.1.2 Theoretical analysis model for heat-conduction error in temperature measurement of fluid flows without temperature gradient

As stated in the introduction, Sparrow (1976) proposed a simple and useful theoretical formula for estimating the heat-conduction error, which was derived using the physical model shown in Fig. 3.2 on the assumption that fluid temperature is uniform at T_m and measured through a solid wall kept at a constant temperature T_0. In Fig. 3.2, the sensing part is located at the tip of the sensor body ($x = 0$), which applies to a sheathed thermocouple or a pair of thermocouple wires welded at $x = 0$ (junction/bead)—the shape resembles a pair of pine needles. In the present analysis, $T_\mathrm{a}(x)$ denotes the temperature profile of a fluid flow, and T_m the fluid temperature at the measurement position ($x = 0$), which should be treated as a true value. Then, a uniform fluid-temperature profile along the sensor body can be expressed as $T_\mathrm{a}(x) = T_\mathrm{m}$. On the other hand, when representing the temperature distribution of the sensor body as $T_\mathrm{w}(x)$, $T_\mathrm{w}(0)$ corresponds to the measured value (sensor output) and the temperature at the interface between the sensor body and its support ($x = L$) is to be fixed at a temperature of the flow channel wall as $T_\mathrm{w}(L) = T_0$.

When solving the differential equation (3.6) under the boundary conditions that the sensor body is adiabatic at $x = 0$ ($\mathrm{d}T_\mathrm{w}/\mathrm{d}x = 0$) and its temperature at $x = L$ is fixed at T_0, we can obtain the sensing-part temperature $T_\mathrm{w}(0)$ (sensor output) as

$$\frac{T_\mathrm{w}(0) - T_0}{T_\mathrm{m} - T_0} = 1 - \frac{1}{\cosh(L/L_\mathrm{c})}. \tag{3.7}$$

The derivation process of Eq. (3.7) is essentially identical to heat transfer analysis of a thin rod fin, while the direction of heat conduction is opposite. Equation (3.7) shows that the heat-conduction error is dominated by the ratio of the length of the sensor body L to the cold length L_c and the heat-conduction error will diminish with increasing L and decreasing L_c.

As seen from Eqs. (3.3) and (3.5), for example, when physical properties of the working fluid and sensor material are constant and the sensor length L is kept unchanged, the heat-conduction error will diminish with decreasing cold length L_c. This can be realized by decreasing the sensor diameter d and increasing the heat-transfer coefficient h (i.e., increasing the flow velocity U). However, when applying Eq. (3.7) to a flow with temperature gradient, the heat-conduction error will be generally underestimated as shown in section 3.1.4, since Eq. (3.7) was derived on condition that the fluid temperature has a uniform distribution along the sensor body. To be more specific, if the fluid temperature decreases in the positive direction of the x-axis, the convective heat transfer from the fluid to the sensor body—the first term of the right-hand side of Eq. (3.1)—becomes smaller than that for the uniform fluid temperature case shown in Fig. 3.2. This makes it more difficult to maintain the sensing-part temperature $T_\mathrm{w}(0)$ at the fluid temperature (true value) T_m to be measured. Thus, in the following, we try to extend the above theoretical approach to derive a new formula which enables more accurate estimation of the heat-conduction error in the presence of the temperature gradient in a non-isothermal fluid flow. In the present study, we introduce a non-dimensional temperature Θ_0 to measure the heat-conduction error quantitatively.

$$\Theta_0 = \frac{T_\mathrm{w}(0) - T_0}{T_\mathrm{m} - T_0}. \tag{3.8}$$

Consequently, when the sensing-part temperature $T_\mathrm{w}(0)$ coincides with the fluid temperature at the measurement position $T_\mathrm{m} = T_\mathrm{a}(0)$, Θ_0 becomes unity ($\Theta_0 = 1$). Namely, the heat-conduction error diminishes as Θ_0 approaches unity.

3.1.3 Present theoretical model for heat-conduction error in temperature measurement of fluid flows with temperature gradient

In general, in temperature measurement of fluid flows, there exist temperature gradients in the thermal field. Then, if the axis of the sensor body is set in the direction of the temperature gradient, the temperature measurements are more likely to be subject to larger heat-conduction error than that predicted by Eq. (3.7) for the reason noted in section 3.1.2. Therefore, in this section, we analyze theoretically the heat-conduction error in temperature measurement of a fluid flow with temperature gradient by using the physical model shown in Fig. 3.3.

In the present model, we assume that a fluid temperature is measured using a thin

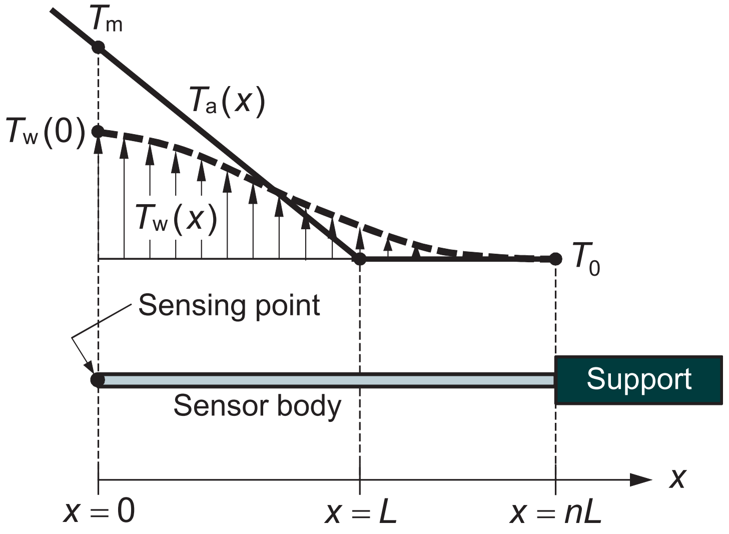

Figure 3.3 Proposed analytical model of heat-conduction error in measurement of non-uniform fluid temperature.

rod-shaped sensor, which has a diameter of d and is inserted into a non-isothermal flow field having a temperature distribution $T_{\mathrm{a}}(x)$ under the condition of uniform flow velocity. Then, as in Fig. 3.2, the tip of the sensor body is the detecting point and its temperature $T_{\mathrm{w}}(0)$ represents the sensing-part temperature (sensor output). As shown in Fig. 3.3, the fluid temperature distribution $T_{\mathrm{a}}(x)$ decreases linearly with x from the fluid temperature at the detecting point ($x = 0$) T_{m} and reaches an ambient fluid temperature T_0 at $x = L$. In the region of $x \geq L$, the fluid temperature has a uniform distribution as $T_{\mathrm{a}}(x) = T_0$. In the present analysis, we introduce a parameter n ($n \geq 1$) to specify the position of the sensor support located at $x = nL$. Then, the fluid temperature distribution $T_{\mathrm{a}}(x)$ can be expressed by the following equation:

$$T_{\mathrm{a}}(x) = \begin{cases} T_{\mathrm{m}} - [T_{\mathrm{m}}(0) - T_0]\,\dfrac{x}{L} & (0 \leq x \leq L), \\[2ex] T_0 & (L \leq x \leq nL). \end{cases} \tag{3.9}$$

The sensor-body temperature $T_{\mathrm{w}}(x)$ can be obtained by solving the differential equation (3.6) under the fluid temperature distribution given by Eq. (3.9). By normalizing the solution using T_{m} and T_0, the solution $\Theta(x)$ $[=(T_{\mathrm{w}} - T_0)/(T_{\mathrm{m}} - T_0)]$ can be written as

$$\Theta(x) = \begin{cases} C_1 \mathrm{e}^{x/L_{\mathrm{c}}} + C_2 \mathrm{e}^{-x/L_{\mathrm{c}}} + \left(1 - \dfrac{x}{L}\right) & (0 \leq x \leq L), \\[2ex] C_3 \mathrm{e}^{x/L_{\mathrm{c}}} + C_4 \mathrm{e}^{-x/L_{\mathrm{c}}} & (L \leq x \leq nL), \end{cases} \tag{3.10}$$

where $C_1 \sim C_4$ are constants of integration. To determine these constants, the following four boundary conditions are given to Eq. (3.10). (i) Adiabatic $(\mathrm{d}T_{\mathrm{w}}/\mathrm{d}x = 0)$ at $x=0$; (ii) The two solutions of Eq. (3.10) are equal at $x=L$; (iii) The conductive heat flowing through the cross section at $x=L$ is conserved (the temperature gradients $\mathrm{d}T_{\mathrm{w}}/\mathrm{d}x$ are equal at $x=L$); (iv) At $x=nL$, $T_{\mathrm{w}} = T_0$. Using the above four conditions, C_1, C_2, C_3 and C_4 can be determined as follows:

$$\begin{cases} C_1 = \dfrac{L_{\mathrm{c}}}{2L}\left[\dfrac{\mathrm{e}^{(n-1)L/L_{\mathrm{c}}} - \mathrm{e}^{-(n-1)L/L_{\mathrm{c}}} + 2\mathrm{e}^{-nL/L_{\mathrm{c}}}}{\mathrm{e}^{nL/L_{\mathrm{c}}} + \mathrm{e}^{-nL/L_{\mathrm{c}}}}\right], \\[2ex] C_2 = C_1 - \dfrac{L_{\mathrm{c}}}{L}, \\[2ex] C_3 = \dfrac{L_{\mathrm{c}}}{2L}\left[\dfrac{2 - \mathrm{e}^{L/L_{\mathrm{c}}} - \mathrm{e}^{-L/L_{\mathrm{c}}}}{\mathrm{e}^{2nL/L_{\mathrm{c}}} + 1}\right], \\[2ex] C_4 = -C_3 \mathrm{e}^{2nL/L_{\mathrm{c}}}. \end{cases} \tag{3.11}$$

Consequently, the non-dimensional temperature Θ_0 defined by Eq. (3.8) can be given by

$$\begin{aligned}
\Theta_0 &= C_1 + C_2 + 1 \\
&= \frac{L_\mathrm{c}}{L}\left[\frac{\mathrm{e}^{(n-1)L/L_\mathrm{c}} - \mathrm{e}^{-(n-1)L/L_\mathrm{c}} + 2\mathrm{e}^{-nL/L_\mathrm{c}}}{\mathrm{e}^{nL/L_\mathrm{c}} + \mathrm{e}^{-nL/L_\mathrm{c}}} - 1\right] + 1 \\
&= 1 + \frac{L_\mathrm{c}}{L}\left[\frac{\mathrm{e}^{(n-1)L/L_\mathrm{c}} - \mathrm{e}^{-(n-1)L/L_\mathrm{c}} - \mathrm{e}^{nL/L_\mathrm{c}} + \mathrm{e}^{-nL/L_\mathrm{c}}}{\mathrm{e}^{nL/L_\mathrm{c}} + \mathrm{e}^{-nL/L_\mathrm{c}}}\right] \\
&= 1 + \frac{L_\mathrm{c}}{L}\left[\frac{\sinh[(n-1)L/L_\mathrm{c}] - \sinh(nL/L_\mathrm{c})}{\cosh(nL/L_\mathrm{c})}\right] \\
&= 1 - \frac{\sinh(nL/L_\mathrm{c}) - \sinh[(n-1)L/L_\mathrm{c}]}{(L/L_\mathrm{c})\cosh(nL/L_\mathrm{c})}
\end{aligned} \tag{3.12}$$

It is noted that Eq. (3.12) approaches zero in the limit of $L/L_\mathrm{c} \to 0$.

3.1.4 Comparison of estimated heat-conduction error between the existing and proposed formulas

As mentioned above, the governing parameter of the heat-conduction error in fluid temperature measurement is the ratio of sensor length to cold length, L/L_c. Hence, we compare the behavior of the present estimation equation [Eq. (3.12)] with that of the existing formula [Eq. (3.7)] as a function of the parameter L/L_c. The result is shown in Fig. 3.4 and can be summarized as: 1) when a temperature sensor of $L/L_\mathrm{c} < 1$ is used, the temperature measurement becomes less than half the true value (the measurement error is more than 50%); 2) in the case of $L/L_\mathrm{c} > 1$, the existing formula [Eq. (3.7)] gives an error smaller than that estimated from the present equation [Eq. (3.12)]; and 3) parameter n hardly affects the behavior of Eq. (3.12) in the region of $L/L_\mathrm{c} > 3$.

In the above results, the item 2) must be very important. As an example, in order to make the heat-conduction error less than 10% (i.e., $\Theta_0 \geq 0.9$) in a thermal field with temperature gradient, Eq. (3.12) indicates the use of a sensor that satisfies $L/L_\mathrm{c} > 10$ as shown in Fig. 3.4. On the other hand, Eq. (3.7) provides the heat-conduction error less than 10% under the condition of $L/L_\mathrm{c} > 3$. Thus, it is highly dangerous to tolerate such a large difference in the estimation of the heat-conduction error in order to make a proper selection of temperature sensors. Hence, in fluid flows with temperature gradient, it is preferable to evaluate strictly the heat-conduction error using Eq. (3.12) to make a proper selection of sensors and/or correct appropriately the heat-conduction error in temperature measurements.

As for thin rod-shaped temperature sensors, we can estimate the heat transfer coefficient h in Eq. (3.3) using the following well-known correlation equations (3.13) and (3.14), which are called the Collis-Williams (Collis and Williams 1959) and Kramers (Kramers 1946) equations, respectively. The former is applicable to only airflow and the latter to air or water flow.

$$\mathrm{Nu}\left(\frac{T_\mathrm{f}}{T_\mathrm{a}}\right)^{-0.17} = A + B\mathrm{Re}^n, \tag{3.13}$$

$$\begin{cases} A = 0.24, B = 0.56, n = 0.45 & (0.02<\mathrm{Re}<44), \\ A = 0, B = 0.48, n = 0.51 & (44<\mathrm{Re}<140), \end{cases}$$

$$\mathrm{Nu} = 0.42\mathrm{Pr}^{0.2} + 0.57\mathrm{Pr}^{0.33}\mathrm{Re}^{0.50}, \tag{3.14}$$

where Nu $(= hd/\lambda_a)$, Re $(= Ud/\nu_\mathrm{a})$ and Pr $(= \nu_\mathrm{a}/(\lambda_\mathrm{a}/\rho_\mathrm{a}c_\mathrm{pa}))$ are the Nusselt, Reynolds and Prandtl numbers, respectively, and λ_a, ν_a, ρ_a and c_pa are the physical properties of

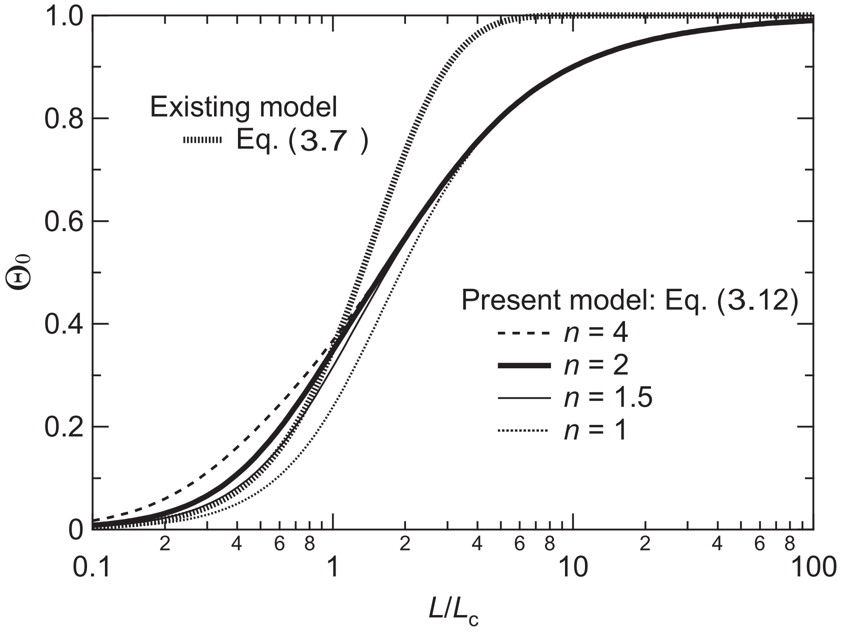

Figure 3.4 Comparison of heat-conduction error estimated between the conventional formula [Eq. (3.7)] and the proposed one [Eq. (3.12)].

the working fluid and denote, respectively, the thermal conductivity [W/(m·K)], kinematic viscosity [m^2/s], density [kg/m^3] and specific heat at constant pressure [J/(kg·K)]. In addition, T_f on the left-hand side of Eq. (3.13) is the film temperature defined by the arithmetic mean of sensor temperature T_w and fluid temperature T_a as $T_\mathrm{f} = (T_\mathrm{w}+T_\mathrm{a})/2$. At ordinary temperatures, we may use T_a instead of T_f.

3.2 Experimental apparatus and methods

3.2.1 Validation experiment using a wake flow formed behind a heated cylinder

In the present validation experiment, as shown in Fig. 3.5, we used a non-isothermal wake flow formed behind an electric heater (wattage: 300 W; total length: 300 mm) consisting of a stainless-steel cylinder 10 mm in diameter and is set at the middle of the long side of the rectangular exit (50 mm × 80 mm) of an upright wind tunnel. The working fluid is air. The Cartesian coordinate system (x, y, z) is employed, and the origin is set in the center of the heated cylinder. The x-axis is set in the flow direction and the z-axis along the axis of the heater. The y-axis is set normal to the x-z plane as shown in Fig. 3.5. The test section is the region of -30 mm$\leq y \leq 0$ mm at $x = 55$ mm and $z = 0$ mm.

In the following, we call a temperature sensor insusceptible to the heat-conduction error a ‘reference probe’ and a sensor subject to the heat-conduction error a ‘test probe’. Thus, we may evaluate quantitatively the heat-conduction error from mutual comparison between the temperature measurements by the test and reference probes. In the present experiment, as shown in Fig. 3.5, we set a type-K thermocouple 25 μm in diameter and 10 mm in length (distance between prongs) parallel to the z-axis so as not to generate a temperature gradient along the axis of the thermocouple wire, and used it as a reference probe. The 25 μm thermocouple is connected directly to the prongs consisting of thick type-K thermocouple wires 0.5 mm in diameter. On the other hand, the test probe consists of a type-K thermocouple wire (75, 125, 254 μm in diameter) which has an appearance like a pair of pine needles and is connected to the prong of thermocouple wires 0.5 mm in diameter to form an L-shaped structure. By setting the centerline of the pine-needle-shaped thermocouple in the y-direction, the temperature gradient is generated on the thermocouple-wire of the test probe.

We used three different test probes, which consist of the type-K thermocouple 75, 125 and 254 μm in diameter with protruding lengths—distance between the thermocouple bead and the prong—of 12, 15, 15 mm, respectively. Since the prong is much thicker than the thermocouple wires and its temperature can be considered to be kept at an ambient temperature, the interface between the sensor body and the support ($x = nL$) in the analytical model corresponds to the junction between the prong and the thermocouple wire. The protruding length of the 75 μm thermocouple is made shorter than those of the 125 and 254 μm thermocouples to prevent it from vibration. Although these thermocouple wires are slightly inclined with respect to the y-axis, the angle of inclination is 5 degrees at most and the difference between the temperature-gradient in the y-direction and that along the thermocouple-wire axis is less than 0.5%. Since the reference and test probes were mounted on the same precision motion stage, we were able to position these probes in the thermal fields to be measured within ±0.05 mm.

In the present experiment, the flow velocity in the x-direction and the flow temper-

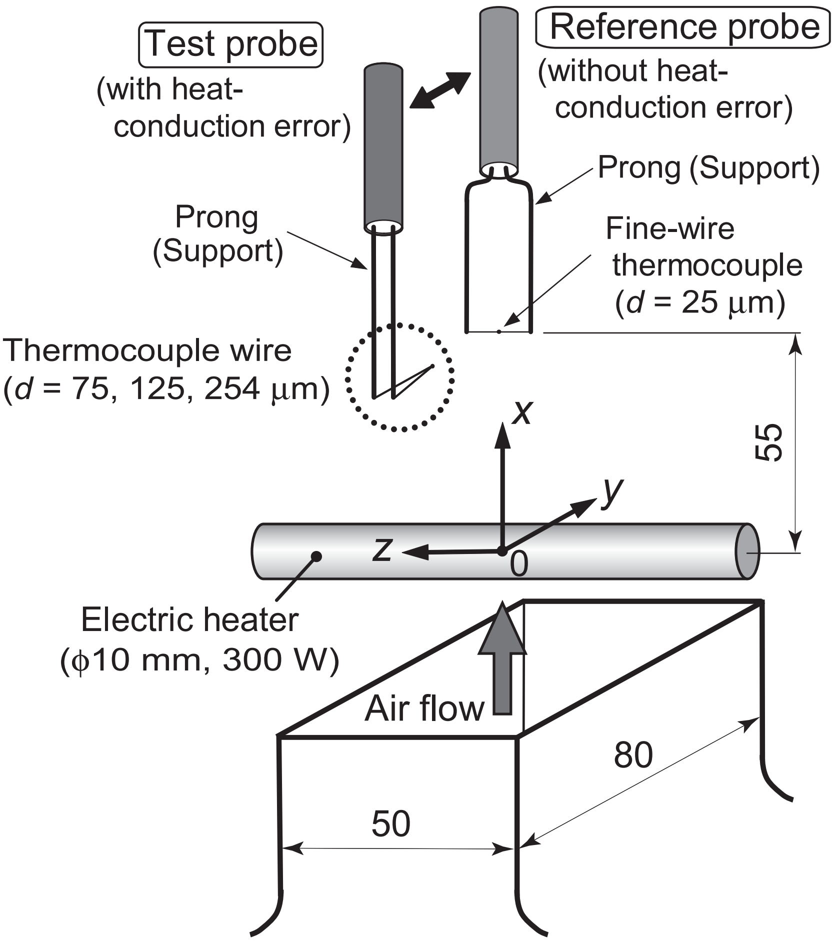
Test probe
(with heat-conduction error)
Reference probe
(without heat-conduction error)
Prong (Support)
Prong (Support)
Fine-wire thermocouple
(d = 25 μm)
Thermocouple wire
(d = 75, 125, 254 μm)
x
y
z
0
55
Electric heater
(ϕ10 mm, 300 W)
Air flow
80
50

Figure 3.5 Experimental apparatus and arrangement of reference and test probes for temperature measurement.

ature at the wind-tunnel exit were set to $U_0 = 4$ m/s and $T_0 = 300$ K, respectively. As shown in Fig. 3.6, since the flow field formed behind the cylinder (electric heater) is a turbulent wake flow, the thermal field also entails temperature fluctuation (Tagawa et al. 2001). As a test field, although it must be ideal for the temperature field not to fluctuate, the root-mean-square (r.m.s.) temperature fluctuations actually measured by the 75, 125 and 254 μm thermocouples were less than 2.0, 1.4 and 0.7 K, respectively (figures omitted). Hence, these values are sufficiently small compared with the variation in the mean temperature distribution (about 30 K), and have negligible effects on the experimental evaluation of the heat-conduction error. In addition, as seen in Fig. 3.6, although the mean velocity varies in the range of 3 $\sim$ 4 m/s in the test section, the relevant change in the heat-transfer coefficient h remains within 10% (5% for the cold-length L_c) so that the heat-transfer coefficient can be regarded as a constant value. For these reasons, the present experiment can be assumed to meet adequately the prerequisite for the theoretical analysis of the heat-conduction error.

The outputs of the temperature sensors were amplified by 1000 times using an instrumentation amplifier INA114 and were digitized by a 14-bit A/D converter (Microscience ADM-970PCI) at a sampling frequency of 1 kHz to collect 2^{17} (=131072) temperature data at each measurement position.

3.2.2 Verification experiment by candle flame

In the downstream region of a candle flame, there is formed a thermal field with very large temperature gradients. Therefore, this thermal field enables us to test critically the effectiveness of the estimation equation (3.12) for the heat-conduction error. The measurement system is shown in Fig. 3.7. The candle used has a diameter of 15 mm and was set in a box measuring 30 cm (W)$\times$ 40 cm (D) $\times$ 40 cm (H) to prevent the candle flame from being disturbed by the surrounding airflow. As shown in Fig. 3.7, the test section to be measured was 35 mm higher than the candlewick to be located just

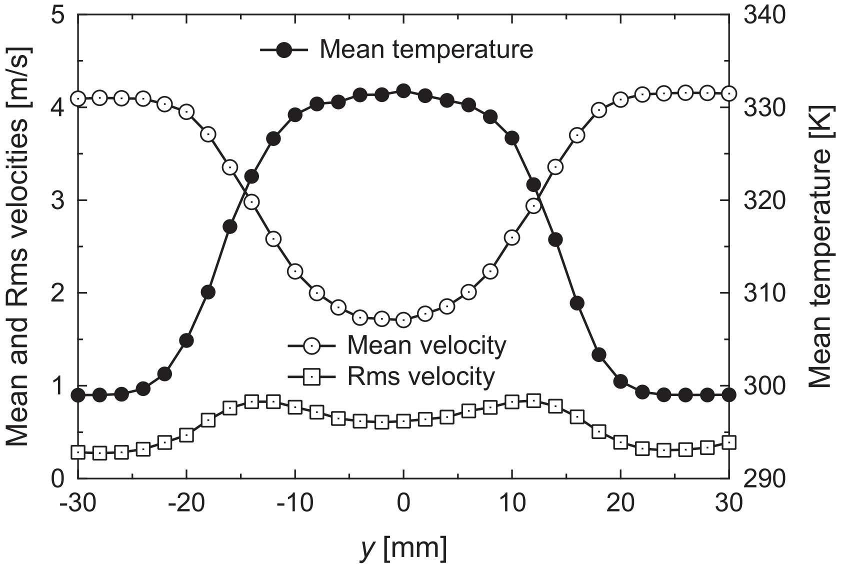

Figure 3.6 Characteristics of the test field for heat-conduction error. (Mean velocity and temperature distributions were measured by hot-wire anemometer and fine-wire thermocouple. Flow velocity was set to 4 m/s at a wind-tunnel exit.)

above the tip of the candle flame. The flow velocity around the flame was measured with a laser Doppler velocimeter (Kanomax, smart LDV system with retroreflector) by suspending alumina particles about 1 μm in diameter inside the box.

As the temperature sensors, we used the platinum-platinum rhodium thermocouple (type R: Pt-Pt$_{87}$Rh$_{13}$), which was welded to the prongs made of the same type-R thermocouple wires 0.5 mm in diameter. Unlike the heated wake flow shown in Fig. 3.5, the temperature field of the candle flame is formed concentrically. Thus, as a reference probe, we employed the type-R thermocouple 25 μm in diameter—which has a pine-needle shape 8 mm in length and is connected to the prongs—and set it vertically downward (in the negative direction of the x-axis) to minimize the temperature gradient

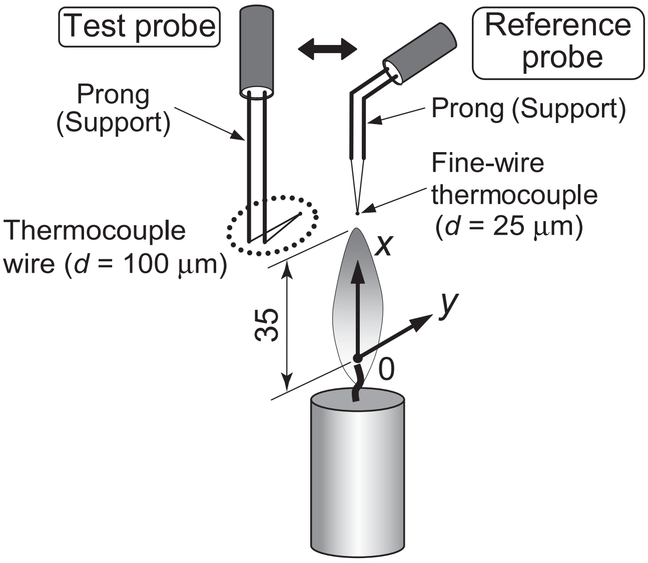
Test probe
Reference probe
Prong (Support)
Prong (Support)
Fine-wire thermocouple (d = 25 µm)
Thermocouple wire (d = 100 µm)
x
y
0
35

Figure 3.7 Experimental configuration for evaluating heat-conduction error in temperature measurement of candle flame.

along the thermocouple wires. On the other hand, the thermocouple wire used for the test probe was the type-R one 100 μm in diameter, protruding from the prongs at a right angle with its tip directed in the positive direction of the y-axis. As noted above, the interface between the sensor body and the support ($x = nL$) of the test probe can be regarded as the junction between the prong and the thermocouple wire. Both probes have an equal distance (2 mm) between the prongs.

3.3 Results and discussion

3.3.1 Measurement of temperature distributions

First, the temperature distributions measured in the y-direction of the heated wake flow (Fig. 3.5) are shown in Fig. 3.8. The ordinate indicates a difference between the measured temperature T_w and the surrounding one T_0, i.e., $(T_\mathrm{w} - T_0)$. The open circle in Fig. 3.8 indicates the result measured by the reference probe and can be regarded as the fluid temperature to be measured (true value). To verify the accuracy of the reference-probe measurements, we have replaced the 25 μm thermocouple of the reference probe by a 3.1 μm tungsten wire driven by a very low constant electric current (cold-wire) and then compared the two data. As a result, the temperature distributions measured by these two sensors were in very good agreement and hardly distinguishable (figure omitted). The thick solid line in Fig. 3.8 shows a straight-line approximation of the fluid-temperature distribution (open circles), and the intersection point of this line with the abscissa, i.e., $y = -25.5$ mm, corresponds to the position $x = L$ in Fig. 3.3.

As seen from Fig. 3.8, it is obvious that the temperature distribution falls with increasing thermocouple-wire diameter of the test probe. Namely, the heat-conduction error becomes pronounced in proportion to the cold length L_c of the sensor. It is noted, however, that the actual fluid temperature $T_\mathrm{a}(x)$ connects to the ambient temperature T_0 not discontinuously (as shown in Fig. 3.3) but smoothly as seen in Fig. 3.8. Thus, in the experimental evaluation of the heat conduction errors, we have excluded the vicinity

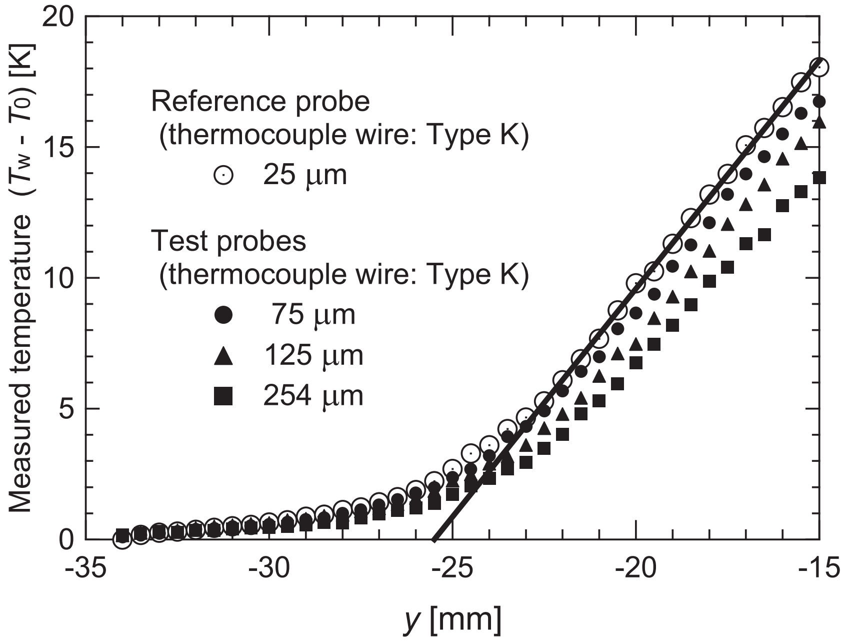

Figure 3.8 Temperature distributions obtained using the reference and test probes designed for wake flow formed behind a cylindrical heater.

of the intersection point at $y = -25.5$ mm and employed six measurement points given by $y = -20.5$, -19.5, -18.5, -17.5, -16.5 and -15.5 mm, at which the fluid temperature distribution measured by the reference probe is linearly increasing. Then, as seen from Fig. 3.3, the distance between the measurement position and intersection point can be regarded as L, and the above six measurements points correspond to $L = 5$, 6, 7, 8, 9 and 10 mm, respectively. As stated in section 3.2.1, since the protruding length of the test probe is 12 or 15 mm, the sensor support (prong) can be located outside of the linear fluid-temperature region, i.e., $y \leq -25.5$ mm even for the innermost measurement position of $y = -15.5$ mm.

On the other hand, the temperature distribution measurements of the candle flame

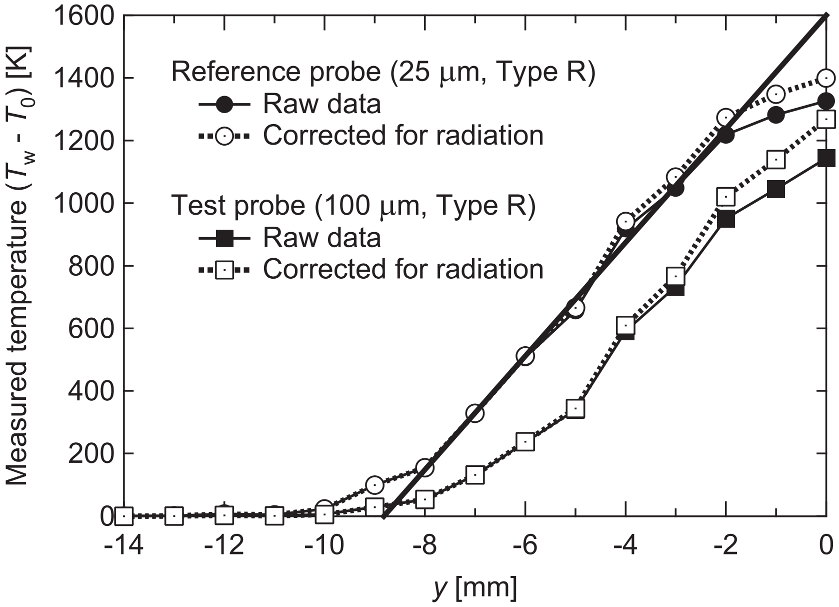

Figure 3.9 Temperature distributions obtained using the reference and test probes designed for candle-flame temperature.

(Fig. 3.7) are shown in Fig. 3.9. In the temperature measurement of combusting flows, we need to take account of the radiation effects on the measurements. Thus, we have corrected the measurements for the radiative heat loss in a manner similar to the previous study (Tagawa and Ohta 1997) on the assumption that the emissivity of the type-R thermocouple is 0.2 (Kaskan 1957, Bradley and Entwistle 1961). The results thus corrected are also included in Fig. 3.9. In addition, when we use a thermocouple consisting of platinum and platinum-rhodium alloy in combustion fields, we should be careful about the possibility that the measured temperature can indicate a value higher than the true temperature because of the catalytic effect of the platinum surface. In the present experiment, however, since the test section was located slightly above the candle flame, the combustion reaction is almost completed, and thus we may neglect the catalytic effect of the type-R thermocouple on the measurements.

As seen from Fig. 3.9, the temperature distributions measured by the reference probe show very steep temperature gradients, and the difference in gas temperature between the flame and the ambient air reaches 1400 K at $y = 0$ mm. Consequently, the outputs of the test probe consisting of the 100 μm type-R thermocouple indicate temperatures about 300 K lower than the actual fluid temperature due to the heat-conduction error. For the same reason mentioned above, we have evaluated the heat-conduction error based on the five measurement positions—$y = -4$, -3, -2, -1 and 0 mm—which are more than 5 mm away from the intersection of the straight line with the abscissa, i.e., $y = -9$ mm. Hence, the above five positions correspond to $L = 5$, 6, 7, 8 and 9 mm, respectively. Then, as explained in section 3.2.2, since the protruding length of the test probe is 12 mm, the sensor support (prong) is located outside of the linear-temperature region, i.e., $y \leq -9$ mm, even at the innermost measurement position of $y = 0$ mm.

3.3.2 Experimental evaluation of heat-conduction error and comparison with theoretical estimation

Based on the temperature distributions shown in Figs. 3.8 and 3.9, we have evaluated the heat-conduction errors experimentally. The results are collectively shown in

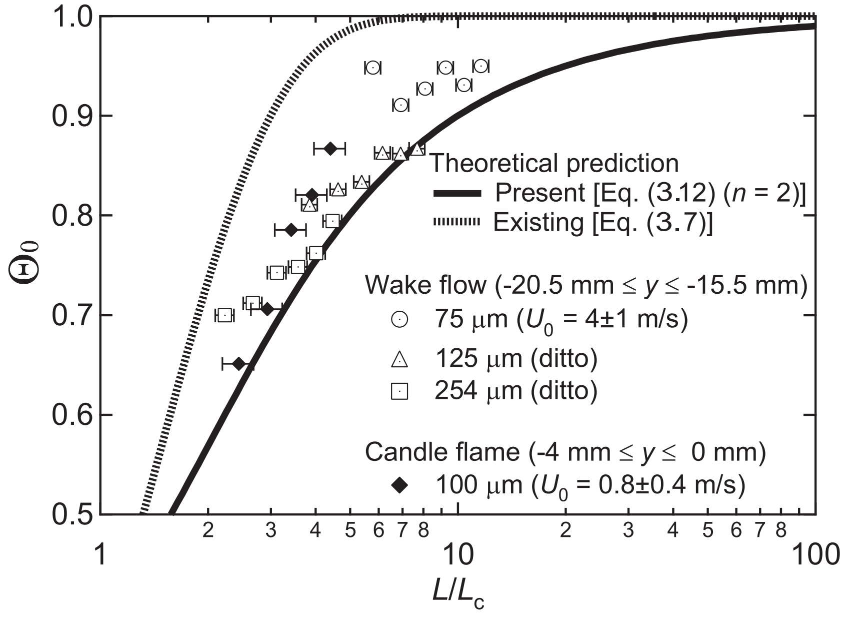

Figure 3.10 Experimental validation of the proposed theoretical formula [Eq. (3.12)] for estimating heat-conduction error based on the present experimental results.

Fig. 3.10. In addition, the results calculated by Eq. (3.7) and those by Eq. (3.12) are also included in Fig. 3.10. To estimate the heat-conduction error using Eq. (3.12), we need to give an appropriate value to the parameter n. As seen from Fig. 3.4, since the estimation by Eq. (3.12) is hardly affected by the value of n in the range of $L/L_c > 1$, we have employed $n = 2$ in the present study. The error bars attached to the experimental results indicate the change in the cold-length L_c by assuming that the variation in flow velocity ranges from 3 to 5 m/s for the wake flow and from 0.4 to 1.2 m/s for the candle flame. Namely, since the variation in flow velocity changes the cold length through the heat transfer coefficient, the value of L/L_c shown on the abscissa will vary even if L is unchanged.

As seen from Fig. 3.10, Eq. (3.12) can represent the behaviors of the experimental results quantitatively. In general, the heat-conduction errors obtained from the present experiments tend to be smaller than those predicted by Eq. (3.12). Such tendency may be ascribed to the shape of the experimental temperature distributions, which connects not discontinuously but gently to the ambient temperature T_0 as seen from Figs. 3.8 and 3.9. Especially for the wake flow formed behind the heated cylinder, from the behaviors the experimental results obtained by each thermocouple, it is observed that the difference in the heat-conduction error between the measured value and the theoretical estimation has a tendency to expand with decreasing L/L_c.

The above-mentioned effect may be reflected in such a tendency. As for the candle flame, as seen from Fig. 3.9, the fluid-temperature deviates from the linear distribution toward the center of the flame ($y = 0$ mm) to show a gentle profile. Thus, the difference between the measured and theoretical results indicates a tendency to expand with increasing L/L_c. Therefore, Eq. (3.12) can be considered as an error-estimation formula to provide the maximum value (upper limit) of the heat-conduction error. On the other hand, the existing formula, Eq. (3.7), gives error estimates fairly smaller than the experimental results. As stated in section 3.1.4, such a difference between Eqs. (3.7) and (3.12) should have a substantial influence on the criterion for selecting appropriate temperature sensors. As mentioned above, in non-isothermal fields with temperature gradients, since Eq. (3.12) can be considered to provide an upper limit of the heat-conduction error, it would be safer to select appropriate temperature sensors based on the error estimation by Eq. (3.12).

3.4 Heat-conduction error in temperature-fluctuation measurement

3.4.1 Physical model for theoretical analysis and frequency response of a temperature sensor with heat-conduction error

Based on the physical model shown in Fig. 3.11, we analyze theoretically the effects of the heat-conduction error on the measurements of temperature fluctuation. As shown in Fig. 3.11, the fluid temperature, $T_{\mathrm{a}}(t,x)$, is assumed to have a linear distribution anchored to the point of $x = L$ and fluctuates sinusoidally around the time-averaged (mean) temperature $\overline{T}_{\mathrm{a}}(x)$. Then, $T_{\mathrm{a}}(t,x)$ in the region of $0 \leq x \leq L$ can be represented using the fluid temperature to be measured, $T_{\mathrm{m}}(t)$, as:

$$T_{\mathrm{a}}(t,x) = \left(1 - \frac{x}{L}\right) T_{\mathrm{m}}(t) + \left(\frac{x}{L}\right) T_0. \tag{3.15}$$

To investigate the characteristics of sensor response to fluid-temperature fluctuations, we decompose $T_{\mathrm{a}}(t,x)$, $T_{\mathrm{m}}(t)$ and $T_{\mathrm{w}}(t,x)$ into mean and fluctuation components as follows:

$$\begin{cases} T_{\mathrm{a}}(t,x) = \overline{T}_{\mathrm{a}}(x) + t_{\mathrm{a}}(t,x), \\ T_{\mathrm{w}}(t,x) = \overline{T}_{\mathrm{w}}(x) + t_{\mathrm{w}}(t,x), \\ T_{\mathrm{m}}(t) = \overline{T}_{\mathrm{m}} + t_{\mathrm{m}}(t), \end{cases} \tag{3.16}$$

where the first and second terms on the right-hand side represent the time-averaged value and the fluctuation component, respectively. The substitution of Eq. (3.16) into Eq. (3.15) yields the following equation for $\overline{T}_{\mathrm{a}}(x)$ and $t_{\mathrm{a}}(t,x)$ of the fluid temperature $T_{\mathrm{a}}(t,x)$ for $0 \leq x \leq L$:

$$\begin{cases} \overline{T}_{\mathrm{a}}(x) = \left(1 - \dfrac{x}{L}\right) \overline{T}_{\mathrm{m}} + \left(\dfrac{x}{L}\right) T_0, \\ t_{\mathrm{a}}(t,x) = \left(1 - \dfrac{x}{L}\right) t_{\mathrm{m}}(t). \end{cases} \tag{3.17}$$

On the other hand, by substituting Eq. (3.16) into Eq. (3.2), we obtain the governing equation for temperature fluctuation of the sensor body, $t_{\mathrm{w}}(t,x)$, as follows:

$$\frac{\partial t_{\mathrm{w}}}{\partial t} = \frac{1}{\tau}(t_{\mathrm{a}} - t_{\mathrm{w}}) + a\frac{\partial^2 t_{\mathrm{w}}}{\partial x^2}. \tag{3.18}$$

Then, the insertion of the Fourier integrals for $t_{\mathrm{w}}(t,x)$ and $t_{\mathrm{a}}(t,x)$ (see the appendix) into Eq. (3.18) yields the differential equation representing the relation between the Fourier components $\hat{t}_{\mathrm{w}}(\omega)$ and $\hat{t}_{\mathrm{a}}(\omega,x)$, where ω denotes the angular frequency ($= 2\pi f$). By solving the governing equation in frequency space under the boundary conditions given in the 3.1.3, we obtain the frequency response function $H(\omega)$ of the temperature sensor illustrated in Fig. 3.11 (the derivation process is described in detail in the appendix).

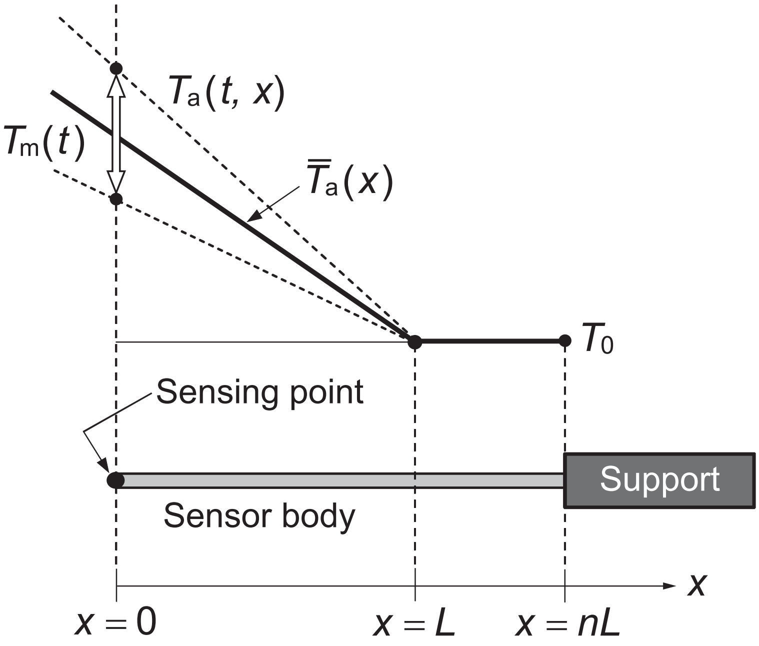

Figure 3.11 Theoretical model for analyzing the dynamic response of temperature sensor with heat-conduction error.

The solution is given by

$$H(\omega) = \frac{1}{1 + j\tau\omega}\left[1 - \frac{\sinh(n\Omega L/L_\mathrm{c}) - \sinh[(n-1)\Omega L/L_\mathrm{c}]}{(\Omega L/L_\mathrm{c})\cosh(n\Omega L/L_\mathrm{c})}\right], \tag{3.19}$$

where j is the imaginary unit and Ω denotes a variable parameter (complex number) defined by the following equation:

$$\begin{aligned} \Omega &\equiv \sqrt{1 + j\tau\omega} \qquad (3.20) \\ &= \frac{1}{\sqrt{2}}\left(\sqrt{\sqrt{1 + \tau^2\omega^2} + 1} + j\sqrt{\sqrt{1 + \tau^2\omega^2} - 1}\right) \end{aligned}$$

As seen from Eq. (3.19), $H(\omega)$ is written in the product of the first-order lag system and the same function as Eq. (3.12) in which the parameter L/L_c is replaced by $\Omega L/L_\mathrm{c}$.

On the other hand, as for the reference probe consisting of a fine-wire thermocouple shown in Fig. 3.5, the frequency response $H_0(\omega)$ was reported in the previous studies (Chomaik and Niedzialek 1967, Petit *et al.* 1982, Fralick and Forney 1993), which is given by

$$H_0(\omega) = \frac{1}{1 + j\tau\omega} \left\{ 1 - \frac{1}{\cosh[\Omega\ell/(2L_\mathrm{c})]} \right\}, \tag{3.21}$$

where ℓ is the prong span—the distance between the two prongs—of the reference probe. To be more specific, $H_0(\omega)$ can be obtained from Eq. (3.18) under the condition that the fluid temperature is uniform along the thermocouple wire and the wire temperature at both ends is anchored to a constant temperature, i.e., $T_\mathrm{w}(t, \pm\ell/2) = \overline{T}_\mathrm{m}$ with $t_\mathrm{w}(t, \pm\ell/2) = 0$. As for the present reference probe, the prong span ($\ell = 10$ mm; aspect ratio $\ell/d = 196$) is large enough to make Eq. (3.21) rather close to the first-order lag system.

Figure 3.12 shows the theoretical-analysis results of the frequency response Eq. (3.19) for $n = 2$, which are plotted along the abscissa of $\tau\omega$ $(= 2\pi\tau f)$ as a function of L/L_c. The response of the first-order lag system is included in Fig. 3.12 for comparison. In the first-order lag system, it is well known that the frequency giving $\tau\omega = 1$ is called the cutoff frequency f_c $[= 1/(2\pi\tau)]$ and the gain and phase have values of $1/\sqrt{2} = 0.707$ and $-\pi/4$ at f_c, respectively. As seen from Fig. 3.12, the effects of the heat conduction become pronounced in the low-frequency range, and $H(\omega)$ approaches the first-order lag system with increasing L/L_c. The gain of the flat part in the low-frequency range coincides with the value of Θ_0 in section 3.1.3. This is because $\Omega \to 1$ for $\tau\omega \to 0$ and

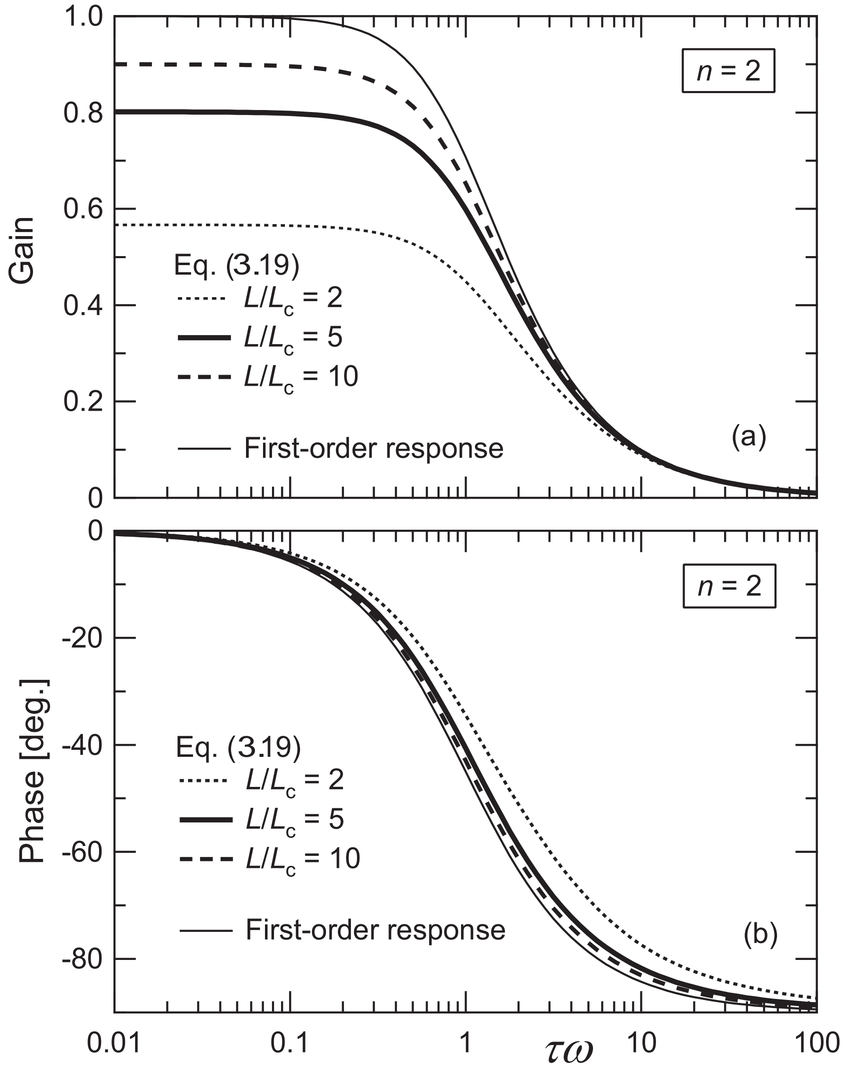

Figure 3.12 Frequency response of temperature sensor with heat-conduction error. (a) gain (b) phase

$H(\omega)$ approaches Θ_0 given by Eq. (3.12). It is noted that, as seen from Fig. 3.4, the frequency response $H(\omega)$ is almost independent of the value of n.

3.4.2 Influences of heat-conduction error on temperature-fluctuation measurement

To investigate experimentally the heat-conduction error in the temperature-fluctuation measurement, the temperature sensor needs to respond sufficiently fast to temperature fluctuations to be measured. In general, as the dynamic characteristics of the sensor deteriorates, the heat-conduction error will increase as shown in Fig. 3.4. For example, the increase in thermocouple-wire diameter will enlarge the time constant and slow the response speed of the thermocouple. Then, since the cold length $L_\mathrm{c} = \sqrt{a\tau}$ also increases, the ratio L/L_c becomes smaller even if L is kept constant. As a result, as shown in Fig. 3.10, the heat-conduction error increases with decreasing response speed of the thermocouple. However, the use of an excessive thicker thermocouple will make the signal-to-noise ratio too small to evaluate accurately the effects of the heat-conduction error on the temperature-fluctuation measurement. Therefore, in the present experiment, we have used a relatively thin type-K thermocouple 51 μm in diameter for the test probe with a protruding length 10 mm from the prong. In addition, the flow velocity at the wind-tunnel exit was set to a lower value of $U_0 = 1.5$ m/s not only to augment the intensity of temperature fluctuations but also to shift the power-spectrum distribution to the lower frequency range.

On the other hand, we used two different probes for the reference probe shown in Fig. 3.5: one is a cold-wire probe consisting of a fine tungsten-wire 3.1 μm in diameter

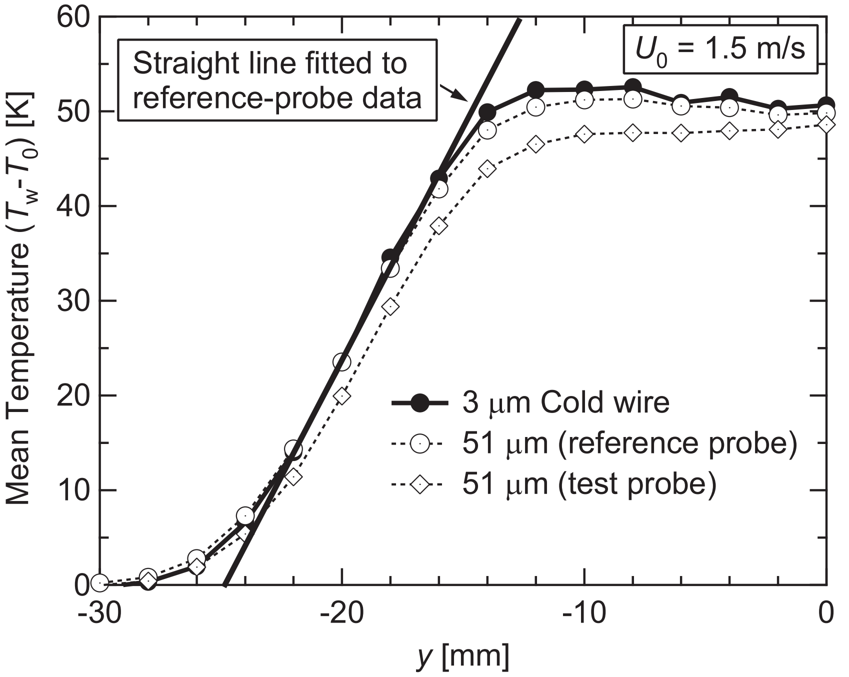

Figure 3.13 Mean temperature distribution of a wake flow formed behind a heated cylinder.

and 1.5 mm in length with a prong span of 4 mm; and the other is a thermocouple probe having the type-K thermocouple 51 μm in diameter with a prong span of 16 mm.

Figure 3.13 shows the measurement results of the mean-temperature distributions. As seen from Fig. 3.13, the onset of the heat-conduction error is clearly observed in the test-probe measurements, although it is not so significant as in Figs. 3.8 and 3.9. From the straight-line approximation to the temperature distributions measured by the reference probes, the intersection of the straight line with the abscissa is found to locate at $y = -25$ mm.

Figure 3.14 shows the root-mean-square (r.m.s.) values of the temperature fluctu-

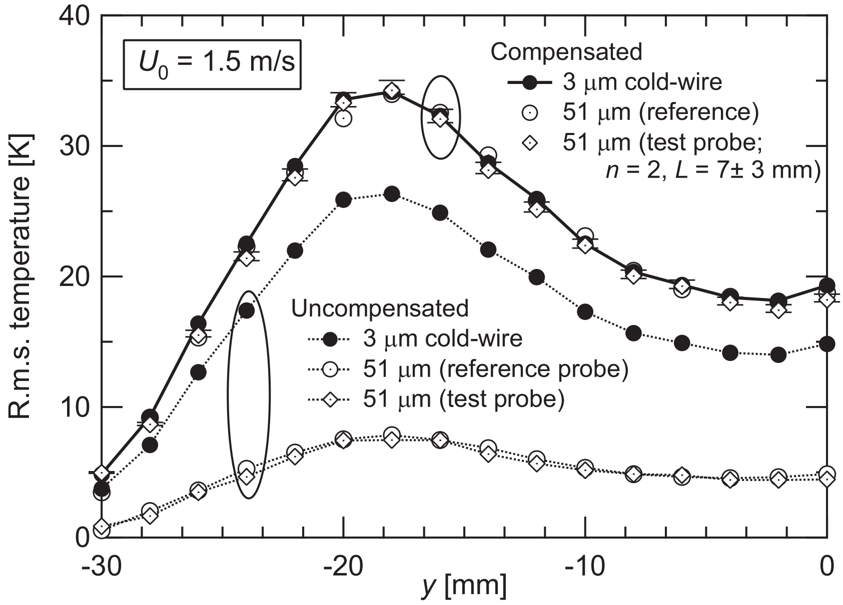

Figure 3.14 Response compensation of temperature fluctuations measured by the reference and test probes.

ations measured by the two reference probes and the test probe. In Fig. 3.14, the raw (uncompensated) outputs of these three temperature sensors and the results compensated for the response delay of the sensor are shown simultaneously.

For the response compensation of the cold-wire and fine-wire thermocouple of the reference probes, we used a frequency-response function of the cold-wire reported previously (Tagawa et al. 2005) and Eq. (3.21) which is, as mentioned above, almost equal to the first-order lag system, respectively. The compensation procedure based on the frequency response function is explained in detail in our previous paper (Tagawa *et al.* 2005). The outline is as follows: 1) apply the fast-Fourier-transform (FFT) to the sensor output (time-series data); 2) multiply the FFT output by the inverse of the

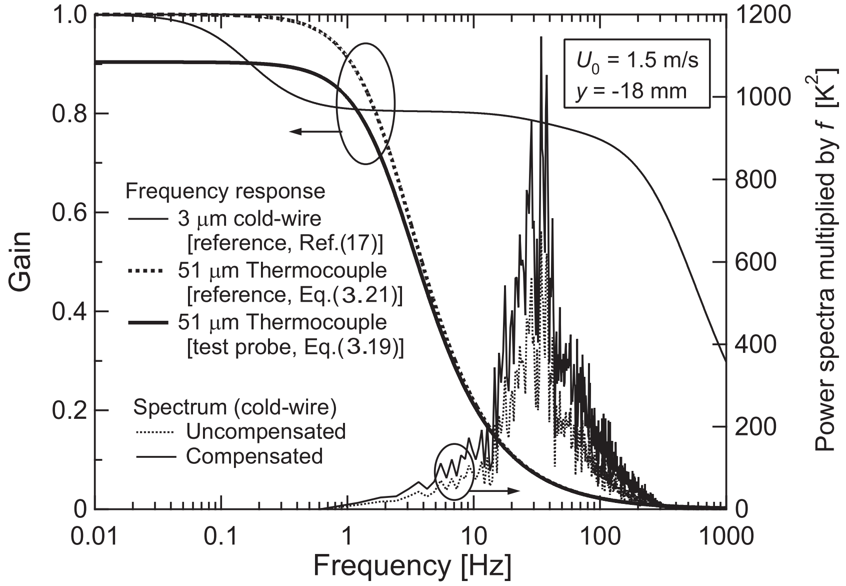

Figure 3.15 Frequency responses of the reference and test probes, and power spectra of raw and compensated data measured by the reference cold-wire probe (Tagawa et al. 2005).

response function, i.e., $H^{-1}(\omega)$, and 3) apply the inverse FFT to the frequency-domain data thus obtained. On the other hand, the thermocouple output of the test probe was compensated using Eq. (3.19). In the application of Eq. (3.19), since the parameter L is dependent on the measurement position, we have varied L within the range of $L = 7 \pm 3$ mm and demonstrated the effects of the value of L on the compensated results.

As seen from Fig. 3.14, there appears to be little difference in the compensated result among these three probes. Namely, we can reproduce accurately the fluid-temperature fluctuations using Eq. (3.19) irrespective of the existence of the heat-conduction error. Interestingly, in the present test field, the heat-conduction error hardly affects the raw (uncompensated) measurements of the two thermocouple outputs of the reference and test probes. Such phenomena can be explained as follows.

Figure 3.15 shows the frequency response (gain) of the three temperature probes together with the uncompensated (raw) and compensated power spectra measured by the 3.1 μm cold-wire of the reference probe at $y = -18$ mm. The abscissa is frequency f [Hz]. In Fig. 3.15, the power spectrum $E(f)$ is shown in the form of $f \cdot E(f)$, which is called the pre-multiplied spectrum in the field of turbulence research. Such expression of the power spectrum is useful to indicate the contribution of each frequency component to the variance of temperature fluctuation $\overline{t^2}$ when the frequency scale is logarithmic, since the following relation holds:

$$\begin{aligned} \overline{t^2} &= \int_0^\infty E(f)\,\mathrm{d}f = \int_0^\infty f \cdot E(f) \frac{\mathrm{d}f}{f} \\ &= \int_0^\infty f \cdot E(f)\,\mathrm{d}(\ln f). \end{aligned} \tag{3.22}$$

As seen from the profile of the pre-multiplied spectrum, the central frequency of the present fluctuating temperature field is located in the range of 30 $\sim$ 40 Hz and the contribution of the frequency components lower than a few hertz should be quite small. Thus, even if we use the temperature probe entailing the heat-conduction error like the test probe, the heat-conduction error has little effect on the sensor output. Namely, the heat-conduction error in the temperature-fluctuation measurement depends strongly on the frequency characteristics of an unsteady temperature field to be measured. Consequently, as seen in Fig. 3.15, if the power spectrum distribution stays sufficiently away from the low-frequency region where the heat-conduction error has a significant influence, we need not take into account the heat-conduction error to compensate for the response delay of the temperature sensor.

Chapter 4

A coordinated velocity and temperature sensor for flow-direction and flow-velocity measurement

A coordinated hot-wire and thermocouple sensor has been developed to measure simultaneously flow-direction and flow-velocity. The sensor is designed to suit a wide range of outdoor measurement. The CCA technique described in Chapter 2 has been employed not only to measure flow velocity but also to work as a heat source for the twelve fine-wire thermocouples, which surrounds the hot-wire equiangularly on the circumference of circle, to detect the convected hot region due to the heat source.

4.1 Frequency response of flow-direction and flow-velocity sensor

In this section, we have investigated the frequency responses of the flow-direction sensor composed of the thermocouples and the flow-velocity sensor driven at the constant-current mode (CCA). First, the frequency responses (gain) of the thermocouple probe 51 μm in diameter are shown in Fig. 4.1. In Fig. 4.1 (a), the frequency response of the thermocouple probe (51 μm in diameter) with a prong span of $\ell = 16$ mm, which can be regarded as a reference probe as shown in Fig. 3.5, has been calculated using Eq. (3.21). In Fig. 4.1 (b), on the other hand, the response of the thermocouple probe (51 μm in diameter) with the sensing length of $L = 8$ mm, which was used as the test probe shown in Fig. 3.5, has been obtained using Eq. (3.19). As seen from these figures, naturally, the cutoff frequency decreases with decreasing flow velocity regardless of the type of thermocouple probe. As for the thermocouple probe with a sensing length of $L = 8$ mm, it should be remarkable that the gain in the low-frequency region becomes deteriorated due to the effect of the heat-conduction error and pronounced with decreasing flow velocity. As shown in Fig. 3.15, we may say that the effect of heat-conduction error on the thermocouple output can be estimated to be less than 10% on condition that the flow velocity is higher than 1.5 m/s.

Figure 4.2 shows the frequency-response characteristics of the CCA reference sensor and the test sensor obtained by Eq. (2.8). The results are shown as a function of flow

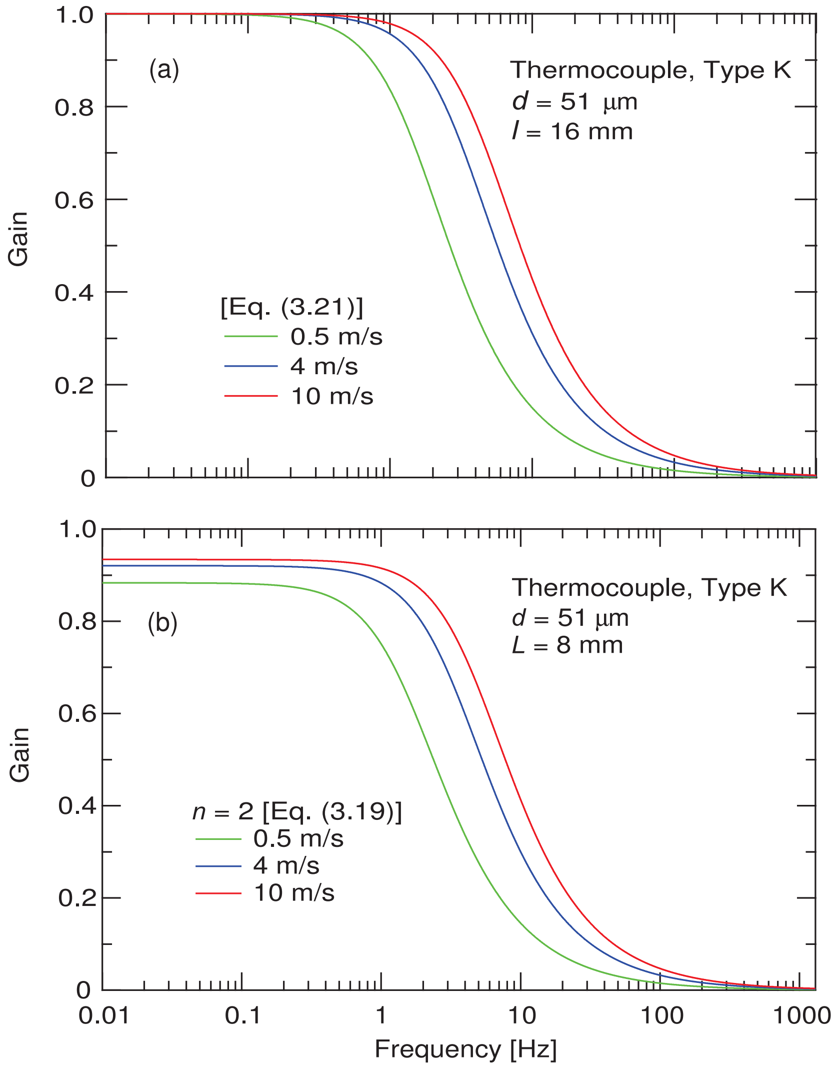

Figure 4.1 Frequency response of temperature sensors as a function of flow velocity: (a) Standard fine-wire thermocouple probe 51 μm in diameter with the prong span of $\ell = 16$ mm [Eq. (3.21)]; (b) V-shaped thermocouple probe 51 μm in diameter with the sensing length of $L = 8$ mm [Eq. (3.19)].

velocity. In Fig. 4.2 (a), the CCA reference probe consists of a tungsten wire 10 μm in diameter, whose physical properties are shown in Table 2.1. On the other hand, Fig. 4.2 (b) shows the CCA test sensor consisting of a minute coil of a nichrome wire

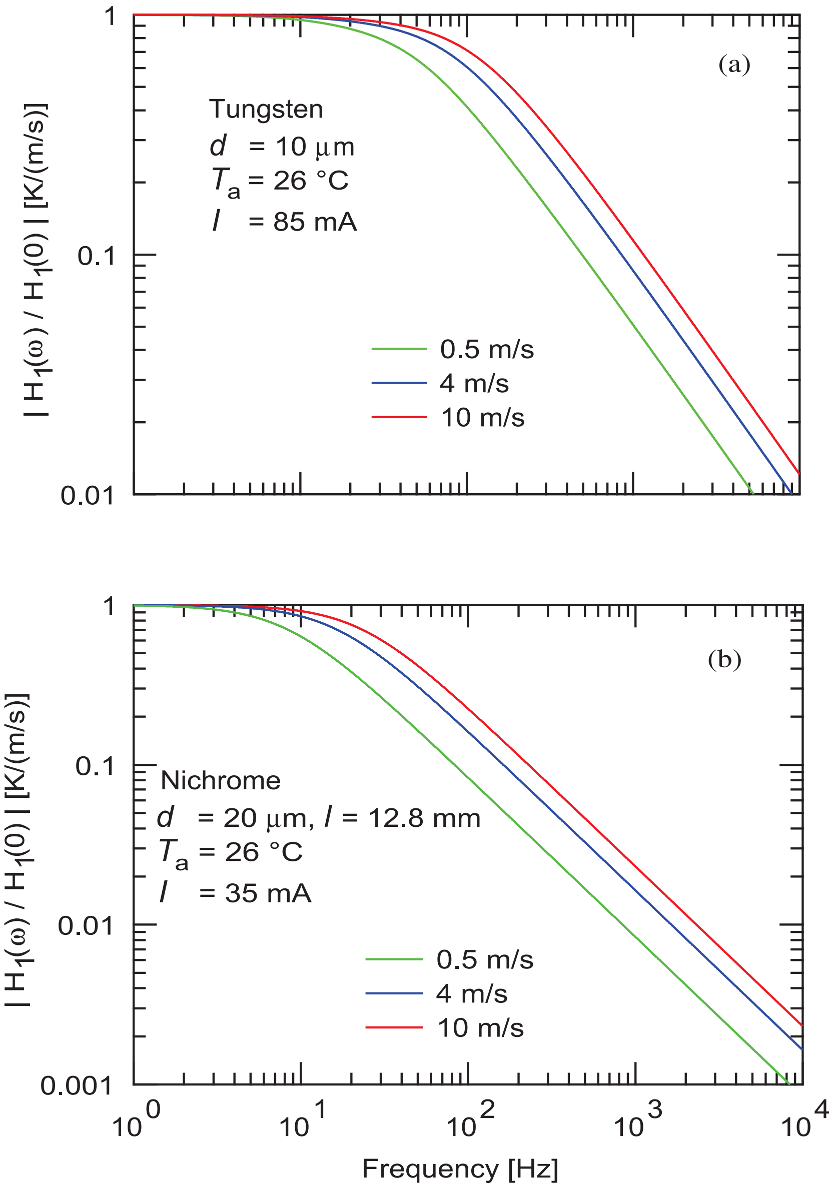

Figure 4.2 Frequency response of CCA reference sensor and test sensor as a function of flow velocity using Eq. (2.8): (a) Reference sensor (tungsten wire 10 μm in diameter); (b) Test sensor (nichrome coil 20 μm in diameter).

20 μm in diameter. The nichrome coil is soldered directly to the prong tips of steel without providing any stub parts. The frequency responses of these two sensors are

calculated for three flow velocities in consideration of outdoor measurement. As seen from the figures, if the flow velocity is reduced to 0.5 m/s, the cutoff frequency in the response of the CCA test sensor (nichrome coil) drops to less than 10 Hz, while that of the reference sensor (tungsten wire) is still higher than 20 Hz.

4.2 Sensor arrangement and experimental setup

4.2.1 Sensor arrangement

The flow-direction sensor consists of the constant-current hot-wire anemometer (CCA) made of the minute coil of a nichrome wire 20 μm in diameter [nickel (77%), chromium (19 $\sim$ 21%) and others 2 $\sim$ 4%] and the twelve type-K thermocouples (d = 51 μm), which are arranged equiangularly around the CCA sensor [see in Fig. 4.3 (a)]. The diameter of the nichrome-coil of the CCA sensor is about 0.5 mm. The CCA sensor is designed not only for sensing airflow velocity but also for serving as the heat source for the thermocouples to detect the flow-direction. The flow-direction sensor is mounted on a plastic disk 18 mm in diameter, which is attached to the end of a cantilever in consideration of not only handleability but flexibility in the probe design. The heated coil generates a thermal boundary layer in the downstream region and will be detected by the thermocouples surrounding the coil (0 to 360°). In the present study, we have used another hot-wire probe consisting of a tungsten wire 10 μm in diameter as the reference velocity sensor to verify the reliability of the nichrome-coil measurements. These two hot-wire sensors are driven at the constant-current mode. The driving currents for the nichrome coil (test probe) and the tungsten wire (reference one) were set at 35 mA and 85 mA, respectively. The driving current for the nichrome coil needs to be sufficient to provide a high-temperature region for the surrounding thermocouples. Specifically, it will raise the airflow temperature up to 40° when the flow velocity is less than 1 m/s.

The twelve type-K thermocouple wires 51 μm in diameter are used for detecting a hot wake formed downstream of the nichrome coil to sense the flow direction. These wires are attached to the prongs consisting of the type-K thermocouple wire (30 AWG; Omega), the prongs are fixed to the plastic disc. As seen in Fig. 4.3 (b), these twelve thermocouples, which are V-shaped [(Minn Khine *et al.* 2013 (a) (b)], are arranged circumferentially at every 30°. The hot junctions of these thermocouples are 15 mm away from the disc surface to avoid fluid-dynamical interferences with the supporting section of the sensors. The edge of the disc is also tapered to 15° so as to accept a larger angle of attack of the airflow.

The above nichrome coil and thermocouples have been constructed separately. First, the plastic disk is fastened on to the end of the steel pipe (outside diameter 6 mm and inner diameter 4 mm) using the epoxy adhesive. Then, the thermocouple prongs are installed on this disk. The nichrome coil is attached to the steel prongs 0.5 mm in diameter which are set inside the inner steel pipe (outside diameter of 4 mm). In such a way, the nichrome coil is located in the geometrical center of the twelve thermocouples. The position of the coil can be fine-tuned using the adjusting screws to bring the coil as close to the geometrical center as possible.

4.2.2 Experimental setup

Prior to the verification experiment for the flow-direction sensor, we have examined the location of the outdoor measurement and found an appropriate sites (for steady- and complex-flow cases) in the campus of Nagoya Institute of Technology (NIT) (see Fig. 4.4). The experimental setup used is shown in Fig. 4.5. This photograph shows the measurement near the building No.12 in the NIT campus where we can get both relatively steady- and complex wind cases. As shown in Fig. 4.5, we have used the flow-direction sensor shown in Fig. 4.3 (a), in which the CCA reference sensor and the two reference thermocouples are installed to know ambient airflow velocity and temperature accurately. The reference and test CCA probes are calibrated by a small wind tunnel designed exclusively, which can provide airflow velocities ranging from 0 to 9 m/s by using a voltage slider for controlling the output voltage 0 to 130 V. To exclude disturbance in the airflow during the calibration experiment, the sensing part are shielded from the ambient flow field. The sampling frequency and sampling number are set at 100 Hz and 35000, respectively. All the analog output signals are digitized by 16-channel analog-to-digital converter, and the measurement data are stored in a personal computer.

4.3 Results and discussion

4.3.1 Indoor flow-direction measurement

In the present experiment, we have tested the performance and measurement accuracy of the developed flow-direction sensor in indoor experiment by using a specifically-constructed horizontal wind tunnel. The flow-direction sensor is firmly attached on the basement of a rotatable precision stage (Chuo Precision Industrial Co., Ltd.). In this measurement, the precision stage is rotated at every 15° by a stepping motor to find the spatial resolution of the present flow-direction sensor. The airflow velocity is set at 5 m/s. It is noted that the wind tunnel used can provide a uniform airflow for the calibration of the sensor, and the airflow velocity ranges from 0 to 9 m/s, which is necessary for outdoor measurement. When the airflow pass through the flow-direction sensor, only the downstream thermocouples will detect the high-temperature wake region due to heat convection by airflow, while the other thermocouples continue to sense the ambient airflow temperature. Thus, the angular resolution of the flow-direction sensor will depend principally on the arrangement of the thermocouples surrounding the nichrome coil. To improve the angular resolution of the flow-direction sensor, we have applied the well-known Gaussian interpolation method (Markus *et al.* 1998) to the three consecutive thermocouple outputs around the highest temperature measurement. As shown in Fig. 4.6, the Gaussian interpolation method uses the three highest measurements to estimate a true peak location. The Gaussian curve fitting is reason-able, since the temperature signals detected by the twelve thermocouples are almost always distributed according to the Gaussian distribution. As shown in the figure, a, b and c are the three highest intensities (one is the maximum and the other two are the intensities next to the maximum), and their locations—i.e., identification numbers for the thermocouples—are expressed as $x-1$, x and $x+1$ with b having the highest value. Then, the estimated peak location (P) is given by

$$P = x - \frac{1}{2}\left[\frac{\ln(c)-\ln(a)}{\ln(a)-2\ln(b)+\ln(c)}\right], \tag{4.1}$$

where x is the coordinate for the thermocouple location corresponding to the angle of arrangement, and b is the maximum value among the twelve thermocouple outputs. In the present study, $x{-}1$, x and $x{+}1$ are the locations of the values a, b and c, respectively, and are the three consecutive integers ranging from 1 to 12. The sample measurement result is shown in Fig. 4.7. As seen from the figure, the Gaussian interpolation method can work correctly and the estimated angles—flow-directions—agree well with the stage angles set for the calibration. Although there exist fluctuations in the estimated flow angles as shown in Fig. 4.8, the fluctuation intensities (r.m.s. values) of the flow angles are less than 0.5 degree (mostly less than 0.3 degree) and are negligibly small in actual measurement situations. Thus, the present flow-direction sensor can be used as a reliable tool in outdoor measurement.

4.3.2 Outdoor flow-direction and flow-velocity measurement

As shown in Fig. 4.5, the flow-direction sensor (wind sensor) is firmly mounted using stationary clamps on a small table. As seen from Fig. 4.9, the twelve type-K thermocouples 51 μm in diameter are arranged equiangularly at every 30°, and the data channels for the thermocouple outputs are numbered clockwise. The channel No. 12 represents 0° and/or 360° and can also be regarded as the channel No. 0 in the digital signal processing. In the present experiment, the channel No. 12 is set to the north direction. The flow-direction can be obtained from the twelve thermocouple outputs using Eq. (4.1). First, at a certain moment, the maximum temperature is identified from the twelve ones. Secondly, the two temperatures of either side of the maximum are selected and named as a and c as shown in Fig. 4.6. Finally, the Gaussian fitting process is applied to these three temperature data. The arrangement of the twelve thermocouples and their directions are shown in Fig. 4.9 (a), and the flow velocity measured by the CCA sensor can be decomposed into two velocity components, u and v, using the velocity-direction data obtained [Fig. 4.9 (b)]. In Fig. 4.9 (b), the vertical and horizontal axes represent the north and east directions, respectively.

The flow velocity can be measured by the CCA sensor (nichrome coil) installed in the present flow-direction sensor. As usual, the static calibration experiment is conducted using a pitot tube. The hot-wire driven at the constant-current (CC) mode is generally sensitive to a change in the ambient temperature (T_{a}). Thus, the change in the ambient temperature is monitored during the outdoor measurement. It sometimes changed rapidly in the range of $1 \sim 2$°C when the flow velocity became lower than 1 m/s or higher than 4 m/s.

Steady wind conditions

In this section, the results of the simultaneous flow-direction and flow-velocity measurement conducted in steady wind conditions are discussed. The flow velocities measured by the CCA reference and test sensors are shown in Fig. 4.10. As seen from these figures, in the present experiment, there is little practical difference between the two CCA sensor outputs, and the response compensation has little effect on their measurements. This result indicates that there exists no high-frequency velocity component in the present wind conditions, and the slight difference between the two sensor outputs can be ascribed to the difference in the measurement position between the two sensors. The present results demonstrate that the CCA sensor (nichrome coil) installed in the flow-direction sensor can be used as not only a heat source for the flow-direction detection but also a velocity sensor without using the reference sensor.

The comparison between the uncompensated (raw) and compensated outputs of the twelve thermocouples is shown in Fig. 4.11. As seen from the figure, in the present steady wind conditions, the four thermocouples named No. 1, 2, 3 and 4 are almost always located downstream of the hot wake due to the thermal convection from the heated nichrome coil. Consequently, the sensor of No. 2 or 3 must be located in the center of the hot wake and shows the temperature exceeding 25°C, while the output signals of the upstream one (the opposite position: No. 8 or 9) are kept at the ambient airflow temperature.

Figure 4.12 shows the sample results of the flow-direction measurement conducted near Building No.12 in steady wind conditions. The detected flow-direction is represented by the channel numbers of the twelve thermocouples. As shown in Fig. 4.13, the direction can be converted to the angle to the north direction (0 or 360 degree) using Figure 4.9. As seen from the figure, the measured flow-direction fluctuates in a narrow range of 30° to 120° (the thermocouples detecting the hot wake are limited to No. 1, 2, 3 and 4) because of the steady wind conditions. The two velocity components obtained from the flow-direction results together with the velocities measured by the CCA sensor (nichrome coil) are shown in Fig. 4.14. As seen from the figure, the two velocity components are almost always kept separated from each other due to the steady wind conditions.

Complex wind conditions

In outside measurement, it is not uncommon that not only the flow-velocity but also the flow-direction are changing rapidly. In the following, the sample results of the flow-direction and flow-velocity measurement in complex wind conditions are discussed.

The flow-velocity measurements by the CCA sensor (nichrome coil) are compared with those by the reference sensor, and the results are shown in Fig. 4.15. As seen from the figure, the measurements by the CCA sensor are hardly damped compared with those by the reference sensor as expected from the results of the steady wind case. However, there exist some discrepancies between the two instantaneous signal traces due to the spatial difference in measurement position and/or fluid-dynamical interferences between the two CCA sensors. It is noted that the flow velocities measured by the two CCA sensors show appreciable discrepancies in the range of 6 to 10 second as seen from Fig. 4.15. This is apparently because the flow-direction changed rapidly and widely (see Fig. 4.17). As discussed in the preceding section 4.1, although the frequency response of the CCA sensor (nichrome coil) deteriorates as decreasing flow velocity—for example, at flow velocity 0.5 m/s appearing around 6 second, the twelve thermocouple outputs shown in Fig. 4.17 can detect correctly the rapid changes in the flow direction. As shown in the lower figure of Fig. 4.15, both the CCA sensors are compensated using Eq. (2.8) with the aid of the adaptive response compensation technique. However, the compensated CCA test sensor (nichrome coil) could not sufficiently follow the reference sensor, since the intrinsic response speed of the nichrome coil may be too slow for its outputs to be in excellent agreement with those of the reference sensor.

Figure 4.16 shows the comparison of signal traces between the uncompensated (raw) and compensated temperatures measured in the complex wind conditions. The compensated data is obtained using Eq. (3.19) to know the effects of heat-conduction on the measurements. Although the effects of heat-conduction will become apparent as decreasing flow velocities [see Fig. 4.1 (b)], the compensated results must be satisfactory as shown in Fig. 4.16.

Figure 4.17 shows the flow-direction measurements obtained under the unsteady wind conditions, in which the flow-direction is represented using the channel numbers of the twelve thermocouples. This data can be converted into the angle to the north direction, and the result is shown in Fig. 4.18. The flow velocity can be decomposed into the two velocity components, u and v, using the CCA outputs together with the flow-direction measurements as shown in Fig. 4.19. From these figures, it is clear that the flow-velocity and flow-direction are changing rapidly in the range of 6 to 10 second, since the fairly violent wind passed through the measurement site (near the building No. 12) where a complex flow-field can sometimes be formed because of the canyon of buildings. Consequently, as shown in Fig. 4.19, the velocity component v sometimes becomes close to 0 m/s.

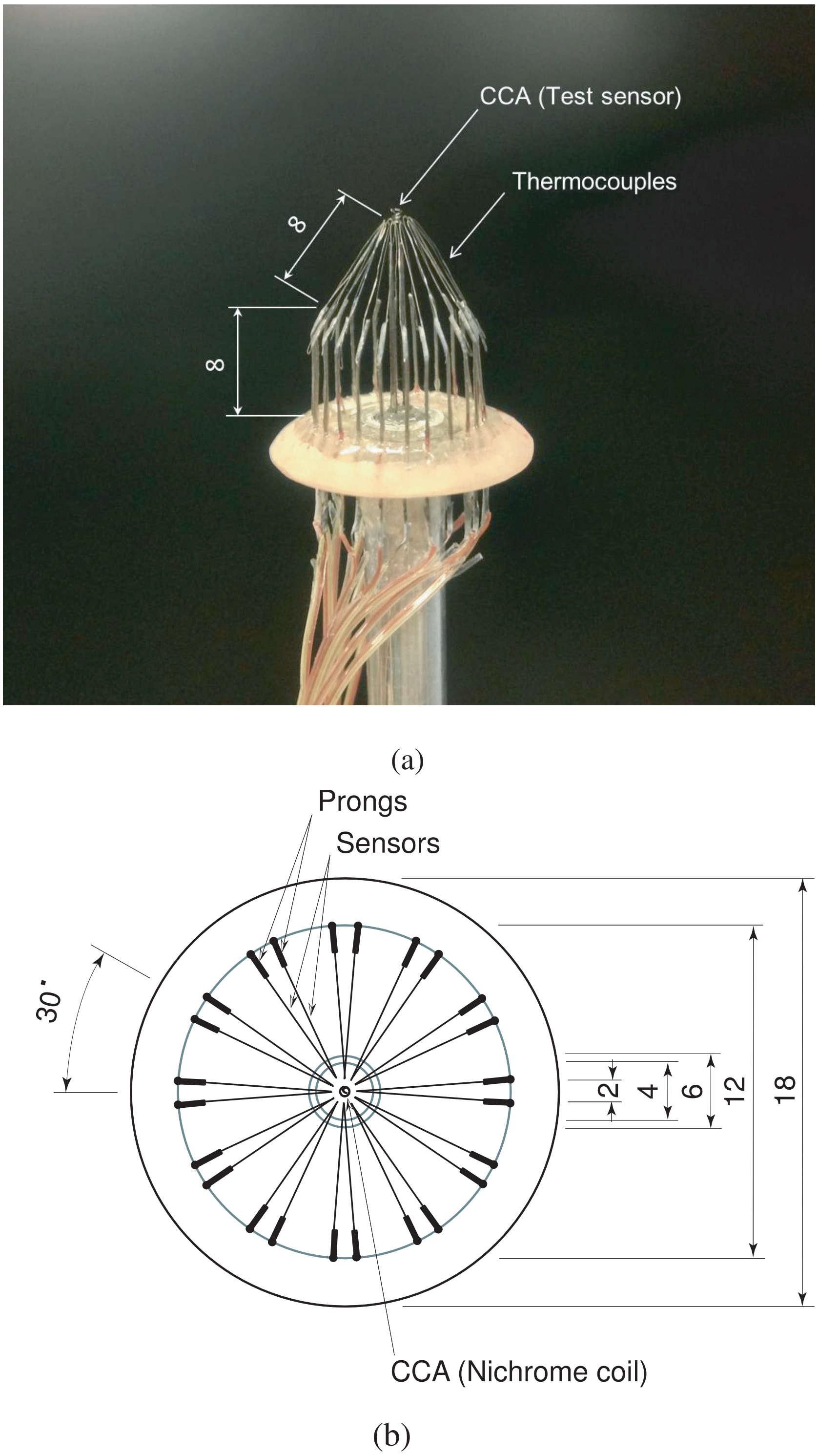
CCA (Test sensor)
Thermocouples
8
8
(a)
Prongs
Sensors
30˚
2
4
6
12
18
CCA (Nichrome coil)
(b)

Figure 4.3 Flow direction sensor combined with the CCA and twelve K-type thermocouples: (a) Photograph of the sensor from the front view; (b) Plan view of the fabricated sensor. (All dimensions in millimeters.)

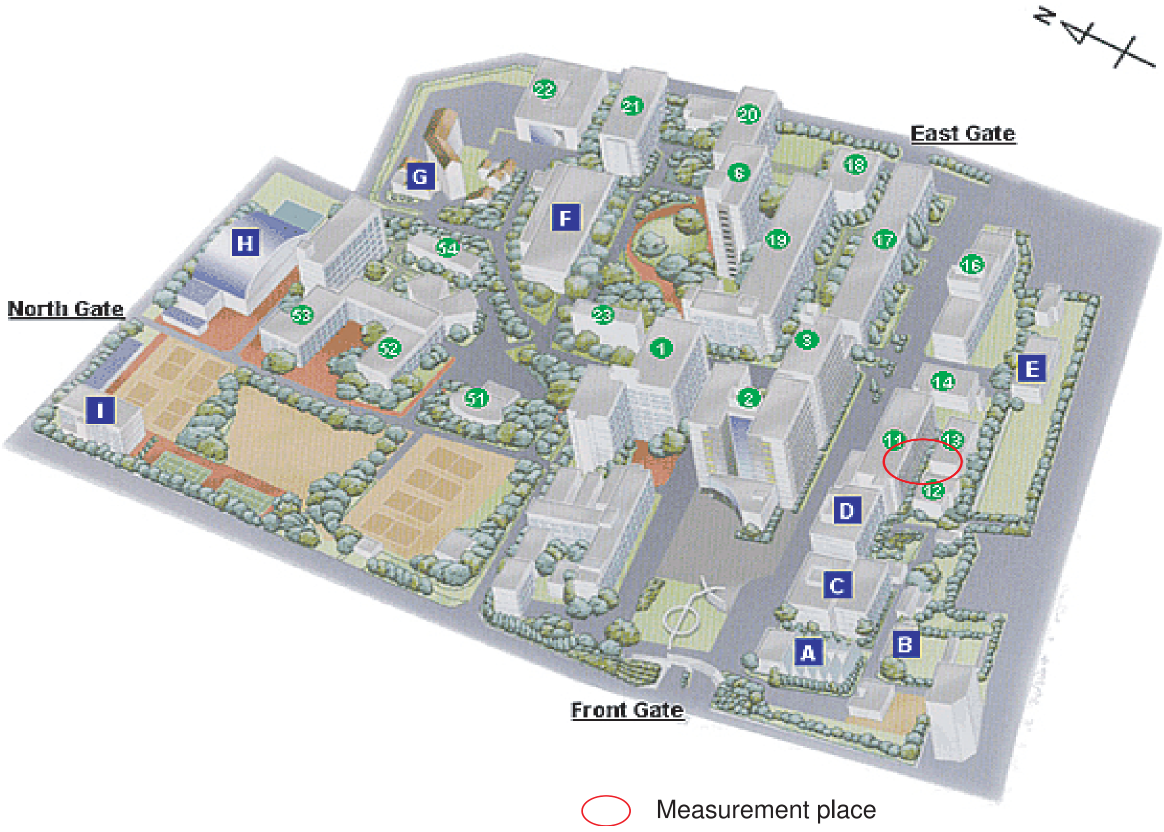
N
East Gate
North Gate
Front Gate
22
21
20
G
6
18
F
H
54
19
17
16
53
23
1
3
52
E
14
51
2
I
11
13
12
D
C
A
B
Measurement place

Figure 4.4 Campus map Nagoya Institute of Technology (NIT) to show the location of outdoor measurement.

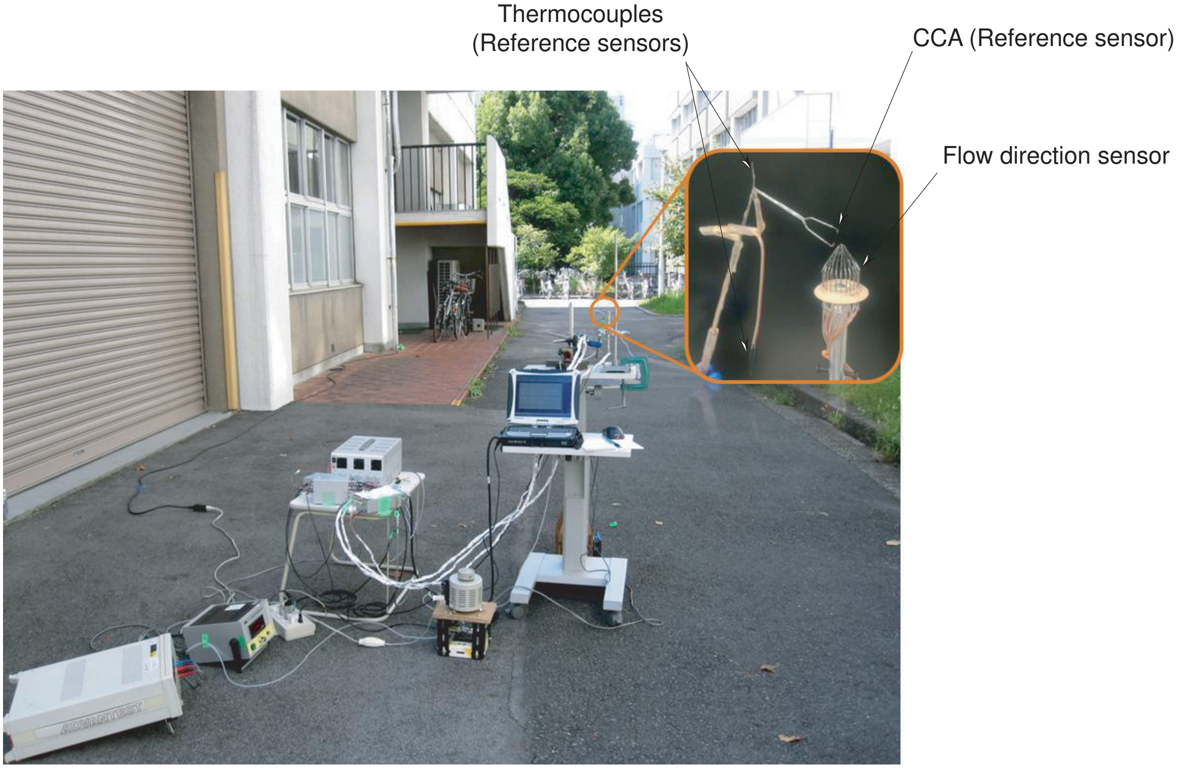
Thermocouples
(Reference sensors)
CCA (Reference sensor)
Flow direction sensor

Figure 4.5 Outdoor measurement using flow-direction sensor near the Building No. 12 in the campus of NIT.

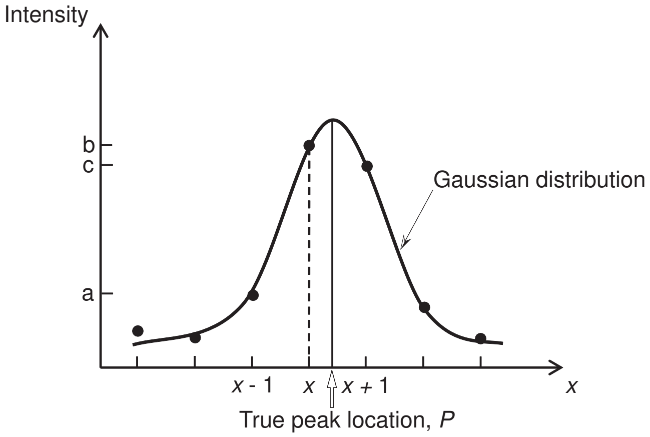

Figure 4.6 Schematic diagram for finding a true peak using Gaussian fitting.

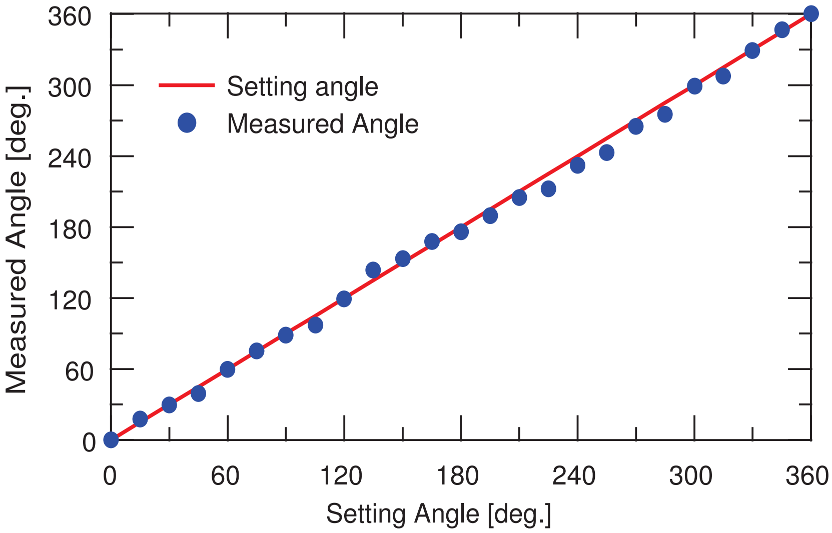

Figure 4.7 Test of the flow-direction sensor by indoor calibration experiment.

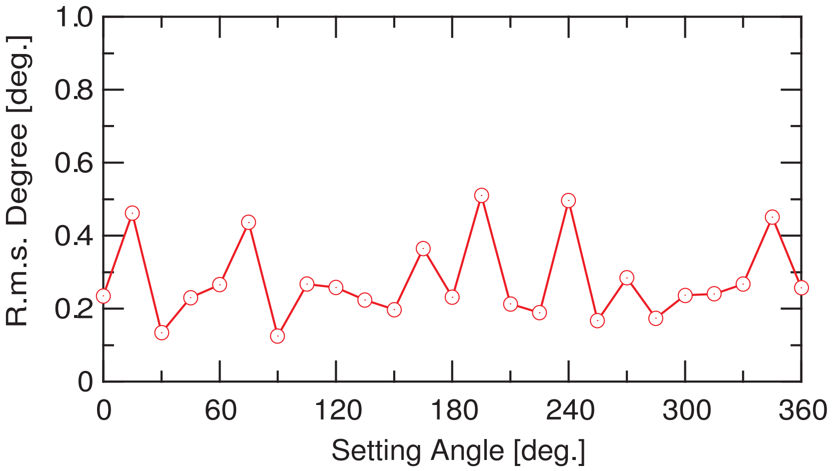

Figure 4.8 Fluctuation intensities (r.m.s. values) of flow-direction angle obtained in indoor measurement.

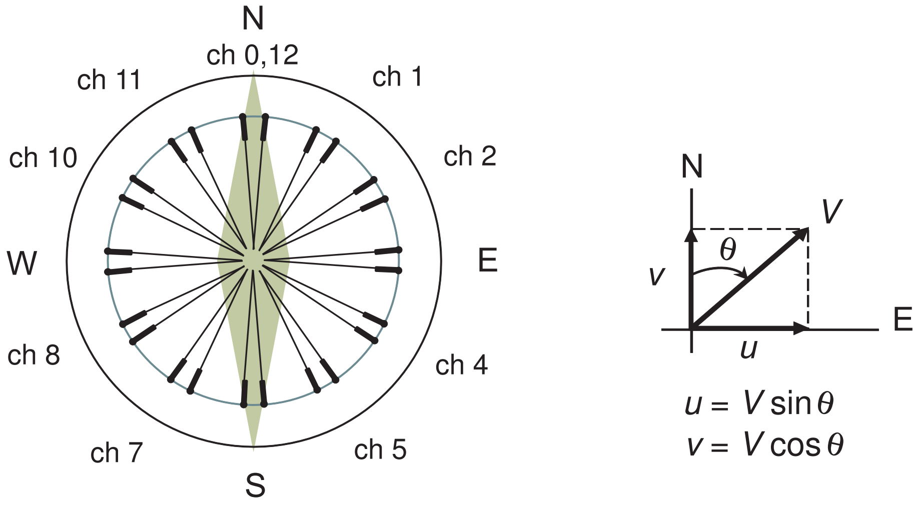
N
ch 0,12
ch 11
ch 1
ch 10
ch 2
W
E
ch 8
ch 4
ch 7
ch 5
S
N
V
θ
v
E
u
u = V sin θ
v = V cos θ

(a) (b)

Figure 4.9 Schematic diagrams for showing the principle operation of flow-direction and flow-velocity measurement: (a) Arrangement of twelve thermocouples for detecting flow-direction; (b) Decomposition of flow-direction measurement into two velocity components in the Cartesian coordinates.

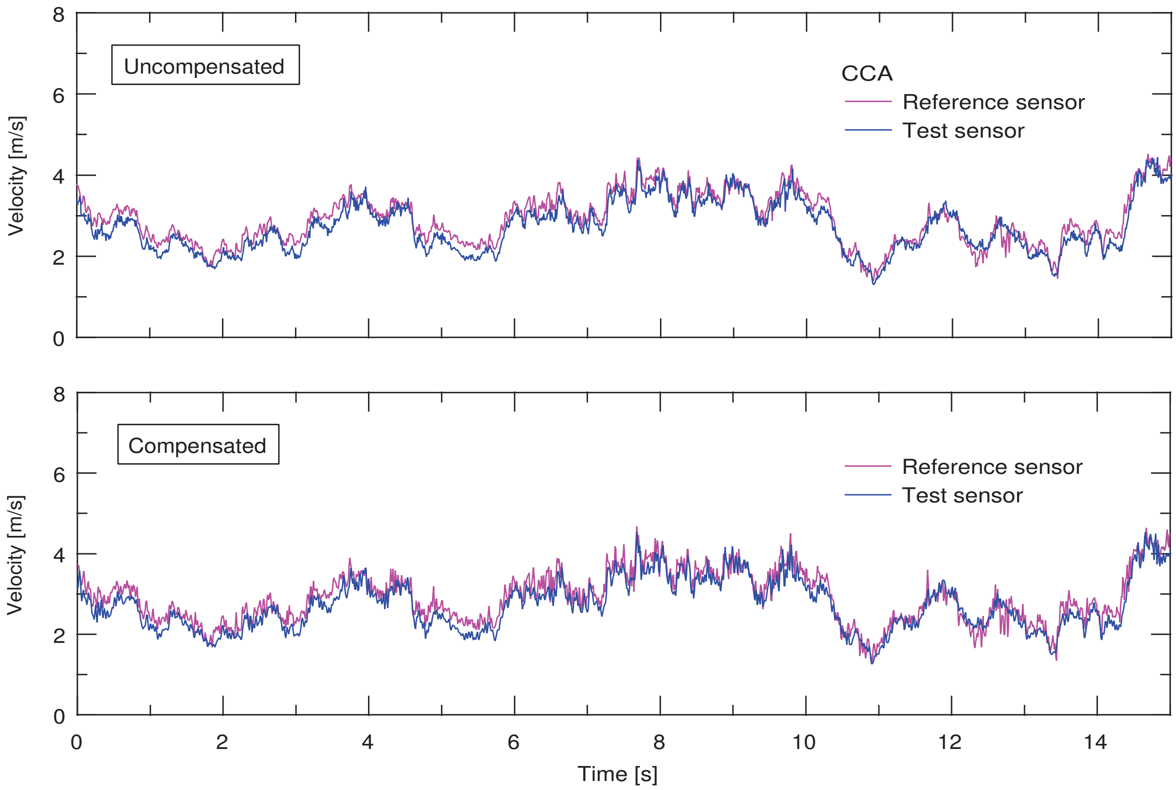

Figure 4.10 Sample instantaneous signal traces of flow velocities measured by the CCA reference (tungsten wire 10 μm in diameter) and test (nichrome coil) sensors.The upper figure shows the raw (uncompensated) data and the lower one the results obtained by the response compensation for the CCA sensors.

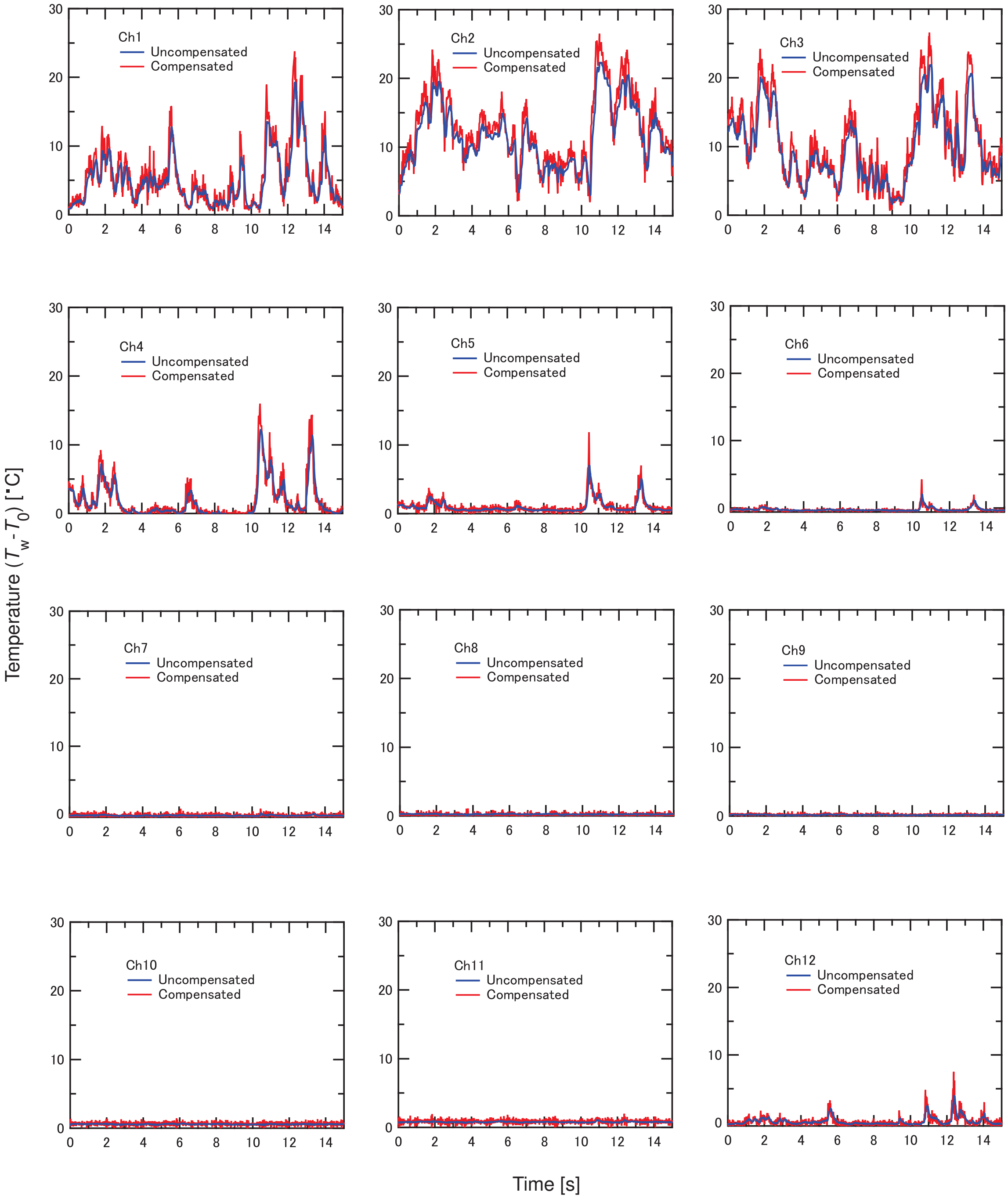

Figure 4.11 Sample flow-direction measurement in steady wind conditions: The instantaneous signal traces of the twelve type-K thermocouples in outdoor measurement conducted near Building No.12.

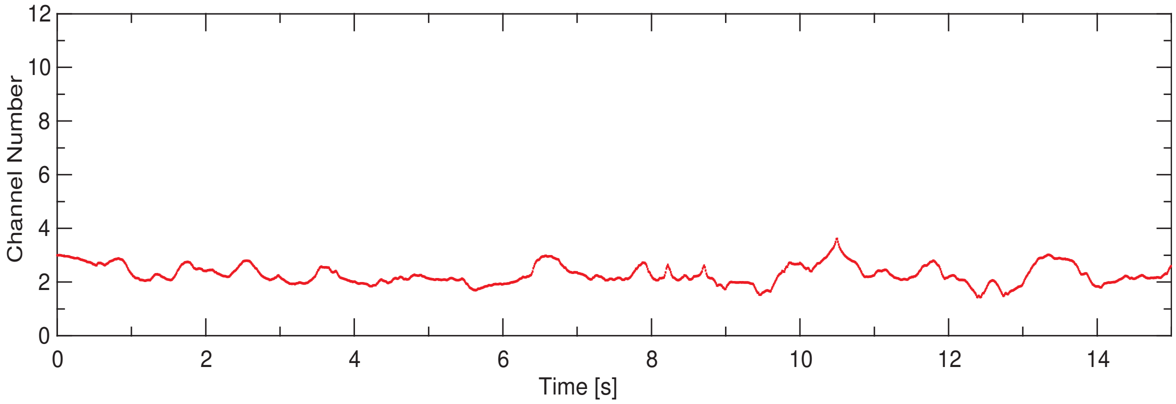

Figure 4.12 Sample flow-direction measurement in outdoor measurement conducted near Building No. 12 under steady wind conditions: The detected flow-direction is represented by the channel numbers of the twelve thermocouples.

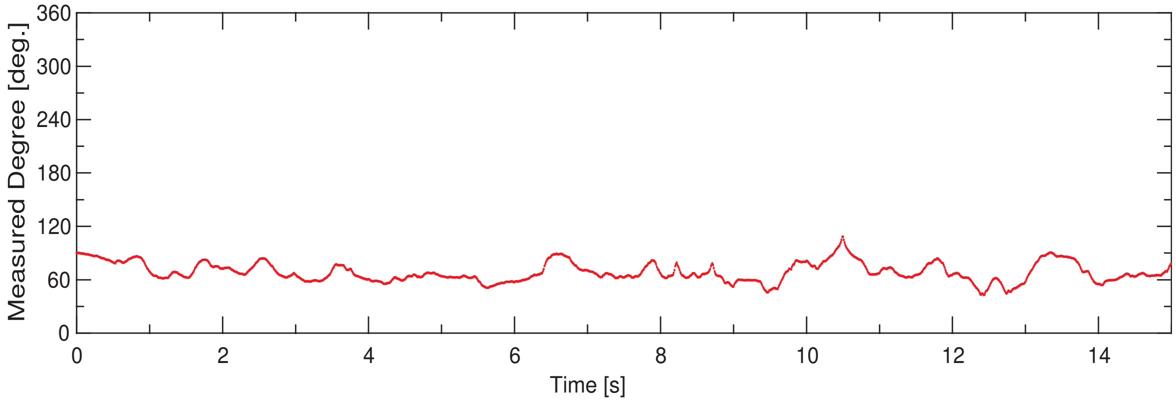

Figure 4.13 Flow-direction measurement in outdoor measurement conducted near Building No. 12 under steady wind conditions. The wind direction is represented by the angle to the north direction (0 or 360 degree).

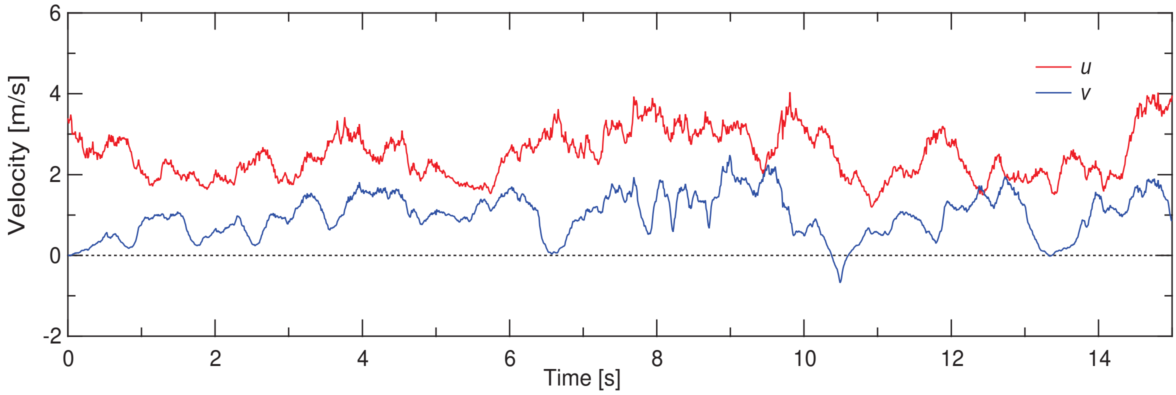

Figure 4.14 Flow-velocity measurement by the CCA sensor (nichrome coil) conducted near Building No. 12 under steady wind conditions: The results are shown in the two velocity components decomposed using both flow-velocity and flow-direction measurements.

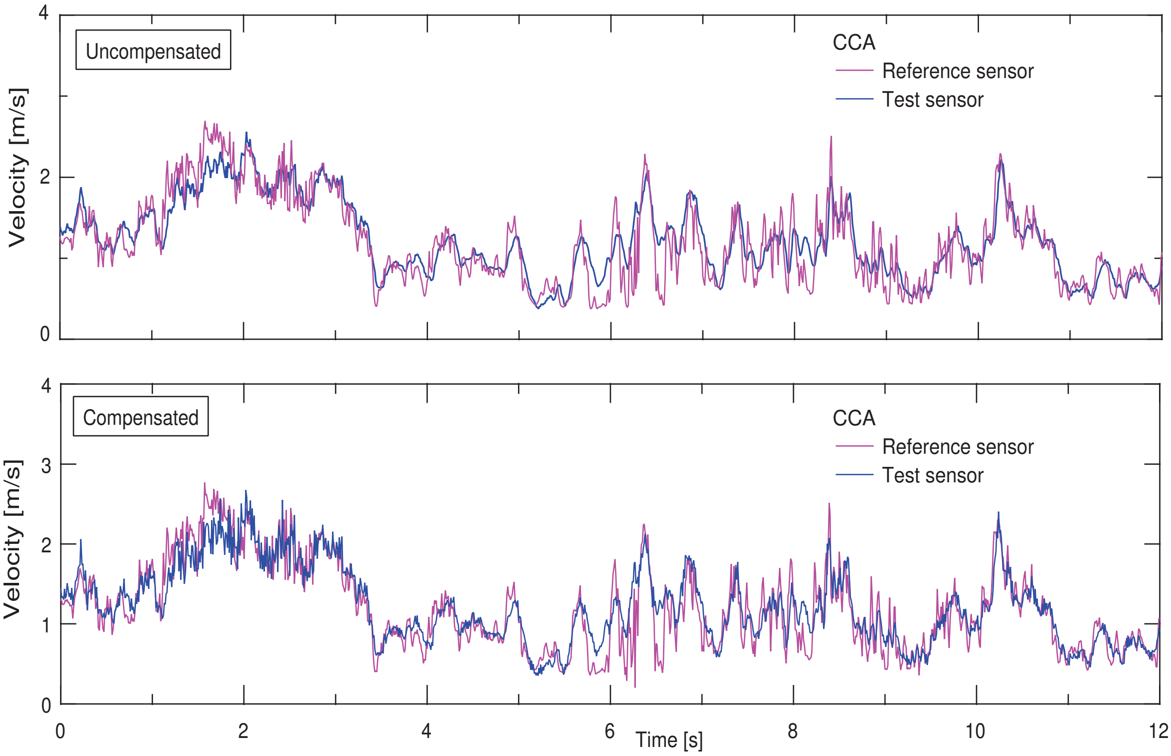

Figure 4.15 Sample flow-velocity measurements by the CCA sensor (nichrome coil whose diameter is 20 μm) and the reference one (tungsten wire 10 μm in diameter) under complex wind conditions.

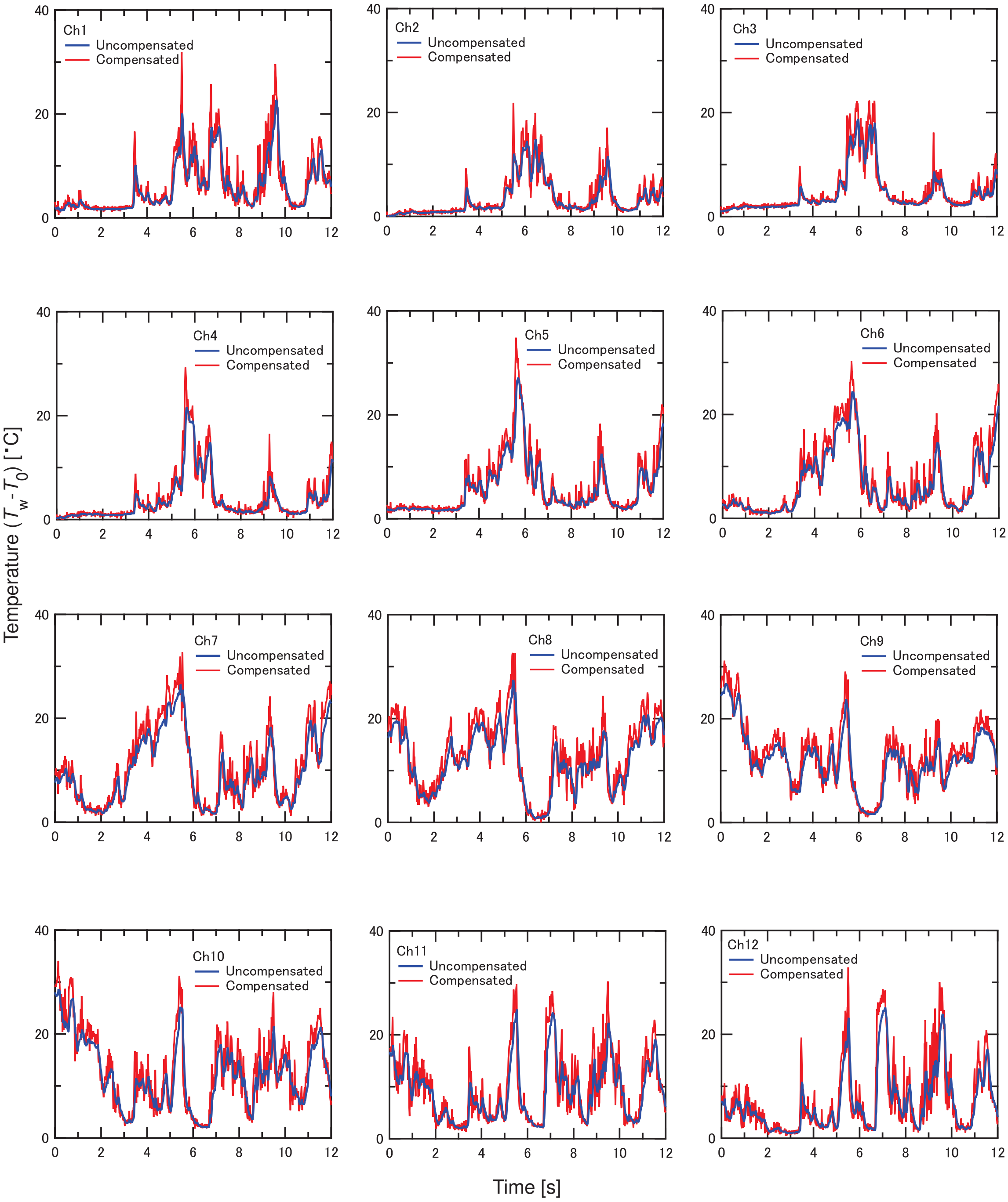

Figure 4.16 Comparison of instantaneous signal traces measured under complex wind conditions between the uncompensated (raw) thermocouple outputs and compensated ones.

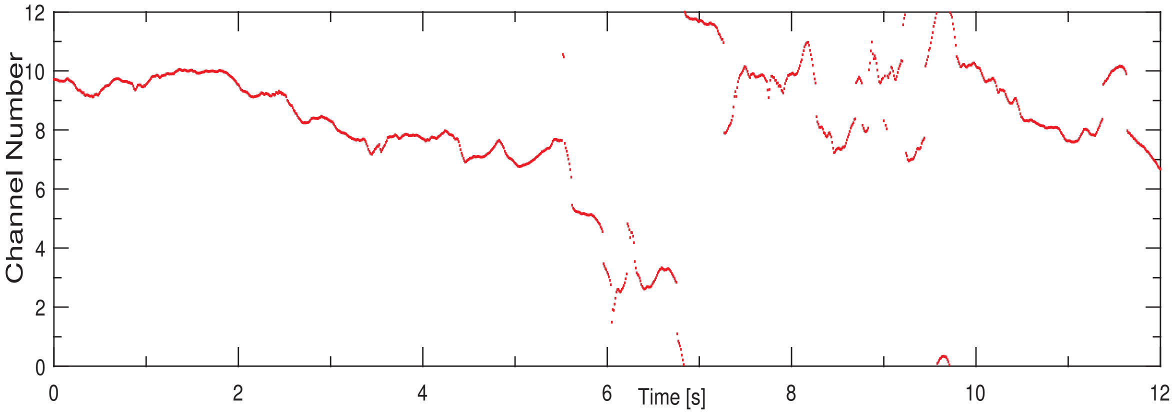

Figure 4.17 Sample flow-direction measurement in outdoor measurement conducted near Building No. 12 under unsteady wind conditions: The detected flow-direction is represented by the channel numbers of the twelve thermocouples.

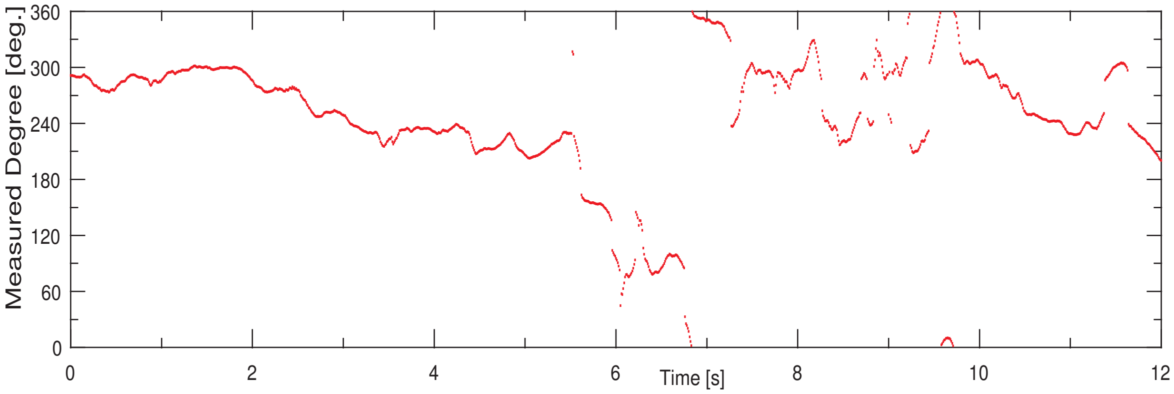

Figure 4.18 Flow-direction measurement in outdoor measurement conducted near Building No. 12 under unsteady wind conditions. The wind direction is represented by the angle to the north direction (0 or 360 degree).

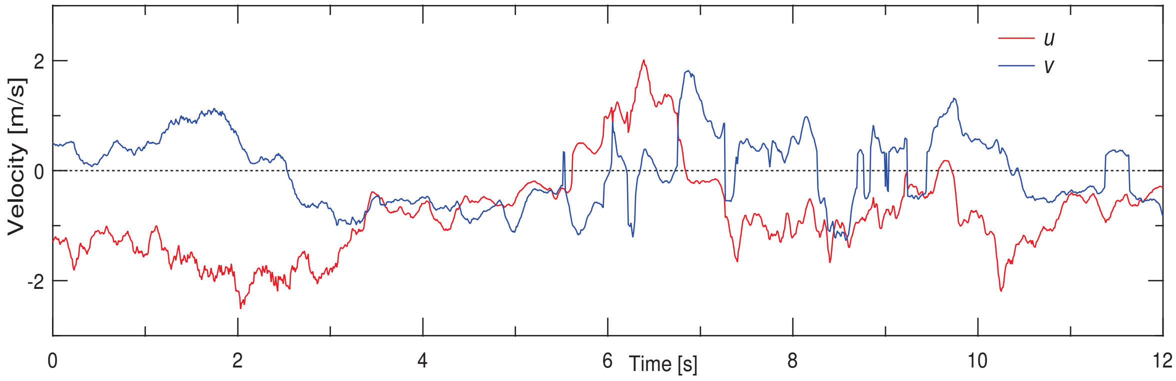

Figure 4.19 Flow-velocity measurement by the CCA sensor (nichrome coil) conducted near Building No. 12 under unsteady wind conditions: The results are shown in the two velocity components decomposed using both the velocity and flow-direction measurements.

Chapter 5

Conclusions

Fine-wire sensors have been widely used in thermo-fluid measurement and enable us to measure fluid temperatures and flow velocities of various flow fields. Although the most remarkable feature of the fine-wire sensor techniques is to be easy to use and available at low cost, we can also achieve high-precision measurement provided that we fully understand their static and dynamic response characteristics to use them appropriately.

The purpose of the present study is to analyze theoretically the static and dynamic response characteristics of the fine-wire sensors and to verify experimentally the effectiveness of the theoretical results in order to improve the accuracy and reliability of thermofluid measurement by the fine-wire sensors. In addition, based on the essential knowledge and technical experiences obtained so far, we have succeeded in developing a novel miniature flow-direction sensor which is applicable to outdoor measurement of complex flow fields and verified its potential for micrometeorological measurement. The results are summarized as follows:

[1] The constant-current hot-wire anemometer (CCA) can be realized with a very simple and low-cost electric circuit for heating the hot-wire. In the present study, an adaptive response compensation techniques to compensate for the response lag of the CCA has been proposed by taking advantage of digital signal processing technology. First, the frequency response of the hot-wires—5 μm, 10 μm and 20 μm in diameter—driven by the constant-current circuit was investigated by using the theoretically-derived frequency response function. Then, a precise response compensation scheme based on the frequency response function of the CCA (Kaifuku *et al.* 2010, 2011) has been developed, and its effectiveness was verified experimentally. Furthermore, another novel technique based on the two-sensor probe technique has been proposed, which enables *in-situ* estimation of the thermal time-constants of the hot-wires driven at the CCA mode to realize reliable response compensation of the CCA. To demonstrate the usefulness of the CCA, the response compensation schemes has been applied to the multipoint velocity measurement of a turbulent far wake of the circular cylinder by using the multi-sensor probe consisting of 16 hot-wires driven simultaneously by the very simple constant-current circuit. As a result, the proposed response compensation techniques for the CCA worked quite successfully and are capable of improving the response speed of the CCA to obtain reliable measurements comparable to those by the commercially-available constant-temperature hot-wire anemometer.

[2] The heat-conduction error of temperature sensors in the measurement of fluid flows with nonuniform and/or unsteady temperature distribution was analyzed theoretically, and a widely applicable estimation and evaluation formula of heat conduction error have been derived successfully. The validity of the proposed formula has been verified experimentally in a wake flow formed behind an electric heater and a candle flame. As a result, it is confirmed that the proposed formula can represent accurately the experimental behaviors of the heat-conduction error which cannot be explained appropriately by the existing formula. Furthermore, the effects of the heat-conduction error on the fluctuating temperature measurement of a non-isothermal unsteady fluid flow has been analyzed theoretically to derive the frequency response of the temperature sensor to be used. The analysis result shows that the heat-conduction error in temperature-fluctuation measurement appears only in a low-frequency range. Therefore, if the power-spectrum distribution of temperature fluctuations to be measured is sufficiently away from the low-frequency range, the heat-conduction error has virtually no effect on the temperature-fluctuation measurements even by the temperature sensor accompanying the heat-conduction error in the mean-temperature measurements.

[3] An effort has been made for measuring flow velocity and direction simultaneously using a coordinated velocity and temperature sensor for outdoor measurement. A heated fine-wire driven at constant-current (CC) mode was used so as to function not only as a velocity sensor but also as a heat source for twelve fine-wire thermocouples equiangularly surrounding the heated wire. An array of these twelve K-type

thermocouples can work as a flow direction sensor by detecting heat convection from the upstream heat source generated by the heated fine-wire. The performance of the coordinated velocity and temperature sensor thus developed was tested in outdoor measurement of complex flow fields, and its effectiveness in the application to micrometeorological investigation has been verified.

Appendix A

Theoretically-derived frequency response function of the CCA

A.1 Theoretical solution of frequency response of CCA

In this appendix, we have summarized the theoretical derivation processes of the frequency response function of the hot-wire probe, consisting of a fine metal wire, stub parts (copper-plated ends/silver cladding of a Wollaston wire) and prongs (wire supports) (see Fig. 2.1).

Equation (2.5) should be a fundamental equation for obtaining the frequency response function expressed by Eq. (2.8). In the right-hand side of Eq. (2.5), the term $(\overline{T}_1 - T_\mathrm{a})$ representing the time-averaged temperature difference between the wire and surrounding fluid varies as a function of x. In the present analysis, however, we assume this term to be constant for simplicity and replace $\overline{T}_1$ by the spatially-averaged temperature along the wire $\overline{T}_{1,\mathrm{m}}$, and similarly $\overline{T}_2$ by $\overline{T}_{2,\mathrm{m}}$ for the stub. As a result, the responses of the wire and stub temperatures to the velocity fluctuation u and the relevant boundary conditions are written as:

- Wire ($0 \leq x \leq \ell/2$):

$$\frac{\partial t_1}{\partial \tau} = -\frac{1}{\tau_1} t_1 + a_1 \frac{\partial^2 t_1}{\partial x^2} - \frac{\pi d_1 B_1 n \overline{U}^{n-1}}{\rho_1 c_1 S_1} (\overline{T}_{1,\mathrm{m}} - T_\mathrm{a})\, u. \tag{A1}$$

- Stub ($\ell/2 \leq x \leq L/2$):

$$\frac{\partial t_2}{\partial \tau} = -\frac{1}{\tau_2} t_2 + a_2 \frac{\partial^2 t_2}{\partial x^2} - \frac{\pi d_2 B_2 n \overline{U}^{n-1}}{\rho_2 c_2 S_2} (\overline{T}_{2,\mathrm{m}} - T_\mathrm{a})\, u. \tag{A2}$$

- Boundary conditions for Eqs. (A1) and (A2):

$$\left.\begin{array}{lll} \text{i)} & x = 0: & \dfrac{\partial t_1}{\partial x} = 0, \\[2ex] \text{ii)} & x = \ell/2: & t_1 = t_2, \\[2ex] \text{iii)} & x = \ell/2: & \dfrac{\pi}{4} d_1^2 \lambda_1 \dfrac{\partial t_1}{\partial x} = \dfrac{\pi}{4} d_2^2 \lambda_2 \dfrac{\partial t_2}{\partial x}, \\[2ex] \text{iv)} & x = L/2: & t_2 = 0. \end{array}\right\} \tag{A3}$$

The boundary conditions i) – iv) shown in Eq. (A3) are formulated so as to represent the following physical requirements: i) a temperature distribution along the heated wire is symmetrical about the origin of the x axis ($x = 0$); ii) at the interface ($x = \ell/2$), the temperature of the wire is equal to that of the stub; iii) heat flowing through the interface ($x = \ell/2$) is assumed to be conserved; and iv) the temperature at the tip of the prong (namely, temperature of the stub at $x = L/2$) is kept at fluid temperature T_a. In the following, we investigate theoretically the frequency response of the CCA along the lines of the procedure used in the analyses of the frequency response of a fine-wire temperature sensor (Tsuji *et al.* 1992; Tagawa *et al.* 2005) and a thermistor (Tagawa *et al.* 2003). The temperatures of the wire and the stub, $t_1(\tau, x)$ and $t_2(\tau, x)$, and the flow velocity $u(\tau)$ can be written using the Fourier integrals as follows:

$$\left.\begin{aligned} t_1(\tau, x) &= \int_{-\infty}^{\infty} \mathrm{e}^{j\omega\tau}\, \hat{t}_1(\omega, x)\,\mathrm{d}\omega, \\ t_2(\tau, x) &= \int_{-\infty}^{\infty} \mathrm{e}^{j\omega\tau}\, \hat{t}_2(\omega, x)\,\mathrm{d}\omega, \\ u(\tau) &= \int_{-\infty}^{\infty} \mathrm{e}^{j\omega\tau}\, \hat{u}(\omega)\,\mathrm{d}\omega, \end{aligned}\right\} \tag{A4}$$

where j is an imaginary unit and ω an angular frequency ($\equiv 2\pi f$). From Eq. (A4), Eqs. (A1) and (A2) are transformed into the following equations:

$$\left.\begin{aligned} \frac{\partial^2[\hat{t}_1(\omega, x)]}{\partial x^2} - \frac{1 + j\omega\tau_1}{a_1\tau_1}\, \hat{t}_1(\omega, x) &= \frac{Z_{1,\mathrm{m}}}{a_1}\hat{u}(\omega), \\ \frac{\partial^2[\hat{t}_2(\omega, x)]}{\partial x^2} - \frac{1 + j\omega\tau_2}{a_2\tau_2}\, \hat{t}_2(\omega, x) &= \frac{Z_{2,\mathrm{m}}}{a_2}\hat{u}(\omega), \end{aligned}\right\} \tag{A5}$$

where $Z_{i,\mathrm{m}}$ (i=1, 2) is represented by

$$Z_{i,\mathrm{m}} = \frac{\pi d_i B_i n \overline{U}^{n-1}}{\rho_i c_i S_i}(\overline{T}_{i,\mathrm{m}} - T_\mathrm{a}). \tag{A6}$$

Equation (A5) is composed of the two differential equations on the variable (coordinate) x, and their solutions are given by

$$\left.\begin{aligned} \hat{t}_1(\omega, x) &= C_1'\,\mathrm{e}^{\Omega_1 x} + C_2'\,\mathrm{e}^{-\Omega_1 x} - \frac{Z_{1,\mathrm{m}}}{\Omega_1^2 a_1}\hat{u}(\omega), \\ \hat{t}_2(\omega, x) &= C_3'\,\mathrm{e}^{\Omega_2 x} + C_4'\,\mathrm{e}^{-\Omega_2 x} - \frac{Z_{2,\mathrm{m}}}{\Omega_2^2 a_2}\hat{u}(\omega), \end{aligned}\right\} \tag{A7}$$

where $C'_1 - C'_4$ are the undetermined coefficients, and Ω_i $(i = 1,\ 2)$ is defined by

$$\begin{aligned}\Omega_i &\equiv \sqrt{\frac{1 + j\omega\tau_i}{a_i\tau_i}} \\ &= \frac{1}{\sqrt{2a_i\tau_i}}\left(\sqrt{\sqrt{1+\omega^2\tau_i^2}+1} + j\sqrt{\sqrt{1+\omega^2\tau_i^2}-1}\right).\end{aligned} \tag{A8}$$

The boundary conditions i) - iv) in Eq. (A3) are also written in the Fourier integrals, and are used to determine the coefficients $C'_1 - C'_4$ in Eq. (A7). As a result, the frequency component of the wire temperature, $\hat{t}_1$, becomes

$$\hat{t}_1(\omega, x) = \left[2k\cosh(\Omega_1 x) - \frac{Z_{1,\mathrm{m}}}{\Omega_1^2 a_1}\right]\hat{u}(\omega), \tag{A9}$$

where k is given by

$$\begin{aligned}k =& \left[\frac{Z_{2,\mathrm{m}}}{\Omega_2^2 a_2} + \left(\frac{Z_{1,\mathrm{m}}}{\Omega_1^2 a_1} - \frac{Z_{2,\mathrm{m}}}{\Omega_2^2 a_2}\right)\cosh\left(\frac{\Omega_2(L-\ell)}{2}\right)\right] \\ &\times \left[2\cosh\left(\frac{\Omega_1\ell}{2}\right)\cosh\left(\frac{\Omega_2(L-\ell)}{2}\right)\right. \\ &\left. + 2\frac{\Omega_1 d_1^2\lambda_1}{\Omega_2 d_2^2\lambda_2}\sinh\left(\frac{\Omega_1\ell}{2}\right)\sinh\left(\frac{\Omega_2(L-\ell)}{2}\right)\right]^{-1}.\end{aligned} \tag{A10}$$

It is assumed that the wire temperature $\overline{T}_1$ can be replaced by the mean temperature $\overline{T}_{1,\mathrm{m}}$ spatially-averaged in the range of $-\ell/2 \le x \le \ell/2$. Therefore, we may appraise the frequency response of the wire by averaging $\hat{t}_1(\omega, x)$ in the same range and the result $\hat{t}_{1,\mathrm{m}}(\omega)$ is described as follow:

$$\begin{aligned}\hat{t}_{1,\mathrm{m}}(\omega) &= \frac{1}{\ell}\int_{-\ell/2}^{\ell/2}\hat{t}_1(\omega, x)\mathrm{d}x \\ &= \left[\frac{2k}{\frac{\Omega_1\ell}{2}}\sinh\left(\frac{\Omega_1\ell}{2}\right) - \frac{Z_{1,\mathrm{m}}}{\Omega_1^2 a_1}\right]\hat{u}(\omega).\end{aligned} \tag{A11}$$

From the above Eq. (A11), we finally obtain the frequency response of the hot-wire probe driven by the CCA, $H_1(\omega)$ $[\equiv \hat{t}_{1,\mathrm{m}}(\omega)/\hat{u}(\omega)]$. The result is given by Eq. (2.8). Similarly, the frequency response of the stub $H_2(\omega)$ $\left[\equiv \hat{t}_{2,\mathrm{m}}(\omega)/\hat{u}(\omega)\right]$ can be obtained by determining the values of C_3' and C_4' in Eq. (A7) (not shown). If there is no stub (i.e., $L = \ell$), the wire is directly connected to the prong. Eq. (2.8) is reduced to the following simple expression:

$$H_1(\omega) = -\frac{Z_{1,\mathrm{m}}}{\Omega_1^2 a_1}\left[1 - \frac{\tanh\left(\Omega_1 \ell/2\right)}{\Omega_1 \ell/2}\right]. \tag{A12}$$

To investigate the frequency response of the CCA using Eq. (2.8), we need to evaluate the heat transfer coefficient h that plays a key role in determining the time constants τ_1 and τ_2 as shown in Eq. (2.6). In the present study, we use the well-known Collis-Williams correlation equation (Collis and Williams 1959), which is given by

$$\begin{aligned} \mathrm{Nu}\left(\frac{T_\mathrm{f}}{T_\mathrm{a}}\right)^{-0.17} &= 0.24 + 0.56\,\mathrm{Re}^{0.45}, \\ &\quad (0.02 < \mathrm{Re} < 44) \end{aligned} \tag{A13}$$

where Nu and Re are the Nusselt and Reynolds numbers, respectively and are defined as $\mathrm{Nu} = hd/\lambda_\mathrm{a}$ and $\mathrm{Re} = Ud/\nu_\mathrm{a}$ (U: flow velocity; ν_a: kinematic viscosity of fluid); and T_f is a film temperature defined as $T_\mathrm{f} = (T + T_\mathrm{a})/2$ (T: surface temperature of the wire).

A.2 Frequency response of CCA

In this section, we investigate in detail the frequency response characteristics of the CCA to obtain basic knowledge of the response compensation of its output. As for the hot-wire probe to be analyzed, a fine tungsten wire 5 μm in diameter is supported by copper stubs 35 μm in diameter, and the end of the stub is connected to the prong tip. In the present analysis, the distance between the prongs (see Fig. 2.1), air flow velocity, fluid temperature and the electric current to drive the CCA are set to 5 mm, 4 m/s , 25 °C and 40 mA, respectively. First, we investigated the frequency response as a function of the wire length. The results are shown in Fig. A1. As seen from Fig. A1 (a), the gain rises considerably with increasing wire length, since the heat loss due to conduction becomes increasingly dominant as the wire length decreases. Naturally, the gain becomes lowest in the case of the shortest wire. Figures A1 (b) and (c) show the Bode diagram (gain and phase) of the CCA output, where the gain is normalized by the respective values at frequency $f = 0$ Hz. In practice, the Bode diagram shown in Figs. A1 (b) and (c) can facilitate the comparison of the effects of the wire length on the response of the hot-wire output, and we may gain a deeper understanding of the response characteristics of the CCA. As shown in Figs. A1 (b) and (c), although the absolute gain attenuates considerably [Fig. A1(a)], the frequency response improves in a high-frequency region over 200 Hz as the aspect ratio of the wire decreases. This is because the relative thermal inertia of the system consisting of the wire, stub and the prong diminishes with decreasing aspect ratio of the wire. On the other hand, the gain in a low-frequency region smaller than 200 Hz increases, and approaches the first-order lag system. In this first-order lag system, the gain and phase take the values of $2^{-1/2} = 0.707$ and $-\pi/4 = -45$ degrees, respectively. From these results, the no-stub case with $\ell/d = 100$ will give the most ideal frequency response except that the absolute gain attenuates enormously. In this contradictory situation, therefore, we must optimize the wire length by taking into account the overall signal-to-noise ratio of the measurement system used. It is noted here that being different from the CCA, the frequency response of the fine-wire temperature sensors will deviate largely from the first-order lag system even if the aspect ratio ℓ/d is greater than 400 (Tagawa *et al.* 2005).

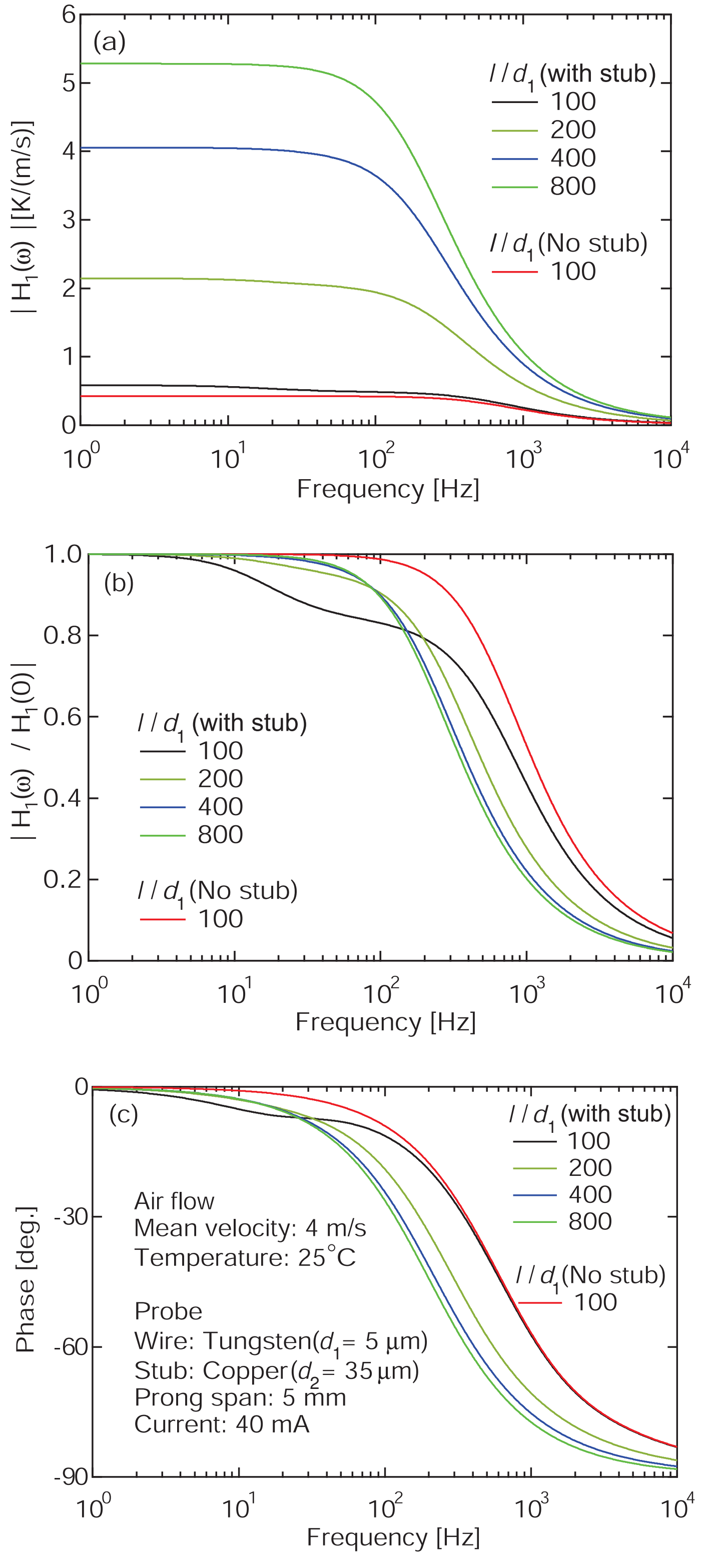

Figure A1 Frequency response of CCA obtained using Eq. (2.8): (a) Absolute gain; (b) Normalized gain; (c) Phase

Appendix B

Additional information on present theoretical model for heat-conduction error and derivation of frequency response function of temperature sensor with heat-conduction error

B.1 Additional information on present theoretical model for heat-conduction error

In addition, if the value $n = 1$ is put into the Eq. (3.12), we obtain an estimation equation of heat conduction error when there is no constant temperature [the temperature T_0 is fixed at the boundary condition ($x = L$) of the main part of a sensor and a

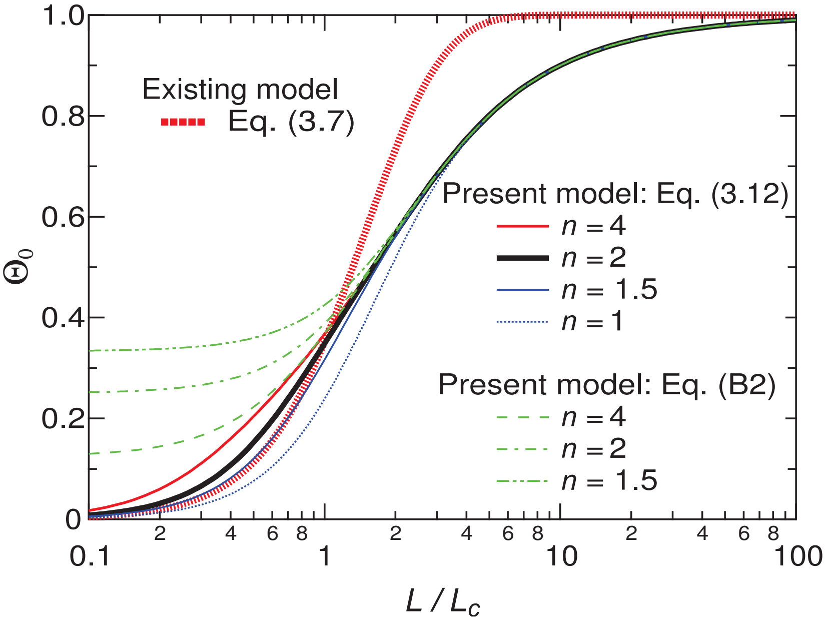

Figure B1 Comparison of heat-conduction error estimated between the existing equation [Eq. (3.7)] and the proposed ones [Eq. (3.12) and (B2)].

support part]. The result is given as follow:

$$\Theta_0 = 1 - \frac{\tanh(L/L_\mathrm{c})}{L/L_\mathrm{c}}. \tag{B1}$$

On the other hand, if we apply an adiabatic condition ($x = nL$), Θ_0 can be given by the following equation:

$$\begin{aligned}\Theta_0 &= 1 - \frac{L_\mathrm{c}}{L}\left[1 - \frac{\mathrm{e}^{2(n-1)L/L_\mathrm{c}} - 2\mathrm{e}^{-L/L_\mathrm{c}} + 1}{\mathrm{e}^{(2n-1)L/L_\mathrm{c}} - \mathrm{e}^{-L/L_\mathrm{c}}}\right] \\ &= 1 - \frac{L_\mathrm{c}}{L}\left[\frac{\mathrm{e}^{nL/L_\mathrm{c}} + \mathrm{e}^{-nL/L_\mathrm{c}} - \mathrm{e}^{(n-1)L/L_\mathrm{c}} - \mathrm{e}^{-(n-1)L/L_\mathrm{c}}}{\mathrm{e}^{nL/L_\mathrm{c}} + \mathrm{e}^{-nL/L_\mathrm{c}}}\right] \\ &= 1 - \frac{\cosh(nL/L_\mathrm{c}) - \cosh[(n-1)L/L_\mathrm{c}]}{(L/L_\mathrm{c})\sinh(nL/L_\mathrm{c})}.\end{aligned} \tag{B2}$$

It is noted that Eq. (B2) approaches $1/(2n)$ in the limit of $L/L_\mathrm{c} \to 0$.

The calculation result of Eq. (B2) is together shown in Fig. B1 with all results of Eq. (3.7) and Eq. (3.12). In the figure, if the value of parameter n increases, the effect of the difference in the boundary condition $x = nL$ on the calculation result of the existing Eq. (B2) becomes smaller.

B.2 Derivation of frequency response function of temperature sensor with heat-conduction error

In what follows, the derivation of Eq. (3.19) is described in detail. The temperature fluctuations of the sensor body, $t_{\mathrm{w}}, (t, x)$, fluid, $t_{\mathrm{a}}(t, x)$, and fluid at the measurement position, $t_{\mathrm{m}}(t)$, can be represented by the Fourier integrals as follows:

$$\begin{cases} t_{\mathrm{w}}(t,x) = \displaystyle\int_{-\infty}^{\infty} \hat{t}_{\mathrm{w}}(\omega,x)\mathrm{e}^{j\omega t}\mathrm{d}\omega, \\ t_{\mathrm{a}}(t,x) = \displaystyle\int_{-\infty}^{\infty} \hat{t}_{\mathrm{a}}(\omega,x)\mathrm{e}^{j\omega t}\mathrm{d}\omega, \\ t_{\mathrm{m}}(t) = \displaystyle\int_{-\infty}^{\infty} \hat{t}_{\mathrm{m}}(\omega)\mathrm{e}^{j\omega t}\mathrm{d}\omega. \end{cases} \tag{B3}$$

The substitution of Eq. (B3) into Eq. (3.19) and its rearrangement yields the governing equation expressed by the Fourier components $\hat{t}_{\mathrm{w}}(\omega, x)$ and $\hat{t}_{\mathrm{a}}(\omega, x)$ as:

$$\frac{\mathrm{d}^2\hat{t}_{\mathrm{w}}}{\mathrm{d}x^2} - \frac{1 + j\tau\omega}{a\tau}\hat{t}_{\mathrm{w}} = -\frac{\hat{t}_{\mathrm{a}}}{a\tau}, \tag{B4}$$

Similarly, the boundary conditions given in section 3.1.3 can be written in the

Fourier components as follows:

$$\begin{cases} x=0: \ \dfrac{\mathrm{d}\hat{t}_{\mathrm{w1}}}{\mathrm{d}x}=0, \\[2ex] x=L: \ \hat{t}_{\mathrm{w1}}=\hat{t}_{\mathrm{w2}}, \\[2ex] x=L: \ \dfrac{\mathrm{d}\hat{t}_{\mathrm{w1}}}{\mathrm{d}x}=\dfrac{\mathrm{d}\hat{t}_{\mathrm{w2}}}{\mathrm{d}x}, \\[2ex] x=nL: \ \hat{t}_{\mathrm{w2}}=0, \end{cases} \tag{B5}$$

where $\hat{t}_{\mathrm{w}}(\omega,x)$ for $0\le x\le L$ and that for $L\le x\le nL$ are expressed as $\hat{t}_{\mathrm{w1}}(\omega,x)$ and $\hat{t}_{\mathrm{w2}}(\omega,x)$, respectively.

On the other hand, the Fourier component of fluid temperature fluctuation, $\hat{t}_{\mathrm{a}}(\omega,x)$, can be rewritten using the Fourier component at the measurement position, $\hat{t}_{\mathrm{m}}(t)$, and is given by

$$\hat{t}_{\mathrm{a}}(\omega,x)=\begin{cases}\left(1-\dfrac{x}{L}\right)\hat{t}_{\mathrm{m}}(\omega) & (0\le x\le L), \\[2ex] 0 & (L\le x\le nL). \end{cases} \tag{B6}$$

By inserting Eq. (B6) into Eq. (B4) and integrating it, we obtain the general solutions of $\hat{t}_{\mathrm{w1}}(\omega,x)$ and $\hat{t}_{\mathrm{w2}}(\omega,x)$ as:

- For $0\le x\le L$

$$\hat{t}_{\mathrm{w1}}(\omega,x)=C_1\mathrm{e}^{\Omega x/L_{\mathrm{c}}}+C_2\mathrm{e}^{-\Omega x/L_{\mathrm{c}}}+\frac{(1-x/L)}{\Omega^2}\hat{t}_{\mathrm{m}}(\Omega), \tag{B7}$$

- For $L\le x\le nL$

$$\hat{t}_{\mathrm{w2}}(\omega,x)=C_3\mathrm{e}^{\Omega x/L_{\mathrm{c}}}+C_4\mathrm{e}^{-\Omega x/L_{\mathrm{c}}}. \tag{B8}$$

The integral constants $C_1\sim C_4$ in Eqs. (B7) and (B8) can be determined using the boundary condition given by Eq. (B5). The results are as follows (C_3 and C_4 are omitted):

$$\begin{cases} C_1 = \dfrac{1}{2\Omega^3 L/L_\mathrm{c}} \left[\dfrac{\mathrm{e}^{-n\Omega L/L_\mathrm{c}} + \sinh[(n-1)\Omega L/L_\mathrm{c}]}{\cosh(n\Omega L/L_\mathrm{c})} \right] \hat{t}_\mathrm{m}(\Omega), \\ C_2 = C_1 - \dfrac{1}{\Omega^3 L/L_\mathrm{c}} \hat{t}_\mathrm{m}(\Omega). \end{cases} \tag{B9}$$

From Eq. (B7), the Fourier component at the sensing part, $\hat{t}_\mathrm{w1}(\omega, 0)$, is given by

$$\hat{t}_\mathrm{w1}(\omega, 0) = C_1 + C_2 + \frac{1}{\Omega^2} \hat{t}_\mathrm{m}(\Omega). \tag{B10}$$

By substituting Eq. (B9) into Eq. (B10) and using the following definition of $H(\omega)$, we obtain the frequency response function given by Eq. (3.19):

$$H(\omega) \equiv \frac{\hat{t}_\mathrm{w1}(\omega, 0)}{\hat{t}_\mathrm{m}(\omega)} \tag{B11}$$

Bibliography

Adamec, R. J., Thiel, D. V. and Tanner, P. 2003 MEMS Wind direction detection: from design to operation. *Proc. IEEE* **1**, 340–343.

Berson, A., Poignand, G., Blanc-Benon, P. and Comte-Bellot, G. 2010 Capture of instantaneous temperature in oscillating flows: Use of constant-voltage anemometry to correct the thermal lag of cold wires operated by constant-current anemometry. *Rev. Sci. Instrum.* **81** (1), 015102.

Blackwelder, R.F. and Kaplan, R.E. 1976 On the wall structure of the turbulent boundary layer. *J. Fluid Mech.* **76**, 89–112.

Bradley, D. and Entwistle, A. G. 1961 Determination of the emissivity, for total radiation, of small diameter platinum-10% rhodium wires in the temperature range $600 - 1450°$C. *British J. Appl. Phys.* **12**, 708–711.

Bruun, H.H. 1995 *Hot-Wire Anemometry - Principles and Signal Analysis*, Oxford University Press, New York.

Chevray, R. and Tu Tu, N. K. 1972 Simultaneous measurements of temperature and velocity in heated flows. *Rev. Sci. Instrum.* **43**, 1417–1421.

Chomiak, J. and Niedzialek, B. 1967 Measurement of rapidly varying gas temperatures in an unsteady flow. *Int. J. Heat Mass Transfer* **10**, 1571–1579.

Collis, D.C. and Williams, M.J. 1959 Two-dimensional convection from heated wires at low Reynolds numbers. *J. Fluid Mech.* **6**, 357–384.

Comte-Bellot, G. 1976 Hot-wire anemometry. *Annu. Rev. Fluid Mech.* **8**, 209–231.

Comte-Bellot, G. 2007 *Springer Handbook of Experimental Fluid Mechanics*, C. Tropea,A. L. Yarin and J. F. Foss (eds), Springer, Berlin, Sec 5.2.1-5.2.7, 229–283.

Dong, Z., Chen, J., Qin, Y., Qin, M. and Huang, Q. A. 2012 Fabrication of a micromachined two-dimensional wind sensor by Au-Au wafer bonding technology. *J. MEMS* **21** (2), 467–475.

Fralick, G. C. and Forney, L. J. 1993 Frequency response of a supported thermocouple wire: Effects of axial conduction. *Rev. Sci. Instrum.* **64**, 3236–3244.

Glauser, M.N. and George, W.K. 1992 Application of multipoint measurements for flow characterization. *Exp. Therm. Fluid Sci.* **5**, 617–632.

Hayashi, M., Goto, Y., Hanzawa, K., Matsumoto, M., Koide, A. and Jeong, H. W. 2009 Trends in Hitachi's MEMS sensors for automobiles. *Hitachi Rew.* **58** (7), 335–340.

Hinze, J. O. 1975 *Turbulence*, 2nd edition, McGraw-Hill.

Houra, T. and Nagano, Y. 2008 Spatio-temporal turbulent structures of thermal boundary layer subjected to non-equilibrium adverse pressure gradient. *Int. J. Heat Fluid Flow* **29** (3), 591–601.

Hultmark, M. and Smits A. J. 2010 Temperature corections for constant temperature and constant current hot-wire anemometers. *Meas. Sci. Technol.* **21**, 105404 (4 pages).

Kaifuku, K., Khine, S.M., Houra, T. and Tagawa, M. 2010 Response compensation of constant-current hot-wireanemometer. In *Proc. of the 21st international symposium on transport phenomena*, Kaohsiung, Taiwan, pp 816–822

Kaifuku, K., Khine, S.M., Houra, T. and Tagawa, M. 2011 Response compensation for constant-current hot-wire anemometry based on frequency response analysis. In *Proc. ASME/JSME 2011, 8th thermal engineering joint conference*, Honolulu, AJTEC2011-44437, 8 pages.

Kaiser R. and Puits, R. du. 2012 Error estimation of temperature measurements in non-isothermal shear layers. *Exp. Fluids* **53**, 137–143.

Kaskan, W. E. 1957 The dependence of flame temperature on mass burning velocity. *Symp. (International) on Combust.* **6**, 134–143.

Kato, K., Kaifuku, K. and Tagawa, M. 2007 Fluctuating temperature measurement by a fine-wire thermocouple probe: influences of physical properties and insulation coating on the frequency response. *Meas. Sci. Tech.* **18** (3), 779–789.

Kidron, I. 1966 Measurement of the transfer function hot-wire and hot-film turbulence transducers. *IEEE Trans. Instrum. Meas.* **15** (3), 76–81.

Kidron, I. 1967 The signal-to-noise ratios of constant-current and constant-temperature hot-wire anemometers. *IEEE Trans. Instrum. Meas.* **16** (1), 68–73.

Kim, T. H. and Kim, S. J. 2006 Development of a micro-thermal flow sensor with thin-film thermocouples, *J. Micromech. Microeng.* **16**, 2502–2508.

Kobus, C. J. 2006 True fluid temperature reconstruction compensating for conduction error in the temperature measurement of steady fluid flows. *Rev. Sci. Instrum.* **77**, 034903 (10 pages).

Kottapalli, A. G. P., Tan, C. W., Olfatnia, M., Miao, J. M., Barbastathis,M. and Triantafyllou M. 2011 A liquid crystal polymer membrane MEMS sensor for flow rate and flow direction sensing applications. *J. Micromech. Microeng.* **21**, 085006 (11 pages).

Kramers, H. 1946 Heat transfer from spheres to flowing media. *Physica* **12**, 61–80.

Lee, C. Y., Wang1, Y. H., Hsueh, T. H., Ma, R. H., Fu, L. M. and Chou, P. C. 2008 A Smart Flow Sensor for Flow Direction Measurement. *Adv. Mater. Res.* **47-50**, 189–192.

Li, J. D. 2004 Dynamic response of constant temperature hot-wire system in turbulence velocity measurements. *Meas. Sci. Tech.* **15** (9), 1835–1847.

Ma, R. H., Wang, D. A., Hsueh, T. H. and Lee, C. Y. 2009 A MEMS-based flow rate and flow direction sensing platform with integrated temperature compensation scheme. *Open Access J. Sensors* **9**, 5460–5476.

Makinwa, K. A. A., Huijsing, J. H. and Hagedoorn, A. 2001 Industrial design of a solid-state wind sensor, *Sensors for Industry: Proc. First ISA/IEEE Conference*, Rosemount, Illinois, USA, 68–71.

Markus, R., Willert C. E. and Kompenhans J. 1998 *Particle Image Velocimetry: A*

Practical Guide, Springer, Verlag Berlin Heidelberg.

Minn Khine, S., Houra, T. and Tagawa, M. 2012 A Two-Sensor Probe Technique for Response Compensation of Constant-Current Hot-Wire Anemometry, *The Eight KSME-JSME Thermal and Fluids Engineering Conference*, Incheon, Korea, GSF30-005, 4 pages.

Minn Khine, S., Houra, T. and Tagawa, M. 2013 (a) Theoretical Analysis and Its Experimental Validation of Heat-Conduction Error of Temperature Sensors in a Flow Field with Mean-Temperature Gradient, *Thermal Sci. Eng.* **21** (3), 73–81.

Minn Khine, S., Houra, T. and Tagawa, M. 2013 (b) Heat-conduction error of temperature sensors in a fluid flow with nonuniform and unsteady temperature distribution, *Rev. Sci. Instrum.* **84**, 044902 (11 pages).

Minn Khine, S., Houra, T. and Tagawa, M. 2013 (c) An Adaptive Response Compensation Technique for the Constant-Current Hot-Wire Anemometer, *Open J. Fluid Dynamics* **3**, 95–108.

Nguyen, N. T. 2005 A novel thermal sensor concept for flow direction and flow velocity, *IEEE SENSORS J.* **5**, (6), 1224–1234.

Perry, A.E. 1982 *Hot-wire Anemometry*, Oxford University Press, New York.

Petit, C., Gajan, P., Lecordier, J. C. and Paranthoen, P. 1982 Frequency response of fine wire thermocouple. *J. Phy. E: Sci. Instrum.* **15**, 760–764.

Sparrow,E. M. 1976 Error estimates in temperature measurement. *Measurements in Heat Transfer*, E. R. G. Eckert and R. J. Goldstein (eds), Hemisphere, 1–23.

Tagawa, M. and Ohta, Y. 1997 Two-thermocouple probe for fluctuating temperature measurement in combustion–Rational estimation of mean and fluctuating time constants. *Combust. Flame* **109**, 549–560.

Tagawa, M., Shimoji, T. and Ohta, Y. 1998 A two-thermocouple technique for estimating thermocouple time constants in flows with combustion: In situ parameter identification of a first-order lag system. *Rev. Sci. Instrum.* **69** (9), 3370–3378.

Tagawa, M., Nagaya, S. and Ohta, Y. 2001 Simultaneous measurement of velocity and temperature in high-temperature turbulent flows: a combination of LDV and three-wire temperature probe. *Exp. Fluids* **30**, 143–152.

Tagawa, M., Kato, K. and Ohta, Y. 2003 Response compensation of thermistors: frequency response and identification of thermal time Constant. *Rev. Sci. Instrum.* **74** (3), 1350–1358.

Tagawa, M., Kato, K. and Ohta, Y. 2005 Response compensation of fine-wire temperature sensor. *Rev. Sci. Instrum.* **76** (9), 10 pages.

Tan, Z., Shikida, M., Hirota, M., Sato, K., Iwasaki, T. and Iriye, Y. 2007 Experimental and theoretical study of an on-wall in-tube flexible thermal sensor. . *Micromech. Microeng.* **17**, 679–686.

Tsuji, T., Nagano, Y. and Tagawa, M. 1992 Frequency response and instantaneous temperature profile of cold-wire sensor for fluid temperature fluctuation measurements. *Exp. Fluids* **13**, 171–178.